MEASURING, MODELING AND VERIFICATION OF LIGHT-MATTER INTERACTION PHENOMENA

Von der Carl-Friedrich-Gauß Fakultät
der Technischen Universität Carolo-Wilhelmina zu Braunschweig

zur Erlangung des Grades eines

Doktoringenieurs (Dr.-Ing.)

genehmigte

Dissertation

von Kai Berger

geboren in Braunschweig

am 16. März 1985

Eingereicht am: 2. Juli 2012

Disputation am: 12. Oktober 2012

1. Referent: Prof. Dr.-Ing. Marcus Magnor

2. Referent: Dr. Alexander Wilkie

(2012)

Acknowledgements

Many people supported and inspired me during the work on my thesis. I am grateful to my supervisor Prof. Marcus Magnor. You have shown me interesting new research directions and gave me the freedom to pursue my own ideas. I am also deeply grateful for the conferences and research groups I was able to visit during that time. Thanks to Anja Franzmeier and her team for always helping me with the administrative tasks, from booking tickets to organizing of conferences. I would especially like to thank all my colleagues from the Institut f. Computergraphik for working with me on previous publications and for oftentimes brighting the day. It has been great pleasure to work with these bright researchers. Thanks to Pablo Bauszat, Christian Lipski, Michael Stengel and Stefan John for proof-reading drafts of this dissertation. Special thanks is to Mark Albers, Marc Kastner, and Yannic Schröder, who worked as research assistants countless hours on recording and processing the footage for yet another deadline.

I am most grateful to my parents Udo and Hildegund and my brother Christian Berger. You have always supported me and started my interest in science.

Abstract

The photo-realistic rendering of scenes showing natural phenomena requires skilled graphic designers not only to produce a convincingly good-looking image but also to convey physical plausibility. This is especially important in industrial context, where a modelled scene showcasing a product has to approximate the actual environment of a product as closely as possible, e.g. in automotive industries. In this thesis, new techniques to measure natural phenomena are presented in order to provide new or verify existing models for rendering the physically plausible image. In contrast to other approaches, the measurement is performed using nonconventional methods: an ellipsometer is employed to capture the specular reflectance with respect to the polarisation behaviour, a transmissive screen attached to a glass tank is imaged to capture underwater reflectances, and the Microsoft Kinect, a motion capturing device, is used to detect the gas flows around objects. The results are the verification of existing, physically plausible models for commodity metals, an enhanced reflectance model for materials immersed in transparent media with known refractive index, and the reconstruction of two-phase gas flows around occluding objects.

Kurzfassung

Das Erzeugen von Szenen mit natürlichen Phänomenen in fotorealistischer Qualität ist aufwändig, weil nicht nur ein realistisches Bild erstellt werden soll, sondern auch physikalische Plausibilität in Bezug auf das modellierte Phänomen verlangt wird. Besonders in der Industrie, z.B. in der Automobilindustrie, sollte die modellierte Szene, in der ein Produkt eingesetzt wird, der tatsächlichen Einsatzumgebung so naturgetreu wie möglich ähneln. In dieser Dissertation werden neue Ansätze zum Messen von natürlichen Phänomenen präsentiert, die es ermöglichen, für bestimmte Phänomene neue Modelle zu erstellen oder bestehende Modelle erschöpfender zu verifizieren, um damit physikalische Plausibilität für Szenen, die am Computer ereugt werden, zu gewährleisten. Im Unterschied zu anderen Verfahren, werden unkonventionelle Methoden zur Messung umgesetzt: Mit Hilfe eines Ellipsometers wird die Oberflächenreflektanz von Metallen so vermessen, dass auch Änderungen im Polarisationszustand des Lichtes erfasst werden. Unterwasserreflektanzen von Materialien werden mit Hilfe eines lichtdurchlässigen Diffusers abgebildet, der an einen Glasbecher angebracht wird, und der Bewegungssensor Kinect von Microsoft wird verwendet, um Gasströmungen um Objekte zu detektieren. Die Ergebnisse sind die Verifikation von bestehenden Modellen für handelsübliche Metallflächen, ein erweitertes Reflektanzmodell für Oberflächen, die in refraktive Medien eingetaucht werden und die Rekonstruktion von Gasströmungen um Objekte.

Contents

List of Figures

List of Tables

List of Equations

LIST OF EQUATIONS

1

Introduction

1.1 Motivation

Real or fake - is this image a photo taken of the real world or is it generated by a computer? This question has become popular over the last decade and often led to interesting answers. As the advances in computer graphics over the past years have resulted in increasing photorealism, e.g. in cinema movies or in computer games, it has become increasingly difficult for a human observer to distinguish between a photo of the real world recorded with a digital single-lens reflex camera (dSLR) and a *rendering*. A notable example is also the synthetisation of faces to look similar to photos of human faces. While for some people the above question poses an artistic challenge, to dazzle viewers with the realism of their renderings, for others it represents a viable industrial task. An image, rendered to resemble a real-world situation as accurately as possible, can help by providing previews at a considerably lower cost compared to capturing the same situation in a controlled environment with a dSLR.

Consequently, graphic designers, artists and Computer-aided design (CAD) engineers have an interest in *models* to resemble real-world phenomena as accurately as possible with the constraint that the models should be as computationally inexpensive as possible. Usually, models are provided by research & development, either by conducting studies of the real-world situation to be resembled or by extending existing models and applying them to the context of the real-world situation. The former approach requires that a measurement setup be established; the latter requires a verification of the existing model, evaluating the extent of its applicability in the situation to be resembled.

1.1.1 Light-matter interaction phenomena in nature and today's life

Light-matter interaction shows up predominantly in the light reflectance of various surfaces when they are lit by a light source. While some exhibit a rough appearance to the observer, others look glossy and another surface may almost completely absorb light. Interestingly, a subpart of surfaces seems to exhibit a different reflectance behaviour when they are moistened. A range of effects in this context can be explained by assuming a surface of a certain thickness that exhibits porous behaviour, e.g. a watered stone, but other smooth surfaces, like plastic, can show similar behaviour. When they are permanently immersed, they reflect light differently - e.g. underwater, the highlight on a planar plastic surface seems to be visibly less intense and smaller in extent. In computer graphics, this effect should be taken into account when such a light-surface interaction is to be rendered accurately.

While the polarisation behaviour of light is averaged out in most renderings in the computer graphics discipline, its behaviour is still notable in life today, Fig. 1.1. Some arthropods, e.g. *Scarabaeidae*, have a skin texture that reradiates light in a left-circularly polarised manner (generated by the chitin structure of their cuticles [65]). Another example is the polarisation of skylight, that changes slightly with its position on the firmament relative to the sun. A third example is that of the *Sepia latimanus*, a Cephalopod, that has the ability to visually detect light polarisation. Note that its skin (their iridophores) can also affect the polarisation state of reflected light, e.g. to signal to other conspecifics [92]. In contrast, the human eye is not able to detect polarisation states, although through training, light faints in the skylight, known as Haidinger's brush [59], can be detected. The vision of the human observer can be enhanced by glasses with polarised filters, and thus the effects of polarised light, e.g. reduced mirroring at water surfaces or windows, can be made visible. In the context of computer graphics, this means that there are scenarios when a virtual scene, modeling the real-world exhibits polarisation behaviour that must be taken into account in the rendered image (e.g. a rendering of the retinal image of a *Sepia latimanus* detecting camouflaged prey). Thus, the modeled surface behaviour for real-world materials should not only account for the amount of reradiated light at a given wavelength but also for

Figure 1.1: Polarisation can be recognised in many aspects of today's life. Several animals exhibit polarisation-aware vision (left, *Sepia latimanus*, reproduced from [92]) or cuticle texture [65] (middle, *Cetonia aurata*, reproduced from [65]). Humans are usually insensitive to polarisation - but filter glasses can reveal its effects (right).

its polarisation state.

Two-phase flows, e.g. a propane gas flow in air, are an example of light-volume interaction phenomena, as they can be characterized as a participating medium. In the physical world of today, they can be seen as Schlieren with the bare eye around the wing of an airplane about to take off or through the exhaust stream of a jet, Fig. 1.2. Another example is the shadowgram of a gas plume above a candle [144] that can be noticed as a shadow above the flame when it is illuminated from a second light source, e.g. by sunlight. Its directional deviation scales with the second derivative of the plume's refractive index. The shape and velocimetry properties of gas flows are of interest to the aerodynamics and fluid engineering community, as they can reveal the resistance of an object immersed in the gas flows. In certain scenarios, it might be important to detect a gas flow, e.g. when searching for leaks in a pipeline system. The DARPA robotics challenge (DRC) has recently described such a scenario: an autonomous robot is given the task to move inside a building to find a broken gas pipe. The robot then has to stop the gas flow by turning the correct valve [33].

1.1.2 Scientific approaches in computer graphics

While in industry it is commonly assumed that computer graphics is a rather approximative field with the mission to convey good-looking, psychophysically plausible pictures, its underlying methods require the same scientific rigour found in related fields, such as applied physics or computer vision. The convincingly looking image of an aluminium teapot, anisotropically reflecting the light towards the camera, or the

Figure 1.2: Gas flows are prominent in several real-world examples, e.g. shockwaves (left), air streams (middle), or shadowgraphs of gas plumes above lit candles (right), reproduced from [46].

image of a woven silk cloth covering an object have in common is the fact that the accuracy of their renderings strongly relies on previously captured input data relating to their respective material substance. This process is known as measuring, Fig. 1.3, and is determined by a defined and controlled capturing environment, where the lighting conditions are known and adjustable. Consider the reflectance measurement of an arbitrary material: a patch under investigation is fixed in the centre of a lighting dome or a measurement gantry. A light source with known radiation characteristics is moved so that its position samples various incident angles with respect to the material patch. The same holds for the measurement device. In the last decade that device was mostly a Charge coupled device (CCD). Its array sensor's spectral response curves are known, and the camera is positioned so that several exitant angles are spanned. The recorded images, the samples of the measurement, are then registered according to the captured angles of incidence and exitance, and the data is stored accordingly. A renderer later has to evaluate the incident angles (i.e., the position of the light source with respect to the material patch) and the exitant angles (i.e., the position of the camera with respect to the material patch) for each projected spot on the object's boundary surface representing the captured material, and perform a lookup in the database of the corresponding measurement. The data is interpolated to account for density. The same holds for similar measurement tasks: image-based surface reconstruction or blackbody radiation measurement.

It has to be stated that the procedure described previously applies only to rendering tasks that do not include timing constraints or require data extrapolation. Real-time ray-tracing, an emerging research field in computer graphics assumes frame-rates of at least 30 frames per second (fps), thus inhibiting excessive online-searches, e.g. in

Figure 1.3: A nonexhaustive collection of measurement tools common to computer graphics and employed for this thesis, sorted from left to right by decreasing price. A CCD-camera (Canon EOS 5d), a light meter and the Microsoft Kinect (an RGBD-sensor).

material databases. To alleviate the computational load, a suitable model is fitted to the measured data. In material reflectance measurement, a function dependent at least on the incident and exitant angle is fitted to the data, allowing for fast computation and extrapolation. The same holds for the surface reconstruction of a human actor - a skinned skeleton is adjusted and partially deformed, e.g. to fit the imaged silhouettes of the captured actor. Both have in common to find a suitable model that fits the measured data as accurately as possible while computation time for that model is as small as possible.

Usually, the models described above can be considered as measurement-based heuristic models and, as such, do not necessarily incorporate any assumptions of underlying physical properties or processes. They are chosen, e.g. because they display the least error value to the measured data in comparison with other models. In contrast, models considered as physically plausible are deduced from underlying properties or processes. In an anthropologic scenario this can be described as follows: the hip joint is a synovial joint, and hence the bone attached to it can be modeled as a bone allowed to rotate around three axes (with constraints towards the eccentricity), but this model would not suffice to perform a diagnosis of *Osteoarthritis* [26], Fig. 1.4. In another scenario, e.g. surface reflectance modeling physically plausible models for metallic surfaces can be deduced from dipole models because of the wave characteristics of light and because of the way electromagnetic waves are reflected from dipoles. Still, a model that is deduced from the underlying physical properties has to be verified for the scenarios in which it is to be applied. This is usually done by reverting the above mentioned modeling procedure. A set of real-world samples is assembled and measured for the behaviour

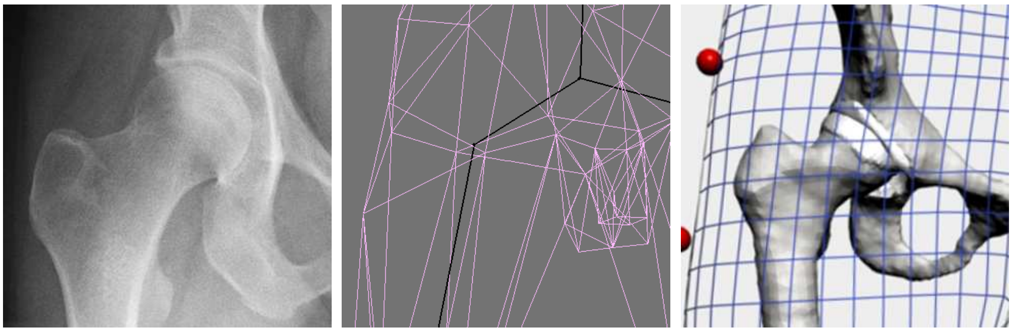

Figure 1.4: A model is used in computer graphics to simplify complexity in order to decrease computational burden or to allow extrapolation. A hip joint (left, CT image reproduced from [146]) can be simplified by a skeleton model (middle, black lines) with certain degrees of freedom (reproduced from[62]), but it would be too superficial for a diagnosis and has to be extended (right, reproduced from [26]).

predicted by the deduced model. If the measurements equal the predicted values within a margin of error, the model is successfully verified against the collected set and can be employed e.g. in physically plausible renderings of scenarios in which representants of the collected set are employed.

1.2 Physical background

This section introduces some concepts and properties of light and its interaction with matter. These properties are noticable in today's life, and are consequently a subject for modeling in computer graphics. Note that these concepts may not account for all properties of light, as, for, example quantum effects are neglected, but the necessary depth for applicability in rendering is pursued and maintained. At first, the concept of surface reflectance, a light-surface interaction process for objects, is formalised as a multidimensional Bidirectional Reflectance Distribution Function (BRDF). Then, the process of light path deviations noticed when light traverses heterogeneous media in terms of their optical density is rationalised using Fermat's principle of least path length, which as a concept is necessary in order to understand the noticeable effects of this process, so called *Schlieren*. Finally, the polarising behaviour of light is described by electromagnetic notation, i.e., the planar components of the wave are expressed in orthogonal and perpendicular equations. While this property may be less noticable in today's life, it still can be engineered to be visible in real-world scenarios. It further

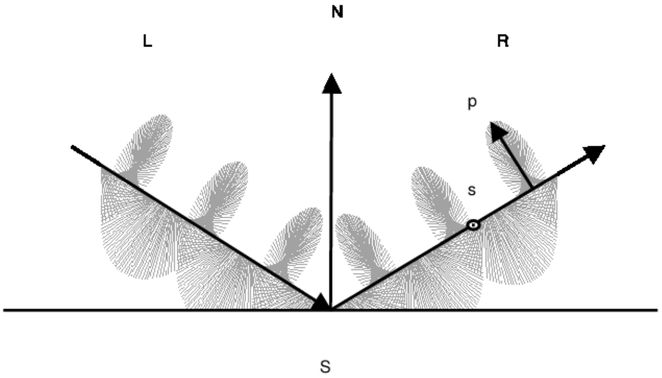

Figure 1.5: In surface reflection, light is usually modeled as a ray between the light source and the illuminated spot on the surface. The ray can be also seen as the propagation vector orthogonal to the light wavefront (gradients) being emitted from the light source. As light shows electromagnetic field behaviour as a transversal wave, it is associated with vectors describing the oscillation in the parallel (p-plane) and the orthogonal (s-plane, from German *senkrecht*) planes w.r.t. the surface normal $\vec{N}$ and . This example shows a clockwise circularly polarised light wave incident on a surface and being reradiated as an anti-clockwise polarised light wave. The positions of the electric field vector **R** coinciding with the s- or p-planes are denoted.

constrains models that are considered physically plausible to be valid in the context of polarisation awareness.

1.2.1 Bidirectional reflectance

The reradiation of light on the surface of an optically absorbing material can be described with Nicodemus [106] as the BRDF, which relates the amount of reflected light for a given exitant direction to a given incident direction. In the most general case, it can be written as a 10d function of two directions, i.e., four angles (θ_i,ϕ_i,θ_o,ϕ_o), two positions on the material surface and the wavelengths of the incident and exitant light beam λ_i and λ_o. Here, it is stated as a 4d function:

$$f_r(\theta_i, \phi_i, \theta_o, \phi_o) = \frac{dL_r(\theta_o, \phi_o)}{L_i(\theta_i, \phi_i) \cdot \cos(\theta_i) \cdot d\omega_i}, \tag{1.1}$$

$$\theta_i, \phi_i \in \Omega_i, \;\; \theta_o, \phi_o \in \Omega_o, \;\; \Omega_i = \Omega_o$$

with L_r being the reflected radiance and L_i being the incident radiance. The BRDF is traditionally integrated into the rendering equation (also referred to as the *illumination* or *scattering equation*) as follows:

$$L_o(\theta_o, \phi_o) = L_e(\theta_o, \phi_o) + \int_{\mathrm{d}\Omega} f_r(\theta_i, \phi_i, \theta_o, \phi_o) L_i(\theta_i, \phi_i) \cos(\theta_i) \mathrm{d}\omega, \tag{1.2}$$

where the term L_e models light-emitting or glowing surfaces.
At least two general BRDF constiuents can be distinguished [128].
The first type is the ideal diffuse BRDF:

$$f_{r_d} = \pi f_r \tag{1.3}$$

Its exitant radiance is independent from the angles θ_o, ϕ_o. The second type is the ideal specular reflector:

$$f_{r_s} = \pi f_{r_s}(\theta_i) \cdot 2\delta(\sin^2(\theta_o) - \sin^2(\theta_i)) \cdot \delta(\phi_o - \phi_i \pm \pi) \tag{1.4}$$

The exitant radiance is dependent on a Dirac-function of the distance between the incident and exitant angles θ, ϕ.
Phenomenologically, these two BRDFs seem to be opposites in terms of reflectance. In a statistical sense, this can be shown by considering both BRDFs as distributions on a 2D bounded domain and evaluating their Full Width at Half Maximum (FWHM), cf. the Appendix. The probability of a light ray being reradiated to a position $\vec{x}$ on the half-sphere is the same over the hemispherical domain for a diffuse BRDF. In contrast, it is infinity at $\vec{x}$ and zero elsewhere, if $\vec{x}$ lies on the mirroring vector. The FWHM is evaluated as $FWHM(f_{r_s}) \to 0$ for the mirror case, i.e., for a Dirac-distribution, while it is evaluated as $FWHM(f_{r_d}) \to \infty$ for the diffuse case, i.e., assuming constant probability over the domain. In recent work [107] the statistical interpretation of BRDFs has been employed to model and order them. There, reflectances showcasing one prominent lobe have been fitted with a Mises-Fisher distribution. This ordering maps the mirror to the infimum and the perfect diffuse reflection to the supremum.

If one were to assign real-world materials to both cases, one would identify dielectric Bragg mirrors (99.999% of light is reflected into mirroring direction) [3] with the mirror reflectance and the Spectralon with the diffuse reflectance ($> 99\%$ of light is reflected to any point on the hemisphere) [136].

Note that in the above considerations, the hemisphere Ω_o for the exitant radiance coincided with the hemisphere for the incident radiance Ω_i, which holds for all opaque media not obtaining subsurface scattering behaviour. If, instead, the transmittance behaviour of a screen with negligible width was to be considered, the hemisphere Ω_o for the exitant radiance would span the remainder of the unit sphere without the hemisphere for the incident radiance Ω_i. The distribution function would then read as the Bi-directional Transmittance Distribution Function (BTDF):

$$f_t(\theta_i, \phi_i, \theta_o, \phi_o) = \frac{\mathrm{d}L_r(\theta_o, \phi_o)}{L_i(\theta_i, \phi_i) \cdot \cos(\theta_i) \cdot \mathrm{d}\omega_i}, \tag{1.5}$$

$$\theta_i, \phi_i \in \Omega_i, \;\; \theta_o, \phi_o \in \Omega_o, \;\; \Omega_i \cap \Omega_o = \emptyset$$

1.2.2 Light path and the Eikonal equation

The propagation of light can be modeled as the wavefront propagation travelling through a continuous refractive index field. Here the ray coincides with the normal of the light's wavefront. Its propagation velocity is determined by the local density of the refractive index field. Its propagation can be generalised using Fermat's principle to travel the path of least time, i.e.,

$$\delta s = \delta \int_A^B n \, \mathrm{d}s = 0, \tag{1.6}$$

where s describes the path length (integrated over infinitesimal arc length elements $\mathrm{d}s$), which can be related to the travel time via the speed of light; A, B describe the position of the light source and the illuminated point; and n describes the continuous index field. Note that the equation is formulated in the calculus of variations notation.

If the light wave is considered to travel through 3D space with increasing z-value, then the path s can be rephrased as a function of z

$$s = (x(z), y(z), z(z)).$$

The infinitesimal arc length element is reformulated by chain rule

$$\mathrm{d}s = \sqrt{1 + \mathrm{d}x^2 + \mathrm{d}y^2}\mathrm{d}z$$

to arrive at

$$\delta s = \delta \int_{A_z}^{B_z} n(x, y, z)\sqrt{1 + \mathrm{d}x^2 + \mathrm{d}y^2}\mathrm{d}z = 0, \tag{1.7}$$

It can be interpreted as principle of stationary action where z is the time variable. It can be rewritten as a system of first order ordinary differential equations [72]:

$$n\frac{\mathrm{d}\vec{x}}{\mathrm{d}s} = \vec{d},$$

$$\frac{\mathrm{d}\vec{d}}{\mathrm{d}s} = \boldsymbol{\nabla} n,$$

where $\vec{r}$ describes the change in propagation direction at a point $\vec{x}$. The equations can be discretized e.g. by using the Euler scheme.

1.2.3 Field behaviour of light

Light can be described as an electromagnetic wave travelling through space with a field behaviour in the plane orthogonal to its propagation direction.

From Goldstein [53] pp. 530-531 one can find the mathematical description of a light wave being reflected from a (potentially layered) surface as a change in its field behaviour. A similar, but shortened description is given in the following Eqs. All introduced symbols that are used throughout the thesis are given in bold notation to help discriminate them from the same symbols in the graphics domain with a different meaning. At first, consider the incident wave as an electromagnetic wave with field components

$$\mathbf{E}_{||} = \mathbf{E}_{0||}e^{i\boldsymbol{\alpha}_{||}}, \mathbf{E}_{\perp} = \mathbf{E}_{0\perp}e^{i\boldsymbol{\alpha}_{\perp}}$$

where $\boldsymbol{\alpha}_\square$ denotes the phase and $\mathbf{E}_\square$ denotes the amplitude. In the following $_\|$ denotes the projection onto the parallel vector and $_\perp$ the projection on the perpendicular vector w.r.t. the plane of incidence, Fig. 1.5. In the literature, the symbols $_p$ and $_s$ (for german *senkrecht*) can be found as well. If a formula applies to both components, the symbol $_\square$ is employed as wildcard character. The same holds for the reflected wave

$$\mathbf{R}_\| = \mathbf{R}_{0\|} e^{i\boldsymbol{\beta}_\|}, \mathbf{R}_\perp = \mathbf{R}_{0\perp} e^{i\boldsymbol{\beta}_\perp}$$

with $\boldsymbol{\beta}_\square$ and $\mathbf{R}_\square$ denoting phase and amplitude again. Relating now the incident and the reflected light wave by the effect of reradiation from an optically absorbing material, it can be stated as

$$\mathbf{R}_\| = \boldsymbol{\rho}_\| \mathbf{E}_\|, \mathbf{R}_\perp = \boldsymbol{\rho}_\perp \mathbf{E}_\perp$$

which is reordered as

$$\boldsymbol{\rho}_\| = \frac{\mathbf{R}_\|}{\mathbf{E}_\|}, \boldsymbol{\rho}_\perp = \frac{\mathbf{R}_\perp}{\mathbf{E}_\perp},$$

where $\boldsymbol{\rho}$ is the change in wave propagation. Substituting the above with $\mathbf{E}_\|, \mathbf{E}_\perp, \mathbf{R}_\|, \mathbf{R}_\perp$ leads to

$$\boldsymbol{\rho}_\| = \frac{\mathbf{R}_{0\|}}{\mathbf{E}_{0\|}} e^{i(\boldsymbol{\beta}_\| - \boldsymbol{\alpha}_\|)}, \boldsymbol{\rho}_\perp = \frac{\mathbf{R}_{0\perp}}{\mathbf{E}_{0\perp}} e^{i(\boldsymbol{\beta}_\perp - \boldsymbol{\alpha}_\perp)}$$

Relating the $\|$ and $\perp$ component leads to

$$\boldsymbol{\rho} = \frac{\boldsymbol{\rho}_\|}{\boldsymbol{\rho}_\perp}$$

The change in amplitude can be extracted:

$$\tan(\boldsymbol{\Psi}) = \frac{\mathbf{R}_{0\|}/\mathbf{E}_{0\|}}{\mathbf{R}_{0\perp}/\mathbf{E}_{0\perp}}$$

Note that the *tangent* notation is used in order to be conformed with the traditional electromagnetic notation. The change in phase is extracted as

$$\boldsymbol{\Delta} = \boldsymbol{\beta} - \boldsymbol{\alpha} = (\boldsymbol{\beta}_\| - \boldsymbol{\beta}_\perp) - (\boldsymbol{\alpha}_\| - \boldsymbol{\alpha}_\perp)$$

In combination, the relative change in wave propagation can be expressed as

$$\boldsymbol{\rho} = \tan(\boldsymbol{\Psi})e^{i\boldsymbol{\Delta}} \tag{1.8}$$

Note that the relative change $\boldsymbol{\rho}$ is dependent on the wavelength λ of the incident light and the properties of the optically absorbing material, hence it can be written as a function with three variables

$$\boldsymbol{\rho} = f(n, \kappa, \lambda)$$

The relationship between the change in phase and amplitude and the reflectance ratio is called the *Fundamental Equation of Ellipsometry* [53], c.f. Eqn. 2.1, and will be examined in detail in Sect. 2.4.

1.2.4 Fresnel reflection in computer graphics

In computer graphics, the effects of the wave propagation of light can often be approximated. The averaged Fresnel reflection coefficient F_r is then used and stated as follows

$$\begin{aligned} F_r &= \frac{1}{2}\left(r_\perp^2 + r_\parallel^2\right) \\ \text{with} r_\perp &= \frac{(n_i\cos(\theta_i) - n_t\cos(\theta_t))}{(n_i\cos(\theta_i) + n_t\cos(\theta_t))} \\ r_\parallel &= \frac{(n_t\cos(\theta_i) - n_i\cos(\theta_t))}{(n_t\cos(\theta_i) + n_i\cos(\theta_t))}, \end{aligned}$$

where θ_i denotes the incident angle in the halfspace that contains the refractive index n_i and θ_o denotes the incident angle in the halfspace that contains the refractive index n_t. Both angles are measured as angle of inclination. Note that the Fresnel reflection coefficient is governed by the factors n_i, the refractive index of the surrounding medium, and n_t, the refractive index of the material. Due to energy conservation, the transmitted light is the light that is not being reflected off the surface, thus the Fresnel transmission coefficient is $F_t = 1 - F_r$.

1.2.5 Stokes vectors and Mueller calculus

Although the following calculus is not used for the derivation of any results in this thesis, it is still referenced in the following chapters. Therefore the calculus as provided by Goldstein [53] pp. 65-115 and its merits are briefly discussed. In order to represent the polarisation state of a light ray travelling through space, e.g. vertical polarisation or left-circular polarisation, the intensity vector, either 1d or 3D, is appended by three dimensions to arrive (in the 1d case) at the Stokes vector

$$\mathbf{S} = \begin{pmatrix} S_0 \\ S_1 \\ S_2 \\ S_3 \end{pmatrix}, \tag{1.9}$$

with $S_0 = \mathbf{E}_{0x}^2 + \mathbf{E}_{0y}^2$, $S_1 = \mathbf{E}_{0x}^2 - \mathbf{E}_{0y}^2$ being the intensity at the main axis of the elliptically polarised light and $S_2 = 2\mathbf{E}_{0x}\mathbf{E}_{0y}\cos\delta$, $S_3 = 2\mathbf{E}_{0x}\mathbf{E}_{0y}\sin\delta$ being the projected intensity at the axes of the field perpendicular to the propagation of the wave, where δ determines the phase shift between orthogonal transverse components.

The Stokes vector exhaustively describes the polarisation state of a light wave. The wave can interact with elements changing its behaviour in terms of polarisation, e.g. a vertically polarised light will be reduced to zero intensity when passing through a horizontal polariser. The interaction process is represented by 4 × 4 Mueller Matrices.

$$\begin{pmatrix} S'_0 \\ S'_1 \\ S'_2 \\ S'_3 \end{pmatrix} = \begin{pmatrix} m_{00} & m_{01} & m_{02} & m_{03} \\ m_{10} & m_{11} & m_{12} & m_{13} \\ m_{20} & m_{21} & m_{22} & m_{23} \\ m_{30} & m_{31} & m_{32} & m_{33} \end{pmatrix} \begin{pmatrix} S_0 \\ S_1 \\ S_2 \\ S_3 \end{pmatrix}, \tag{1.10}$$

In this thesis, two optical components that attenuate or phase-shift the light are used as a *black box* for the creation of elliptically polarised light and thus for the measurement of polarisation states. They are presented in the following in Mueller matrix notation as an example of the calculus.

The ideal linear polariser rotated by angle θ can be written as

$$\mathbf{M} = \frac{1}{2}\begin{pmatrix} 1 & \cos(2\theta) & \sin(2\theta) & 0 \\ \cos(2\theta) & \cos^2(2\theta) & \cos(2\theta)\sin(2\theta) & 0 \\ \sin(2\theta) & \sin(2\theta)\cos(2\theta) & \sin^2(2\theta) & 0 \\ 0 & 0 & 0 & 0 \end{pmatrix} \tag{1.11}$$

and the nonrotated retarder of retardance $\boldsymbol{\Psi}$ is given as

$$\mathbf{M} = \begin{pmatrix} 1 & 0 & 0 & 0 \\ 0 & 1 & 0 & 0 \\ 0 & 0 & \cos(\Psi) & \sin(\Psi) \\ 0 & 0 & -\sin(\Psi) & \cos(\Psi) \end{pmatrix} \tag{1.12}$$

In combination, the rotated polariser and the retarder are able to create elliptically polarised light from an incident light beam. Interestingly, the polarisation state of the incident light beam is considered as arbitrarily polarised and not as unpolarised, i.e., all components of the Stokes vector have non-zero values. This might seem counterintuitive, but it fits the behaviour of natural light which is not unpolarised, but arbitrarily polarised in general [53].

1.3 The predictive rendering pipeline

Generating a rendering in computer graphics with respect to the above mentioned physical properties is known to the computer graphics community as *predictive rendering*. The name originates from the fact that light transport in a scene is simulated outright, which enables the viewer to accurately predict what a rendered scene would look like under the conditions specified in the employed model. It has to be pointed out that, although such a rendered image might look artistically appealing or sometimes convey a certain aesthetic, the intention of the predictive rendering is not artistically motivated. Instead, its main usage area is in virtual prototyping for appearance-sensitive industries with high prototyping costs, such as the automotive sector, or architecture. In these industries, cost reduction in the modeling process is a crucial economic factor. The concept of predictive rendering is discussed in detail by Wilkie *et al.* [147] and summarised here briefly:

The generation of rendered images can be considered as a linear pipeline, with three main components: the first part of the pipeline is modeling, i.e., the replication of the exact geometry of scene elements or their material properties. The second part is rendering, e.g. the spectral sampling of light transport in a modeled scene through a virtual camera stored in a 2D image file. The final part is display, i.e., the presentation of the information stored in the 2D image file in a psychophysically plausible way, e.g. by incorporating perceptional models of early stages of the human visual system.

It is important to note that the entire pipeline is a chain that is as strong as its weakest link: each part of the pipeline is a crucial factor for the accuracy of the following parts of the pipeline.

1.4 State of the art

Currently, in computer graphics a multitude of reflectance models is considered physically plausible because they are derived from theoretical models, e.g. models based on oscillating dipoles that reradiate light, but the real-world applicability of these models has not been verified through measurements that are not prone to errors commonly known to computational photography (i.e., the spatial resolution of the CCD-chip, Bayer-pattern filters, intensity changes due to sensor noise). There exist models that incorporate the polarisation reflectance behaviour [51] of surfaces, but they are usually derived by adding linear polarisation filters to an existing setup, CCD-chip and white light source, thus incorporating the same problems. Their goal is to state a Mueller-Matrix [71, 117] of the sample under investigation and to consider the light as an according vector that stores polarisation states. Other approaches employ ellipsometry for the virtual restoration of a Mesopotamian statuette (manufactured around 200 B.C.) and for rendering purposes [19, 20, 21, 24, 111].

Furthermore, considerable effort has been invested into describing different properties of reflected light through BRDFs by introducing several variables (e.g. the Bidirectional subsurface scattering reflectance distribution function (BSSRDF), phosphorescence, spacial variance of reflectance), but the dependence of the properties of a reflected light cone on the surrounding medium has not been yet investigated with respect to physical plausibility. Much work has been done on investigating moistening effects on surfaces, i.e., wetting [31] and drying processes [150] especially the styling processes of hair [58, 74, 140], or the wetting processes of porous materials [150]. Also the attenuation of light by the participating media has been investigated [109]. A variety BRDF models for describing the reflectance behaviour of surfaces in general (either in air or in a refractive medium) has been presented in the last decades. Phenomenological models are based on an intuitive modeling of the reflection process such as the famous Phong model [113]. Purely ad-hoc methods such as the original Phong model, but also physically plausible BRDF models fall into the category of phenomenological models, where the latter characterisation refers to the fact that ad-hoc models can be built such that they do not obviously violate the principles of positivity, reciprocity, and energy conservation. Examples include the generalised Phong model of Lafortune *et al.* [82], approximations of physical models as in Schlick [124], the reflection model for metallic surfaces by Kelemen and Szirmay-Kalos [80], or the approximation of subsurface scattering processes by Jensen *et al.* [73]. Physics based models, in contrast, originated in the optics literature: the seminal work of Torrance and Sparrow [132] was introduced to computer graphics by Blinn [16]. Cook and Torrance [28] extended the micro-facet model to use Beckmann's [9] micro-facet distribution function. Kajiya [76] developed a micro-faced model for anisotropic rough surfaces, based on an integral description using wave optics. He tabulated the BRDF values for efficient computation. A physics-based analytical model for anisotropic reflection was introduced by Poulin and Fournier [115]. A model based on physical optics, i.e., on electro-magnetic theory, was developed by He et al. [64].

In addition, a regular micro-surface geometry like v-grooves is assumed to compute the geometry term. Oren and Nayar [108] instead consider microgeometry consisting of perfect Lambertian reflectors while retaining the regular micro-geometry assumption. They show that a rough surface consisting of such facets has appreciable non-lambertian reflectance. Ashikmin *et al.* [4] remove the regular micro-surface geometry assumption, developing a method to compute a suitable micro-surface geometry for a given, even designed, BRDF. Physics-based models inherently ensure BRDF energy conservation, reciprocity, and positivity properties of the resulting function.

Measurement-based models take a different approach than phenomenological models. Instead of creating models from analytical descriptions of physical processes, they are based on measurements of the reflection properties of real-world materials. Suitable functions that describe the observed behaviour are then fitted while preserving the basic BRDF properties as in the phenomenological models. An example of this approach is the anisotropic Ward model [140]. He et al. [64] also show fits of their physics-based model to real-world data. The Lafortune model [82] was specifically developed to fit observed data well. A different approach is taken by Matusik *et al.* [95]. The authors acquire a large data base of reflectance data for a wide range of materials. Then they analyse the data using Principal Component Analysis (PCA) and nonlinear dimensionality reduction techniques to derive a low-parametric model given the initial data. Kautz *et al.* [78] present a method that uses spherical harmonics for representation of the captured data.

BRDF acquisition has been performed using a variety of devices. The most commonly used tool in optics is the gonioreflectometer. With this device, a planar sample is analysed by a hemispherical adjustable detector and light source. Marschner *et al.* [91] developed an image-based BRDF measurement technique based on spherical samples. This way, moving the detector can be avoided and BRDFs with a high resolution in the viewing direction can be acquired. Therefore, the approach is the prevailing technique for BRDF acquisition in graphics. Matusik *et al.* [95] use a similar setup but propose to reduce the number of measurements by using their data base. An evaluation of analytical BRDF models for data fitting purposes has been performed by Ngan *et al.* [105]. Ghosh *et al.* [52] expand the BRDF measurements in an optical basis and directly

measure the basis coefficients, removing the need for any mechanical parts. Recently, Hullin *et al.* [70] have extended the concept of a monochromatic BRDF to account for bi-spectral interaction, i.e., conversion of the wavelength of light by the material, e.g. in fluorescent materials. They do not develop a model based on their measured data. Methods for acquiring a spatially-varying BRDF (svBRDF) have also been developed but are of less interest in the context of the proposed approach.
The bidirectional BTDF models describe the transmission of light at the boundary of materials. While Dai *et al.* [30] and Walter *et al.* [138] present BTDF models for the entire entrance and exit process of light, the following papers present BTDFs for subsurface effects of opaque materials. Weidlich *et al.* [142] describe a multi-layer model for the rendering of metallic paints or frosted metal. Hanrahan *et al.* [61] describe a layered surface model for subsurface reflectance that takes the Fresnel effect into account.

While there exist elaborate algorithms to detect unobstructed, potentially transparent flows relying on inexpensive capturing setups [6], and simple algorithms to detect turbulent flows around occluders relying on elaborated setups [38], there is no algorithm that is able to detect the turbulent gas flow around occluders relying only on consumer-grade capturing setups. On the contrary, recently the RGB and depth map (RGB-D) sensors have been the focus of the computer science community [103], but it can be noted that their main applications lie in pose reconstruction, real-time mesh registration and facial recognition; or, in other words, in the applicational context of opaque surface capturing.

1.5 Contribution of the thesis

The goal of this thesis is to provide new ways to measure, model and verify the effects that occur when light interacts with (opaque and transparent) matter. The ellipsometer, an established measurement device, is transferred from applied physics to computer graphics and used for verifying existing reflectance models by measuring the polarisation behaviour of real-world surfaces and circumventing problems afflicting state-of-the-art reflectance measurement setups based on CCD-cameras. Then, a new reflectance model is introduced that explains the effects introduced to surface reflectance by surrounding media. A theoretical and practically tailored measurement setup for capturing these effects is introduced and described in detail. Finally, an affordable RGB-D sensor is, for the first time, used for a two-phase gas flow measurement based on light path deviation.

Part of this work has been published at the *16th International Workshop on Vision, Modeling, Visualization 2011* [13, 15], the journal *Computer Graphics and Applications, special issue on Modeling and Rendering Material Appearance* [16] and the workshop *CDC4CV* in conjunction with *ICCV 2011* [14] and represents the foundation of this thesis. Beyond that, an in-depth analysis of the measurement setups, a derivation of the employed models and fitting algorithms and a broad discussion of the results are laid out herein. The comparison to the related work is expanded to account for recent achievements in the field since the time of publication.

1.5.1 Structure of this thesis

This thesis is structured to account for different aspects of light-matter interaction phenomena: light-surface interaction, i.e., the verification of the polarisation behaviour of real-world surfaces, the modeling of surface reflectance in immersed materials, and light-volume interaction, i.e., the measurement of gas flows by employing light path alteration effects visible in commodity RGB-D sensors. Each aspect is structured as follows: embedding into the related work in the particular field, a definition of the setup for examination, the collection of samples, i.e., objects, patches, gases, and a classification of the implementation of the computational algorithms. For each aspect a distinction is drawn between methodological and observational results, i.e., the liabilities of the particular methods are discussed independently from the examination of the samples. Note that each related work also includes recent and closely related work where one or two publications are examined in greater detail. This part addresses concurrent approaches that were published during or after the experiments undertaken for this thesis in order to account for currency.

In Chapter 2, measurements of the polarisation behaviour of real-world surfaces are conducted and compared to the predictions of existing reflectance models in order to verify them. The set of materials is stated and the measurement device is introduced.

Afterwards, the fitting procedure is described, Sect. 2.5, and the models under investigation are listed. The results are split into general aspects of reflectivity, such as anisotropy, Subsect. 2.6.1, and the textural position on the surface, Subsect. 2.6.3, and into notable material reflectance results, such as anodised aluminium, Subsect. 2.6.4.

In Chapter 3, the new measurement setup for immersed materials is presented and evaluated in order to get a suitable BRDF to incorporate the effects of surrounding media. The set of materials, Sect. 3.5, is stated and the measurement device, Sect. 3.4, is introduced. An insight into the collection of the employed refractive media is presented in Sect. 3.6. The preprocessing of the captured image data is described in Sect. 3.7, while the proposed model is introduced in Sect. 3.8. Again, noteworthy results are discussed. The chapter concludes with fitting and rendering results, Subsect. 3.10.5.

Finally, RGB-D sensors are employed to capture and reconstruct obstructed gas flows in Chapter 4. At first, the image formation under the presence of refractive media is discussed, Sect. 4.3. Then, the measurement setup is introduced, Sect. 4.4 and calibration tasks for heterogeneous sensor setups, such as multiple RGB-D-sensors, are discussed, Subsect. 4.4.1. The results are, again, split into general aspects of the evaluation approaches, Subsect. 4.8.3 and Subsect. 4.8.4, and some notable obstructed gas flows after the introduction and use of occluders, Subsect. 4.8.5.

The conclusion of the thesis is presented in Chapter 5. An outlook towards further research in the evaluated field of light-matter interaction phenomena is also presented in this chapter.

2

Light-surface interaction: Validation of physically plausible reflectance models

2.1 Introduction

In state-of-the-art reflectance measurement methods in computer graphics, the underlying setup mostly consists of CCD-cameras. Marschner *et al.* [91] introduced such a framework, where light is shone onto a spherical surface and the reflected cone is imaged with a Photometrics PXL 1300L CCD camera. This approach has been widely adopted, e.g. for the establishment of the Mitsubishi Engineering and Research Lab

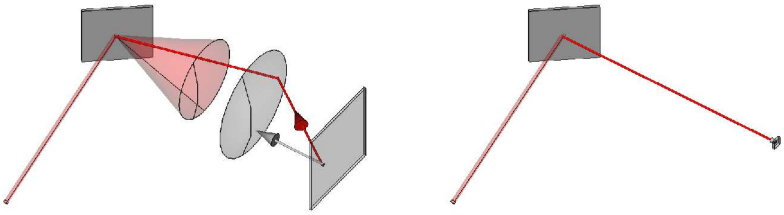

Figure 2.1: In traditional reflectance capture, a spherical cap has to be imaged onto the planar CCD chip, where only a fraction of the pixels is used for BRDF computation. The proposed method constrains the measurements to the mirroring direction. A physical aperture constrains the opening angle to be minimal. This setup is realised using an ellipsometer.

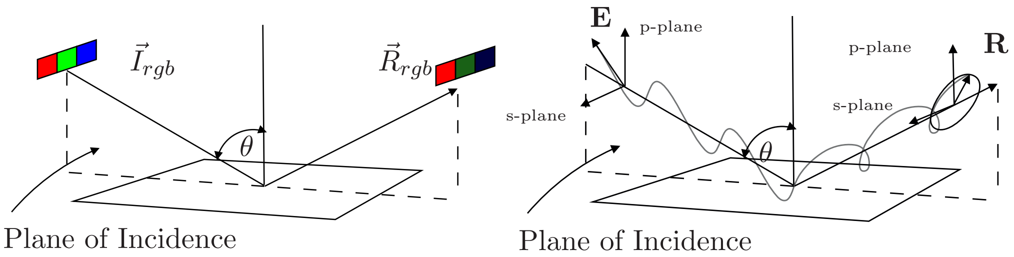

Figure 2.2: In computer graphics, reflected light is usually considered as a scalar or as an RGB-triplet (top). The proposed approach considers the spectrum of light waves $\mathbf{R}_\lambda$, that are attenuated and shifted in phase. The wavelength-dependent ratio of parallel and perpendicular reflectance values of a surface is measured with an ellipsometer. The combination of both reflectance values defines the perceived intensity of the reflected light (bottom).

(MERL) BRDF database [95, 96] (they used a QImaging Retiga 1300 CCD camera), but these setups have the drawback that CCD-cameras are prone to sensor noise. Finally, there is a problem in that a solid angle, which is a curvilinear quadrilateral, has to be mapped to a planar 2D surface, Fig. 2.1. Thus, the image sensor has to be chilled to $-25°C$ [27] and a majority of the pixels in the image are ignored while the rest is are used for computation (cf. to [91]). Furthermore, these methods only provide ground truth for the intensity differences of the reflected light, but they fail to provide data for the change in polarisation behaviour, Fig. 2.2. When certain light-matter interaction phenomena are to be modeled, as explained in Sect. 1.1, that deficiency can affect the plausibility of the rendered image.

2.2 Related work

Phong [113] was the first to introduce an intuitive model for the light reflection process of surfaces. He constrained the model only to the principles of reciprocity and positivity, i.e., the model is not necessarily energy-conservant. Ward *et al.* [139] performed measurements of the reflection process and then fitted a suitable function to the numerical measurement results. A large database that consists only of the goniometric reflectance values for a huge variety of materials has been captured by Matusik *et al.* [94], but it does not provide a model to explain the values. In physically-based rendering, plausible BRDF models are used for rendering. These models assume an accurate representation of idealized surface patches. The most prominent model was

	Manufactured setup	Commodity hardware	Mueller Matrix	Metallic Surfaces	Model Validation
Evaluated Setup	-	-	-	✓	✓
Callet *et al.* [22]	-	✓	-	✓	-
Ghosh *et al.* [51]	✓	-	✓	✓	-

Table 2.1: Comparison of related work to this approach: while Callet *et al.* [22] use ellipsometry to create a realistically looking facsimile of a bronze alloy artefact, Ghosh *et al.* [51] use photos taken with polarisation filters attached to the camera to establish Mueller Matrices for the reflectances of surfaces. This approach relies on ellipsometry to validate physically plausible BRDFs.

introduced by Torrance and Sparrow [132] back in 1967 in the physics community. This model has been adapted by many researchers, e.g. Blinn [16] and Cook [28], to enable them to use different microfacet models.

These models have only been experimentally verified excluding their polarisation behaviour. Recent work in polarisation-aware surface reflectometry has been published, but it rather presents measured data instead of validating existing models [51]. In this evaluation, the focus is on the Torrance and Sparrow BRDF-model as a representative of physically plausible models, and different microfacet models are examined. Also, the real-world measurements are compared to the Fresnel equations.

In this section, physically plausible models are verified with the equations of Ellipsometry [53]. The necessary equations were derived by Paul Drude in 1887. Around 1901, an early instrument was imaged by Drude, but the first working ellipsometric measurement instrument is believed to have been completed by Jules-Celestin Jamin around 1847. Back then, it consisted of two telescopes with attached linear polarizers. The image was directly evaluated with the eye in the same way as with a microscope. The name ellipsometer was first introduced in February 1945 by Alexandre Rother in Review of Scientific Instruments [121]. Until the 1940s, ellipsometry did not take wavelength-dependency into account. The technique was to rotate the analyser until an intensity minimum, ideally zero intensity, was reached (Null ellipsometry). A measurement of a surface patch took about an hour. Therefore, the photometric ellipsometer configuration emerged. The polariser, cf. Eqn. 1.11, is fixed at 45° and a retarder, cf. Eqn. 1.12, is optionally placed inside the beam. The reflected light is always elliptically polarised, so that the analyser simply has to rotate continuously and the intensity of

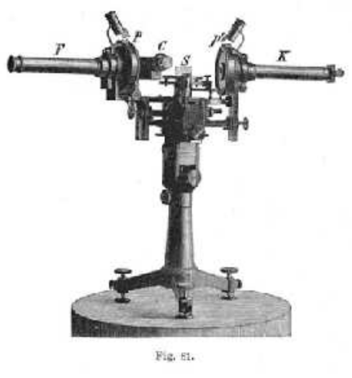

Figure 2.3: The first ellipsometer was imaged by Paul Drude in 1887 and it consisted of two telescopes (**F**,**K**), both attached to linear polarizers ($\mathbf{p}$,$\mathbf{p}'$), c.f. Eqn. 1.11. **C** represents a Babinet-Soleil compensator, a retarder, cf. Eqn. 1.12. A sample **S** was placed in the middle. The image was directly evaluated with the eye, reproduced from [41].

the resulting beam is a sinusoid over time. Using Fourier analysis $\boldsymbol{\Psi}$ and $\boldsymbol{\Delta}$ can be retrieved, c.f. [53] pp. 532–538. The ellipsometer is based on the spectroscopic ellipsometer configuration which was first developed in 1975 by Aspnes *et al.* [122]. The emitted light is produced by a white light source and the retrieved light passes through a monochromator. Other approaches in the area of digitising cultural heritage succeeded in employing spectroscopic ellipsometry as well [22, 23]. In contrast to this work, they restricted themselves to reconstructing artefacts made of alloys, such as bronze, and copper. Part of this chapter has been published in the journal *Computer Graphics and Applications, special issue on Modeling and Rendering Material Appearance* [16].

Recently, Callet *et al.* [22] proposed to use ellipsometry within the context of cultural heritage. Their task was to create a virtual model of an archaic artefact from the Idalion area, near today's city of Dhali. The artefact, a tablet from around the time 480-470 B.C., was manufactured in bronze and remained in the *Bibliothèque Nationale de France*. As a donation to the Mayor of Dhali, the virtual model should be realised as a physical copy of a bronze plate and resemble the original artefact as closely as possible. At first, the macrostructure of the artefact's surface was scanned with a coded light approach. Its accuracy was in the range of 50μm. In order to model the polarisation behaviour of the bronze alloy and, thus, create a physical copy without

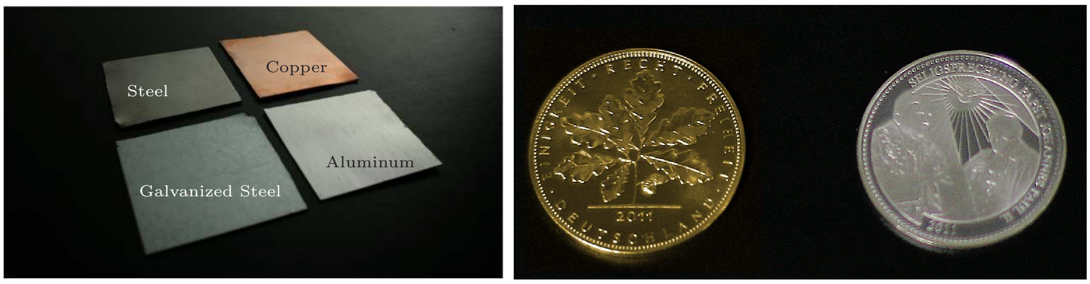

Figure 2.4: The examined materials comprise a subset of commodity metals: steel, copper, galvanized steel, aluminium (left image), gold, and silver (right image).

unnecessary oxidation patina, the authors employed ellipsometry, in this case a Woollam ellipsometer from the Institut des NanoSciences de Paris (ISNP). The benefit of this approach was to interact non-destructively with the artefact by employing light-based methods. The 3D shape of the facsimile was printed in wax with a 3D printer and a negative was formed by dipping the facsimile into melted silica with grains. Finally, the alloy to form the facsimile is melted and poured into the dried negative.

On the contrary, their approach is used only to characterize the influence of elements in the alloy. For example, lead was found to have less than 1% of influence on the overall perceived appearance. Their main task was to fit a surface model to the measurement of an artefact. Besides, they drew an estimate on the thickness of the corrosion layer. It differs from the evaluated approach in this thesis in that it does not aim to verify a certain BRDF model considered as physically plausible to a broad set of materials, but to visually fit one object in its geometric and visual appearance as closely as possible to the properties of the original artefact.

2.3 Measurement

In the following section, the measurement process with the ellipsometer is described, the preparation of the materials is discussed, and potential alterations to the measurements introduced by anisotropy or by spatially varying the position of the sample are evaluated.

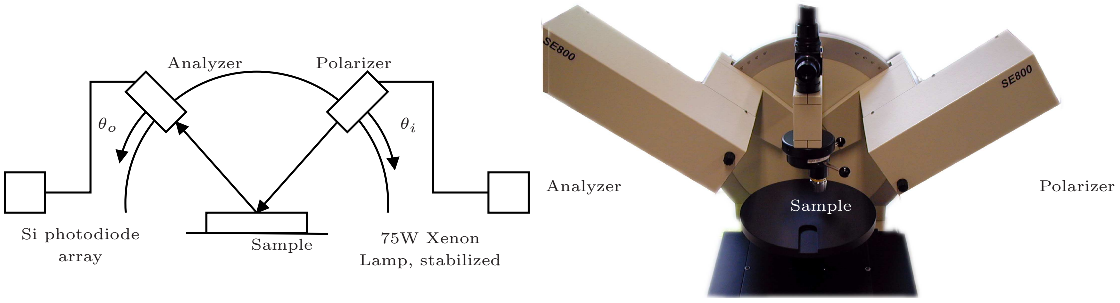

Figure 2.5: Left: Schematic depiction of the ellipsometer setup. Right: SE-800 ellipsometer from SENTECH. For the optical elements polariser and retarder refer to Eqn. 1.11 and 1.12 respectively.

2.3.1 Materials

The focus is set on metals that are obtainable in daily life, Fig. 2.4. From a local hardware store thin plates of copper, galvanized steel and anodised aluminium were gathered. The aluminium is passivated with an oxide layer of defined thickness in order to prevent corrosion. For comparison, annealed aluminium foil has been collected as well. Additionally, the *Münzhandelsgesellschaft deutsche Münze* provided a silver and a gold coin with a defined purity of 99.9% - both manufactured with the *Polierte Platte*, i.e., mint state, procedure [39]. Note that the coins have not had a surface polish applied for economical reasons: the value of the coin would significantly decrease with the small scrapes introduced by the polish.

2.3.1.1 Preparation

The collected materials have not been treated with polish or cleaning fluid. Thus, the samples do not obtain an additional, possibly unintended thin film and can be considered as substrate.

2.3.1.2 Anisotropy and spatial variation

All materials were measured with different rotations around the surface normal to account for anisotropy and with varying positions on the patch surface to account for alterations introduced by spatial variation.

2.3.2 Setup

In contrast to reflectance measurements common to computer graphics, the material patches, usually 5×5cm^2, were not imaged with a dSLR. Instead, they were placed in the centre of an ellipsometer, Fig. 2.5, that measures the polarisation states of the reflected light in the mirroring direction for incident light. In this case, the measurement device was a SENTECH SE800 ellipsometer, a spectroscopic ellipsometer that provides 1024 equidistant samples in the range from 246.84nm to 866.25nm. The intensity profile of the incident light is similar to a white light source, because it is generated with a Xenon (XE)-lamp, Fig. 2.6. This ensures support in the complete Visible range $(390 - 750\text{nm})$ (VIS). The light is collimated to produce an image on the sample of 5 mm diameter and a 1 mrad divergence. Stable results can usually be obtained after about 10 minutes to warm up the XE-lamp [127].

2.3.3 Angular sampling

The SENTECH SE800 Ellipsometer provides angular sampling within the range from 45° to 80° with a step size of 10° with additional sampling positions at 45° and 75°. It is known that on smooth metallic surfaces, the difference in polarisation is amplified between 60° and 85° of the grazing angle of incidence, i.e., Brewster's angle. For dielectric surfaces the angle with the largest differences in polarisation is between 55° and 60°. Hence, in the conducted measurements, the following angles of incidence have been measured: 45°, 50°, 60°, 70°, 75° and 80°, which provides a dense sampling in the angular range with the highest difference in polarisation. Due to the technical constraints of an ellipsometer, the incident and exitant viewing angle are always identical. Off-reflectance angles are not measurable.

2.4 Reflectance ratio computation

At first, the polarisation states of the reflected light are measured with an ellipsometer. Then, the ratio of parallel surface reflectance $r_{\parallel}$ and perpendicular surface reflectance $r_{\perp}$ values are computed and compared to literature values [110].

The conversion from polarisation states to the reflectance ratio is performed by using the *Fundamental Equation of Ellipsometry* for this conversion, cf. Eqn. 1.8. The equation states that

$$\boldsymbol{\rho} = \tan(\boldsymbol{\Psi})e^{i\boldsymbol{\Delta}} = \frac{r_{\parallel}}{r_{\perp}} \tag{2.1}$$

with $\boldsymbol{\rho}, r_{\parallel}, r_{\perp} \in \mathbb{C}$. A thorough derivation of the equation can be found in [53] pp. 529 - 531. The variables $\boldsymbol{\Psi}$ and $\boldsymbol{\Delta}$ represent the amplitude attenuation and phase shift induced on the reflected light wave, Sect. 1.2.3, $\boldsymbol{\rho}$ denotes the ratio of $r_{\parallel}$ and $r_{\perp}$. The ellipsometer is constrained to measure $\boldsymbol{\Psi}$ and $\boldsymbol{\Delta}$ for a given angle of inclination and a given wavelength, Sect. 2.3.2. Then, $\boldsymbol{\rho}_{\text{data}}$ is computed from the $\boldsymbol{\Psi}$ and $\boldsymbol{\Delta}$ values that are measured with an ellipsometer for varying wavelength λ and angle of inclination θ using Eqn. 2.1. Then the model reflectance ratio is derived $r_{\parallel_{\text{model}}}$ and $r_{\perp_{\text{model}}}$ for a physically based BRDF model and the ratio $\boldsymbol{\rho}_{\text{model}} = \frac{r_{\parallel_{\text{model}}}}{r_{\perp_{\text{model}}}}$ is computed. Finally, a fitting of $\boldsymbol{\rho}_{\text{model}}$ to $\boldsymbol{\rho}_{\text{data}}$ is performed, Sect. 2.5.

2.5 Model fitting

The employed reflectance model is introduced and the set of microfacet distribution functions is evaluated. As a fitting procedure, the Levenberg-Marquardt procedure is mathematically derived and employed in the context of the measured data.

2.5.1 Models

The Fresnel terms are to be fitted for their parameters n (refractive index) and k (extinction coefficient) and the Torrance-Sparrow BRDF [131],

$$r_{\square} = \frac{1}{4\cos(\theta_o)\cos(\theta_i)} * Fr_{\square} * G(\theta_o, \theta_i) * D_n,$$

with the following distribution terms D and their roughness parameter β:

- Blinn-Phong [16]
  $D = \cos\angle(\vec{h}, \vec{n})^{\frac{-\log(2)}{\log(\cos(\beta))}}$
  with β as exponential parameter.
  It resembles a simple Phong model, but it is interpolated to reduce the computational burden.

- Gaussian [131]
  $D = \exp(-(\frac{\sqrt{\log(2)}}{\beta}\cos(\angle(\vec{h},\vec{n}))^2))$,
  i.e., the facets are Gaussian distributed.
  It specifies the amount of facets oriented at an angle $\frac{\angle(\vec{h},\vec{n})}{\beta}$ from the average surface normal.

- Beckmann [9]
  $D = \frac{1}{\beta^2 \cos(\angle(\vec{h},\vec{n}))^4}\exp(-(\tan(\angle(\vec{h},\vec{n}))/\beta)^2))$, where β is the Root Mean Square (RMS) slope of the surface microfacets. The surface's roughness scales with the absolute amount of reflectance without futher constants, but the computational load is comparatively high.

- Trowbridge and Reitz [134], where microfacets are modeled as ellipsoids with eccentricity c:
  $D = (\frac{c^2}{\angle(\vec{h},\vec{n})^2 \cdot (c^2-1)+1})^2$,
  $c = \sqrt{\frac{\cos(\beta)^2-1}{\cos(\beta)^2-\sqrt{2}}}$ describes the ratio of the lengths of the two main axes.

Note that $\vec{n}$ and $\vec{h}$ refer to the surface normal and microfacet normal, i.e., the halfway-vector between the incident $\vec{l}$ and exitant $\vec{v}$ ray.

2.5.2 Levenberg-Marquardt fitting

Model fitting is performed using the Levenberg-Marquardt [90] algorithm with the problem formulated as

$$E(\beta) = \sum_{i=1}^{m}(y_i - f(x_i,\beta))^2,$$

where E denotes the sum of squares of deviations between the measured values y_i and the predicted values at positions x_i (here, wavelength and incident angle) for a function f (the BRDF model with parameters β, here the surface roughness). The solution is found iteratively

$$f(x_i,\beta+\delta) \approx f(x_i,\beta) + J_i\delta,$$

with J_i being the Jacobian of f with respect to the parameters β:

$$J_i = \begin{pmatrix} \frac{\partial \Re \boldsymbol{\rho}}{\partial n_1} & \frac{\partial \Re \boldsymbol{\rho}}{\partial k_1} \\ \frac{\partial \Im \boldsymbol{\rho}}{\partial n_1} & \frac{\partial \Im \boldsymbol{\rho}}{\partial k_1} \\ \frac{\partial \Re \boldsymbol{\rho}}{\partial n_2} & \frac{\partial \Re \boldsymbol{\rho}}{\partial k_2} \\ \frac{\partial \Im \boldsymbol{\rho}}{\partial n_2} & \frac{\partial \Im \boldsymbol{\rho}}{\partial k_2} \\ \vdots & \vdots \\ \frac{\partial \Re \boldsymbol{\rho}}{\partial n_s} & \frac{\partial \Re \boldsymbol{\rho}}{\partial k_s} \\ \frac{\partial \Im \boldsymbol{\rho}}{\partial n_s} & \frac{\partial \Im \boldsymbol{\rho}}{\partial k_s} \end{pmatrix}, \quad \begin{array}{l} \left.\begin{array}{l} \\ \\ \end{array}\right\} \text{Top film layer} \\ \left.\begin{array}{l} \\ \\ \end{array}\right\} \text{Second film layer} \\ \\ \left.\begin{array}{l} \\ \\ \end{array}\right\} \text{Substrate layer} \end{array}$$

for a generic BRDF incorporating multiple film layers n_1, k_1, n_2, k_2... and the substrate n_s, k_s, where n denotes the index of refraction and k denotes the extinction coefficient. Here, $\Re$ and $\Im$ denote real and imaginary parts of the reflectance ratio, respectively. In the examined measurements, only one film with the known refractive index of air ($n = 1.0$, $k = 0.0$) is assumed, while the substrate is fitted. A local minimum is theoretically found when $J_i = 0$, but numerically a minimum can be considered for an error of $E(\beta) < 10^{-16}$. Care has to be taken which value to use as the initial guess. In this case, the literature values were used as initial parameters. The corresponding function call in *Mathematica* would then read

```
NonlinearModelFit[  y, {modelAir[{n, k}, x], {n > nlower, n < nupper, k >
    klower, k < kupper}}, {{n, nInit}, {k, kInit}}, x];
```

The lower (`nlower`, `klower`) and upper (`nupper`, `kupper`)bounds were set to let the result converge within a range $\|\texttt{n}-\texttt{nInit}\|, \|\texttt{k-kInit}\| < 1$. The model `modelAir` denotes that the substrate layer is fitted only with the surrounding medium of air (see above).

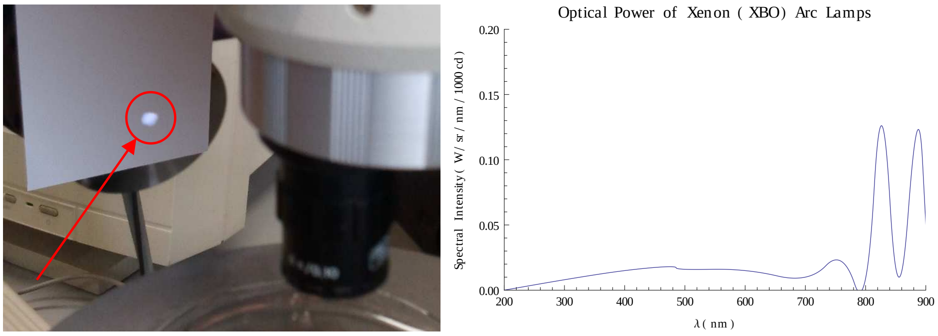

Figure 2.6: The ellipsometer uses a xenon-lamp as light emitter. The light spot is perceived as white (left), because the spectral intensity of a XE-lamp shows a nearly continuous emission over the complete visible range (right, reproduced from [35]). Its light is emitted arbitrarily polarised.

2.6 Results

Four metallic surface patches and two coins have been measured in the VIS with an ellipsometer, resulting in 1024 equidistantly sampled $\boldsymbol{\Psi}$- and $\boldsymbol{\Delta}$-values, Fig. 2.8 (left column). From the measured values, the reflectance ratios have been computed using the *Fundamental Equation of Ellipsometry*, Eqn. 2.1.

2.6.1 Anisotropy

At first, the material measurements were tested for anisotropic behaviour, i.e., the values change significantly with rotation of the patch around its surface normal. The patch was rotated $0°, 45°$ and $180°$ around and measured. The difference in value can be seen in a comparative plot for each incident angle and for $\boldsymbol{\Psi}$ and $\boldsymbol{\Delta}$ for the example of the copper sample, Fig. 2.7. The data suggest that the rotation around the surface normal does not affect the measured polarisation state in the VIS. Smaller deviations are only noticeable in the $\boldsymbol{\Psi}$- and $\boldsymbol{\Delta}$-plots for an incident angle of $70°$, but their extents remain within the margin of error. It is noticeable that the data becomes more noisy towards the IR. This can be explained by deviations of the spectral line of the XE-lamp from the ideal spectral line of XE. For further processing, the measurements captured at $0°$ were used.

2.6.2 Copper

The fitting of physically based rendering models is exemplarily described for the copper sample. From the measured $\boldsymbol{\Psi}$ and $\boldsymbol{\Delta}$ values, Fig. 2.8 (left), the squared reflectance

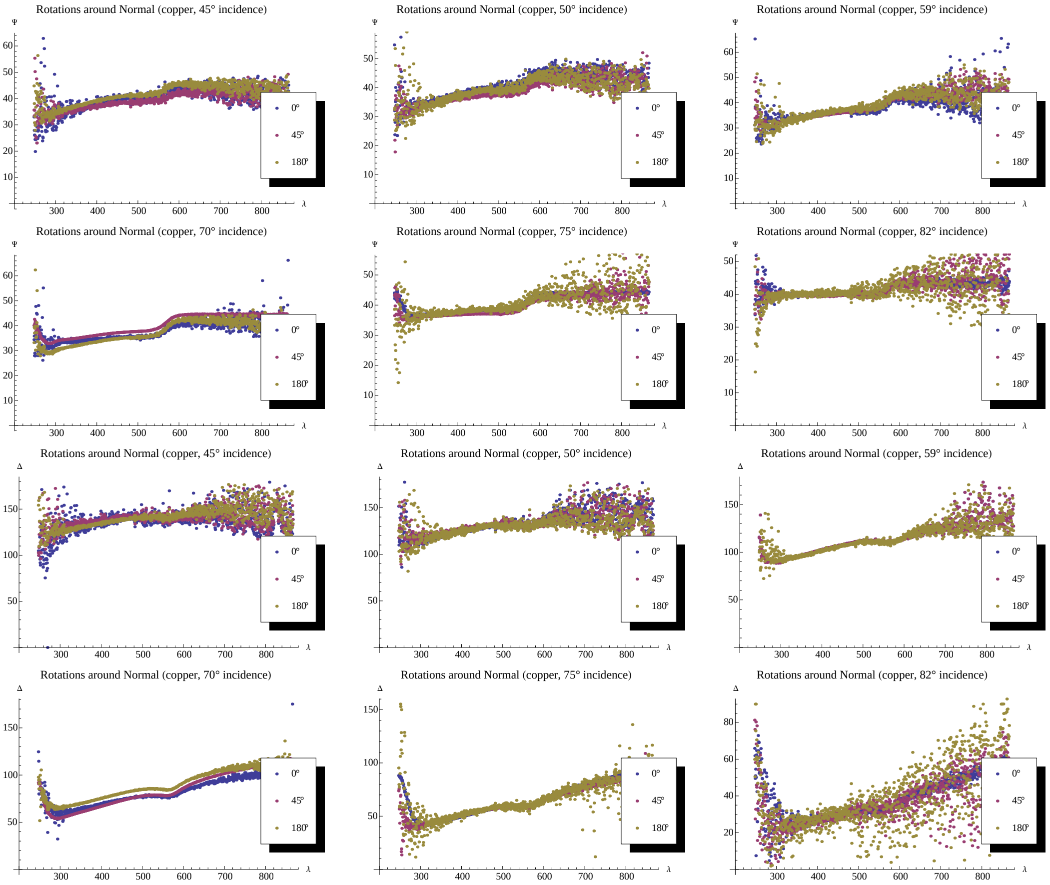

Figure 2.7: An evaluation of anisotropic behaviour reveals that the measured polarisation states do not change significantly. The upper two rows show the **Ψ**-values for copper, rotated $0°, 45°, 180°$ around the patch surface normal. The lower two rows show the **Δ**-values. It can be seen that the values in the VIS for all three surface rotations coincide mostly within a small margin of error. The measurements get more noisy towards the UV and IR. This can be explained by the fact that the XE-lamp has a slight deviation from the ideal profile in that range.

ratio $(\rho_{data})^2 = (\mathbf{\Psi} e^{i\mathbf{\Delta}})^2$ was computed and compared to the estimated reflectance ratio from the literature[110], Fig. 2.8 (middle).

The numerical fitting was performed with Mathematica's `NonLinearModelFit`to the Fresnel terms

$$Fr_{\perp} = \frac{(a - \cos(\theta))^2 + b^2}{(a + \cos(\theta))^2 + b^2}$$

$$Fr_{\parallel} = Fr_{\perp} \frac{(a - \sin(\theta))^2 + b^2}{(a + \sin(\theta)\ \tan(\theta))^2 + b^2}$$

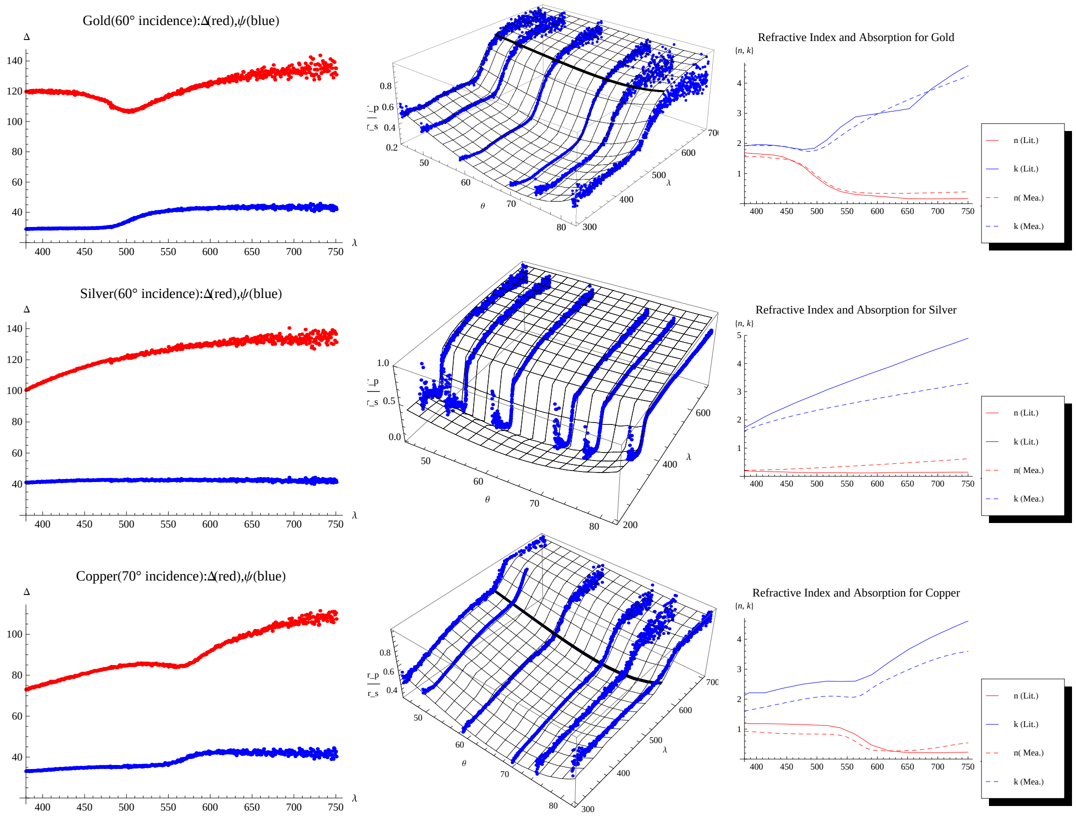

Figure 2.8: Gold (upper row) and silver (middle row) show a stable behaviour in the VIS (left column). The blue plot shows the $\boldsymbol{\Psi}$, the red plot shows the $\boldsymbol{\Delta}$ values for an inclination $\theta = 60°$. The reflectance ratios computed with Eqn.2.1 match the predicted behaviour by the Fresnel equations very accurately (middle column). In the right column an exemplary fit of the refractive index and absorption coefficient to the measured data is plotted against the data in the literature [86] for the VIS.

with

$$a^2 = \frac{1}{2}\sqrt{n^2 - k^2 - \sin^2(\theta) + 4n^2k^2} + (n^2 - k^2 - \sin^2(\theta))$$

$$b^2 = \frac{1}{2}\sqrt{n^2 - k^2 - \sin^2(\theta) + 4n^2k^2} - (n^2 - k^2 - \sin^2(\theta))\,.$$

The results are listed in Table 2.2.

A similar fit could be performed for gold and silver, but the sampling position has to be chosen carefully, Subsect. 2.6.3.

Figure 2.9: Care has to be taken when the sampling position on the coin sample is chosen. Some surface areas are in mint state, i.e., where the surface area has been plunger burnished it appears less diffuse. For example, a measurement of the silver sample at a position in the polished part of the texture results in slightly different results above 430nm (left plot) compared to unpolished parts (right plot).

2.6.3 Silver and gold

The measurement of the surface reflectance of gold and silver is affected by the position on the surface. Since the coins are in mint state, they exhibit both smooth and dull surface areas. An evaluation of the surface positions shows that the smooth surface areas additionally alter the polarisation states due to the burnishment of the plunger, Fig. 2.9 (left). The dull surface parts do not additionally alter the polarisation states and are favourable for a fit to the predicted values. Note that the coin was not cleaned or coated by a transparent film for protection, hence no interference phenomena of a transparent coating has occurred. The silver measurement shows a window transparency in the UV, not very far from the inferior boundary of the VIS (starting at 318 nm), which is also known in the literature [86], Fig. 2.8.

2.6.4 Aluminum

For anodised aluminium (E6) an interesting behaviour can be observed in the measured data. The plots for $\mathbf{\Psi}$ and $\mathbf{\Delta}$ oscillate over the measured spectrum, Fig. 2.10. Thus the computed reflectance ratio oscillates within the VIS, Fig. 2.10 (top right). A fitting comparable to the copper example could not be performed directly. An explanation of the effect could be that the Al_2O_3 oxide layer is situated on top of the aluminium surface in the manufacturing process. It can be accounted for by assuming a thin layer of 3μm on top of the substrate with known complex refractive index. For the substrate n_t was assumed to be $n_t = 0.11945$ and $k = 2.26534$ for $\lambda = 550$nm. The thin film is assumed to be porous aluminium oxide. Such a reflectance behaviour has to be modeled with a layered BRDF model, e.g. by incorporating Weidlich *et al.*'s approach [143]. Another explanation is that this kind of electro-deposition of the oxide

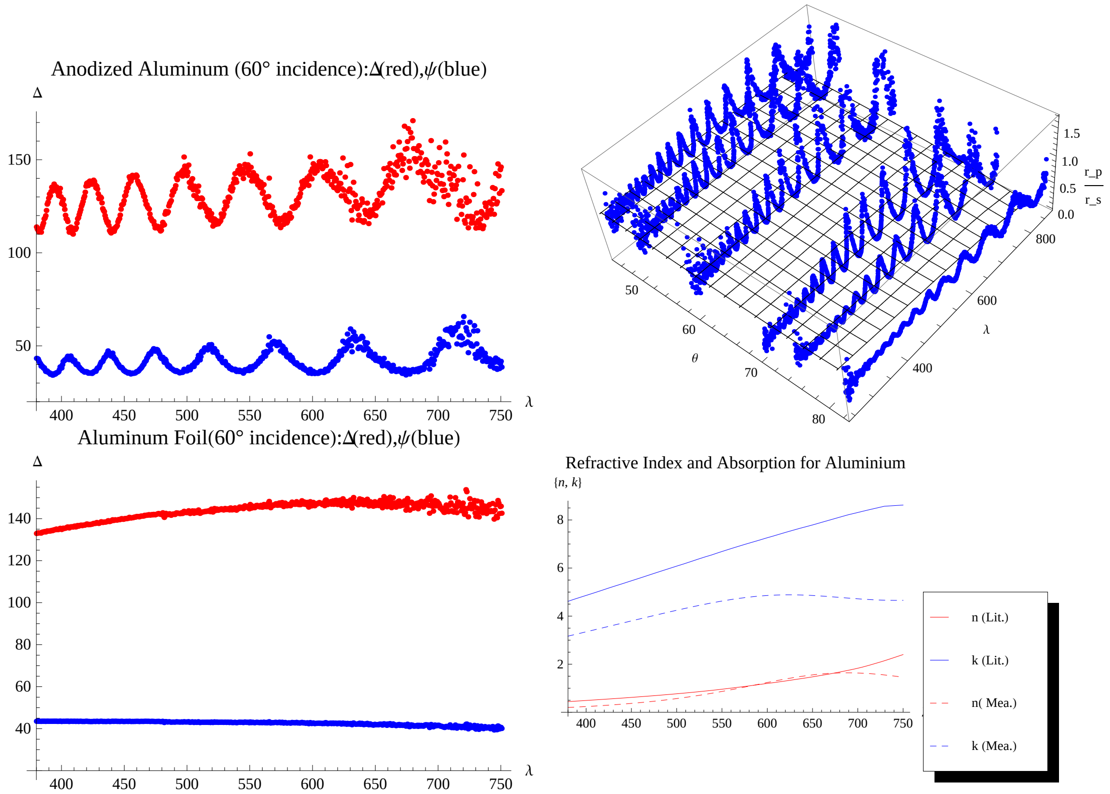

Figure 2.10: Anodised aluminium (E6) shows an oscillating behaviour in the VIS-range (top left). The blue plot shows the $\mathbf{\Psi}$, the red plot shows the $\mathbf{\Delta}$-values (in degree) for an inclination $\theta = 60°$. The reflectance ratios computed with Eqn.2.1 do not fit considerably well to the predicted behaviour according to the Fresnel equations (top right). This plot visualizes the reflectance ratios $\frac{r_p}{r_s}$ computed with Eqn.2.1 (blue dots) for varying inclination θ (in degree) and a wavelength λ (in nm). It does not match the reflectance ratios $\frac{Fr_\parallel}{Fr_\perp}$ of aluminium as stated in the literature [86] (black grid). Aluminium foil shows the expected behaviour in the measured range (bottom row).

on the parent metal produces a relatively uniform coating following the metallic surface profile.

When aluminium foil with a much thinner oxide layer is examined, instead, the computed reflectance ratio values approximately model the predicted behaviour, Fig. 2.10 (bottom right).

2.6.5 Galvanized steel and steel

Galvanized steel has a zinc coating that dominates reflectance behaviour. A fitting with the literature values for zinc could be performed, Fig. 2.11 (top right). The same holds

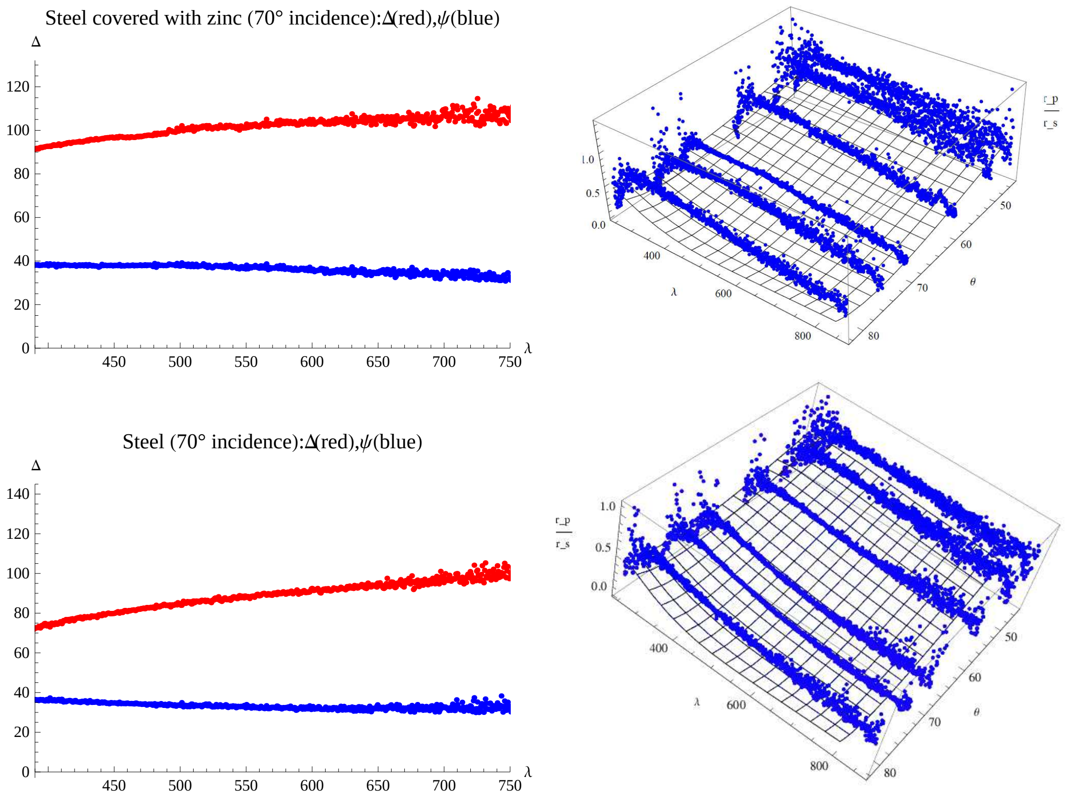

Figure 2.11: Galvanized steel shows the predicted behaviour in the VIS-range (top left). The blue plot shows the **Ψ-**, the red plot shows the **Δ**-values (in degrees) for an inclination $\theta = 70°$. The reflectance ratios computed with Eqn.2.1 do not fit considerably well to the behaviour predicted by the Fresnel equations (top right). This plot visualizes the reflectance ratios $\frac{r_p}{r_s}$ computed with Eqn.2.1 (blue dots) for varying inclination θ (in degree) and a wavelength λ (in nm). It matches the reflectance ratios $\frac{Fr_{\parallel}}{Fr_{\perp}}$ of zinc as stated in the literature [86] (black grid). The same holds for bare steel. Note the decrease in the **Δ**-value in the range $380 - 480$nm.

for bare steel. A slight decrease in value is noticeable in the **Ψ**- and **Δ**-plot within the range $380 - 480$nm.

2.6.6 Comparative table

To provide a comparison to the literature values, a fitting for a particular wavelength is provided, Table 2.2. Weaver *et al.* [141] list the following values for refractive indices: Copper at 516.6nm has a refractive index of $n = 1.120$ and $k = 2.599$. Silver at 516.6nm has a refractive index of $n = 0.240$ and $k = 3.090$. Gold at 516.6nm has a refractive

Fresnel terms						
	Copper $\lambda = 516$nm	Galv. Steel $\lambda = 500$nm	Steel $\lambda = 500$nm	Alum. Foil $\lambda = 516$nm	Gold $\lambda = 516$nm	Silver $\lambda = 495$nm
n	1.030	3.708	2.400	0.875	0.549	0.29
k	2.460	4.721	3.699	6.233	1.810	3.04

Torrance-Sparrow BRDF with Blinn-Phong microfacet distribution						
	Copper $\lambda = 516$nm	Galv. Steel $\lambda = 500$nm	Steel $\lambda = 500$nm	Alum. Foil $\lambda = 516$nm	Gold $\lambda = 516$nm	Silver $\lambda = 495$nm
n	1.032	3.708	2.400	0.875	0.549	0.289
k	2.459	4.721	3.700	6.233	1.810	3.040
β	0.786	0.867	0.255	0.637	0.443	0.793

Torrance-Sparrow BRDF with Gaussian microfacet distribution						
	Copper $\lambda = 516$nm	Galv. Steel $\lambda = 500$nm	Steel $\lambda = 500$nm	Alum. Foil $\lambda = 516$nm	Gold $\lambda = 516$nm	Silver $\lambda = 495$nm
n	1.232	3.708	2.471	0.876	0.55	0.289
k	2.458	4.721	3.500	6.233	1.81	3.04
β	0.358	0.213	0.307	0.438	0.218	0.825

Torrance-Sparrow BRDF with Beckmann microfacet distribution						
	Copper $\lambda = 516$nm	Galv. Steel $\lambda = 500$nm	Steel $\lambda = 500$nm	Alum. Foil $\lambda = 516$nm	Gold $\lambda = 516$nm	Silver $\lambda = 495$nm
n	1.032	3.708	2.400	0.875	0.549	0.289
k	2.459	4.721	3.700	6.233	1.810	3.04
β	0.786	0.867	1.180	0.637	0.866	0.793

Torrance-Sparrow BRDF with Trowbridge and Reitz microfacet distribution						
	Copper $\lambda = 516$nm	Galv. Steel $\lambda = 500$nm	Steel $\lambda = 500$nm	Alum. Foil $\lambda = 516$nm	Gold $\lambda = 516$nm	Silver $\lambda = 495$nm
n	1.232	3.708	2.471	0.875	0.55	0.289
k	2.458	4.721	3.500	6.233	1.81	3.040
β	0.187	0.259	0.246	0.501	0.185	0.736

Table 2.2: The Fresnel terms and Torrance-Sparrow BRDF with different microfacet distributions have been fitted for $\lambda = 516$nm (Copper, Aluminum, Gold), $\lambda = 495$nm (Silver) and $\lambda = 500$nm (Steel, Galvanized Steel) using Mathematica's `NonLinearModelFit`. The parameter n is the refractive index, k is the extinction coefficient, and β models the microfacet distribution's surface roughness. For each material the initial guess for n, k is provided from the literature [86].

index of $n = 0.500$ and $k = 1.860$. Aluminium at 516.6nm has a refractive index of $n = 0.8263$ and $k = 6.283$. The table lists fitting results for the Torrance-Sparrow [131]

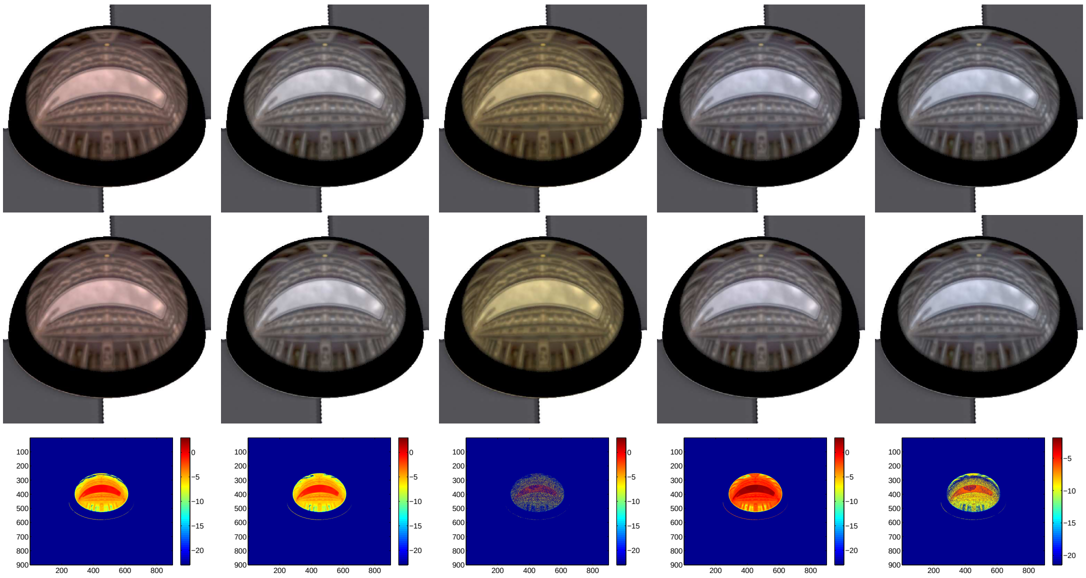

Figure 2.12: Renderings based on the measurements (top, cropped) and literature models (middle, cropped) show only subtle differences (bottom, uncropped HDR images compared). For comparison, a scene is rendered consisting of a sphere on a checkerboard illuminated by the Uffizi light probe [36]. The first row shows the spheres which have a coating with n, k values fitted to the ellipsometric measurement data. The second row shows the coating as stated in the literature [86]. The third row shows the per pixel intensity difference on log-scale. From left to right: copper, silver, gold, aluminium, zinc. The images were rendered with PBRT 2.0 [112] and tonemapped with Durand's algorithm [43] for display.

model with different microfacet distributions D_n:

$$r_i = \frac{1}{4\cos(\theta_o)\cos(\theta_i)} * Fr_i * G(\theta_o, \theta_i) * D_n \tag{2.2}$$

with geometric term G for shadowing of illuminating rays and masking of absorbed viewing rays and where $i \in \{\perp, \|\}$. In the fitting procedure G was set to a constant value and n would vary over the following microfacet distributions: Blinn-Phong [16], Gaussian [131], Beckmann [9], Trowbridge and Reitz [134]. The fitting procedure took $0.03s$ per sample and per distribution on a Intel$^{\circledR}$Core$^{\text{TM}}$2Quad CPU at 2.66GHz with 3.8 GB memory.

2.6.7 Rendering

With the results, virtual scenes that exhibit metallic surfaces can be realistically synthesised. An exemplary scene obtaining an object with the material properties stated in the literature is contrasted with the same scene with material properties fitted to the performed measurements. The scene consists of a half-sphere on a checkerboard-textured plane and is illuminated with the 1500 × 1500px Uffizi high dynamic range light probe [36], as provided by Paul Debevec [37]. The light probe has a dynamic range 500 : 1. The half-spheres were chosen because they cover a broad range of incident and exitant angles for one viewpoint and a fixed lighting environment. The surface roughness was held low ($\beta = 0.0001$), to set a visual focus on the effects of mirroring directions. Since the measured data fit the predicted values in the literature for all samples except anodised aluminium, the perceived visual difference is negligible, Fig. 2.12. In most regions, the intensity difference is in the margins of numeric inaccuracy ($\epsilon = 10^{-12}$). The images were rendered with PBRT, version 2.0 [112]. Note that the first and second row of Fig. 2.12 were tonemapped for display with Durand's algorithm [43], thus perceived colors may not necessarily represent the measured values accurately.

2.6.8 Limitations

Using an ellipsometer for taking the measurement has the limitation that only mirroring directions can be sampled. Its measurement range is limited between 45° and $\approx 85°$. The accuracy of the measured values is influenced by the calibration of the light source, the polarising units and the placement of the sample. The measurement times per sample are considerably long (ranging from $10s$ up to $60s$ per point). Before each measurement, an evaluation of the intensity of the emitted light is necessary to provide signal strength. Thus, several minutes for fine-tuning the height of the sample, the apertures of the emitter and the receiver were necessary.

Numerical inaccuracies in the order of 10^{-16} may affect the computation of the reflectance ratio and the system of equations is overdetermined.

Compared to polarimetry, the employed approach does not provide a complete Mueller Matrix.

2.7 Discussion

With the ellipsometer, an alternative measuring technique has been introduced to the field of computer graphics to capture reflectance data of real-world metallic surfaces, taking into account the electromagnetic field behaviour of light. The reason for this is the validation of existing models that are considered to be physically plausible. It has been applied to a number of commodity metallic surfaces, patches and coins. The subset comprised copper, anodised aluminium, steel, galvanized steel, gold and silver.

The ellipsometer measured the introduced change in phase and amplitude. With the *Fundamental Equation of Ellipsometry*, the complex reflectance ratios have been computed. A fit of the reflectance ratios from measured polarisation values to the literature reflectance showed that all metallic surfaces except anodised aluminium displayed the predicted behaviour. Anodised aluminium instead showed oscillatory behaviour over the measured range, which can be explained by its thin oxide layer.

2.7.1 Integration into the predictive rendering pipeline

The verification of the Torrance-Sparrow model for metallic surfaces addresses the modeling part of the predictive rendering pipeline and provides another method and tool to compute the accuracy of a physically plausible model, regularly employed in the pipeline, for a set of real-world surfaces. It can be used to verify other reflectance models, assumed to be physically plausible, for other materials that exhibit polarising behaviour, as well.

3

Light-surface interaction: Reflectance models for immersed materials

3.1 Introduction

The goal of surface reflectance modeling is to provide mathematical functions that approximate natural light-surface interaction behaviour as closely as possible and that are easily to compute on state-of-the-art graphics hardware. This property distinguishes them from lookup-tables, which provide accurate reflectance values within the error of measurement, but are expensive to store or access during (real-time) rendering. The functions can either be deduced from physical properties of the surface to be modeled (Lorentz dipole-oscillator model, Fresnel reflectance behaviour) or inferred from observations in a measurement setup (by performing a χ^2-fit to the measurement data, again within the error of measurement). This chapter will focus on inferring a suitable reflectance model based on observations made in a newly designed measurement setup. The setup is tailored to place small surface patches along the perimeter of a cylindrical glass tank, that is filled with different fluids of known refractive index in order to measure light-surface interaction for different surrounding media. The light is shone from a trichromatic laser from different angles onto the surface of the immersed patch, but always orthogonal to the surface of the glass cylinder to avoid unwanted refraction at the glass boundaries, Fig. 3.1. The calibration of the laser to the surface of the cylinder is performed by inserting a small mirror patch at the perimeter of the glass cylinder and fine-adjusting the laser so that the spot is reflected with minimal deviation from the incident angle.

Theoretically, surface reflectance has to be measured within a hemisphere, filled with water and the surface patch intersecting the sphere's centre, Fig. 3.2. In practice, this setup is relatively complicated to realise. The glass half-dome would have to be as exact as possible with respect to the distance of each surface point to the sphere's centre. This requires a special glass object similar to a snow dome to be manufactured for this purpose.

In addition, the laser would have to be mounted on a gantry that could be moved in a half-sphere around the patch to span all incoming angles. The calibration of the gantry to the sphere would have to be very accurate, because small deviations would lead to large light path displacements. Thus, the point on the surface patch illuminated by the laser light would move within an undefined range, thus inhibiting the ability to measure textured patches or patches that feature a svBRDF, which are most common in nature. Having these liabilities in mind the setup is constrained to a laser moving along a line, spanning the azimuthal angles, which allowed us to use a Schott glass cylinder instead of a special glass dome not available on the market. The calibration of the laser becomes feasible. The inserted object only has to be placed at the perimeter of the glass cylinder. A holder is designed and printed with a 3D printer. The holder consists of a cap fitting exactly the circumference of the cylinder and of two shafts to guide the sample through the diameter of the cap. A plug would then fix the sample from below, preventing it from sliding out, Fig. 3.3. Part of this chapter has been published at the *16th International Workshop on Vision, Modeling, Visualization 2011* [13].

3.2 Related work

The interaction of water with surfaces has been addressed by some papers beforehand. Lu et al. [84] describe the geometry-based drying process of objects on which water has been spilled. Sun *et al.* [130] describe a time-varying BRDF (tvBRDF), for example dust accumulation and the drying of spray and oil paint. Gu *et al.* [56] describe a thin-layer BTDF model for rendering dirty and contaminated glass.

All previously presented methods do not account for intensity changes of reflected light for submerged surfaces. This thesis addresses this gap and presents a suitable microfacet-based BRDF model and a method to measure data for materials whose reflectance behaviour is governed by this effect.

Recently, Dana *et al.* [32] proposed a new method of watermarking with the use of BRDFs. They introduce a new device to illuminate a sample with unknown refractive

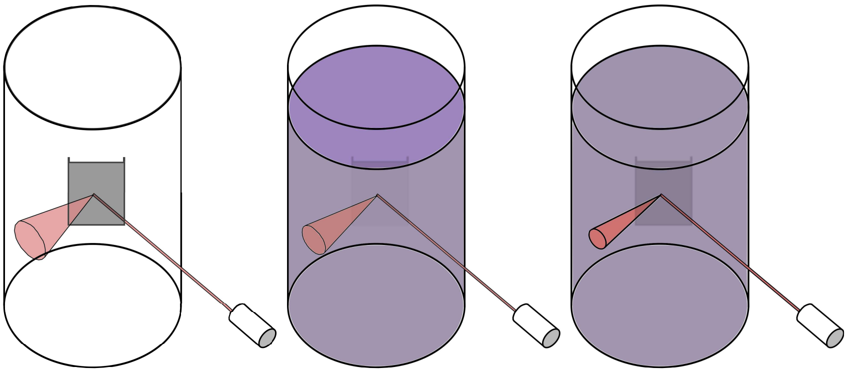

Figure 3.1: The conjecture of this chapter is that the intensity and extent of the reflected light are dependent on the surrounding medium. It is proposed to measure the effect by immersing a surface patch at the perimeter of a cylindrical tank filled with different surrounding media, e.g. air (left) or transparent fluids of known refractive indices (middle and right - indicated by colouring). A laser is rotating around the cylinder, the centre of rotation lies in the cylinder's main axis, thus the light path deviation at the boundary of the glass is minimized. Theoretically, the reflected light cone hits the surface of the cylinder orthogonally at any point.

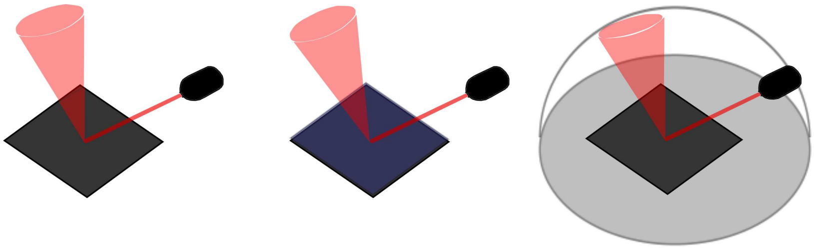

Figure 3.2: The objective behind capturing the reflectance of objects immersed in media compared to traditional reflectance capturing (left) is to illuminate them through a layer of the refractive medium (middle). This constraint raises interesting issues: The refractive medium would bend the light rays at any boundary crossing except for orthogonal crossing. Consequently, in theory, the medium would have to be enclosed in a transparent half-dome, e.g. manufactured glass, with the centre of the half-dome lying in the plane of the object surface (right).

index from various angular directions. At the same time, the reflected intensities for various angular directions are captured in order to find the minimal intensity for a range of angles and thus the Brewster angle. From that, they can estimate the refractive index of the material. Their setup is manufactured and designed to have two confocal parabolic mirrors, thus mapping angular directions to positions on the mirror surface, which then has to be simply captured by a camera and evaluated for the position of the

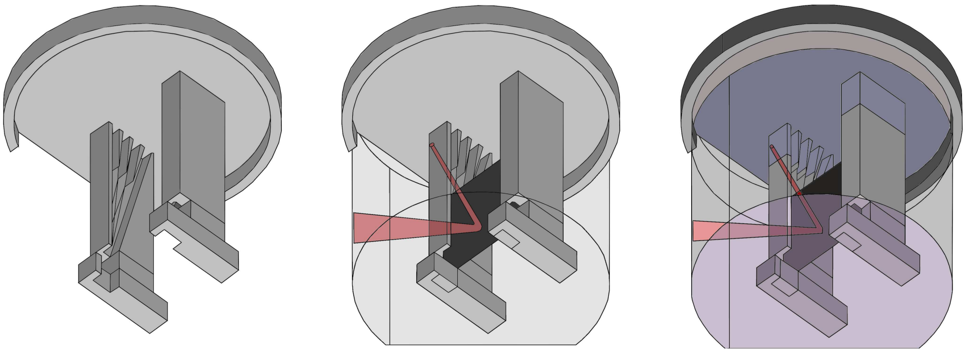

Figure 3.3: A suitable holder to fix a generic sample of defined depth at the perimeter of the cylindrical glass tank is printed out (left). A laser light, shone perpendicularly onto the surface of the cylinder would hit the surface patch at the centre point (middle). The reflected light cone would hit the glass surface orthogonally. A change in the surrounding medium (e.g. by inserting water, right, colour indicates different refractive index) would result in a change in the reflected light cone.

intensity maximum. Their illumination angles usually vary between 50° and 60°. The computation of the refractive index is either performed by assuming the refractive index is proportional to the tangens of the Brewster angle or it is performed by employing the Levenberg-Marquardt method. Their set of samples spans an optical grade glass and liquids with distinct refractive index values, ranging from $n_i = 1.33$ to $n_i = 1.7$. The employed liquids are deliberately chosen to be non-toxic and non-hazardous. The main benefit of their approach is a comparatively simple mapping from the position of maximum intensity to the refractive index. No rotation stage or robotic arm is needed to vary the incident and exitant light directions.

On the contrary, their method does not evaluate the reflectance of a different set of objects immersed into the above-mentioned set of media and thus does not elaborate on the question of whether the media would have an effect on the reflectance of samples immersed into them. While the setup is designed in an elegant way for mapping angles to pixel positions, in their current setup it is limited to a one-dimensional sampling of the reflected light. In the approach evaluated in the thesis, both the azimuth and elevation of the reflected light cone are considered.

Small *et al.* [129] investigated moistening and drying effects on granular media, like sand on samples taken from the *Ganges-Brahmaputra* delta. Their measurement involved placing the granular sample in a watched glass, that may be vibrated slightly for flattening the granular surface. Under the watch glass for each measurement, a Spectralon and a black paper were placed for calibration purposes. The samples were

	Elaborated setup	Time-varying processes	n_i of surrounding medium	Model proposition
Evaluated setup	-	-	✓	✓
Dana *et al.* [32]	✓	-	✓	-
Gu *et al.* [56]	✓	-	-	-
Lu *et al.* [84]	✓	✓	-	-
Small *et al.* [129]	✓	✓	-	-

Table 3.1: Comparison of related work to this approach: while some approaches concentrate on time-varying processes of contaminated surfaces [84, 129], others lay their focus on estimating the refractive index of the medium [32]. The evaluated approach incorporates the refractive index of the medium to measure its effects on the surface reflectance of immersed materials. Time-varying processes are excluded.

rotated four times at 90° around the glass surface normal to rule out geometrical effects. A spectroradiometer served as a measurement device for the samples, a halogen light bulb provided the illumination. One of their results was that moistening on sand has not only distinctive effects on the perceived reflectance, but that the amount of reflectance increases highly nonlinearly with proceeding drying time. Still, the reflectance curve cannot be classified as exponential. Besides, the reflectance increased linearly during the first, third and the last quarter of the measurement period. A discrimination in the measurement between fine and coarse sand samples reveals that temporal extent of the drying process is higher for coarse-granular samples, but the process incorporates a better distinguishable linear time span.

Still, their method does not evaluate reflectance differences for varying refractive media. Although a classification between reflectance of air ($n_i = 1.0$) and of water ($n_i = 1.33$) can be stated, no model is presented that incorporates the refractive index of the surrounding medium. Their setup does not vary the incident or exitant angles for sample spots. Furthermore, granular objects that may obtain mesoscalar surface variances are the only set of materials under investigation. No comparison is made to layered plastics or porous surfaces. Thin layer effects may also alter the measurement effects in their experiment.

3.3 Fresnel reflection and transmission

Fresnel reflection and transmission are the main factors in these models that influence non-diffuse surface appearance. They are generally of the form [63]:

$$f_r = \alpha_s \rho_s + \alpha_{dd} \rho_{dd} + \alpha_{ud} \rho_{ud}, \tag{3.1}$$

where α_s, α_{dd} and α_{ud} are the multiplicative colour factors and ρ_s denotes perfect specular reflectance, ρ_{dd} directionally diffuse reflectance, ρ_{ud} perfect Lambertian reflectance, and f_r is the resulting BRDF. The specular and directionally diffuse terms are influenced by Fresnel reflection which enters the equation

$$\begin{aligned} \rho_s &= F_r \cdot L_i \\ \rho_{dd} &= F_r \cdot D \cdot S, \end{aligned}$$

as a multiplicative factor where L_i is the incident radiance, D is the statistical microfacet distribution, S is the shadowing term, and F_r is the Fresnel reflection coefficient, as defined in Sect. 1.2.4.

3.4 Measurement device

As the surface reflectance is to be measured for immersed surface patches, the patches have to be placed in a suitable tank, and the light has to be shone at the correct angle onto the surface. Finally, the reflected light has to be captured accordingly. Thus, a holder is printed in 3D [118] to hold the measured sample at the perimeter of a glass cylinder. The exitant point of the laser light, in this case the upper end of the fibre cable, is attached to the arm of a rotation stage. In this setup, a Zaber T-RS60 [149] rotation stage is employed because it is steerable to sub-degree accuracy. The centre of the rotation stage coincided with the main axis of the cylinder, such that the laser light hits both the surface patch at approximately the same point and the glass surface orthogonally at the same time. The reflected light is transmitted by a diffuse screen, such that the image is formed directly on the surface of the glass cylinder.

First, the image formation in the measurement device is discussed.

The radiance reflected from the sample is given by

$$L_o^r(\omega_o^r) = L_i^r(\omega_i^r) f_r(\omega_i^r, \omega_o^r) \cos(\theta_i^r) \Delta\omega_i^r. \tag{3.2}$$

Assuming that the incoming radiance L_i^r is approximately constant as opposed to a Gaussian over a small solid angle $\Delta\omega_i^r$, the integration is reduced to a simple multiplication. Similarly, the radiance registered by the camera is

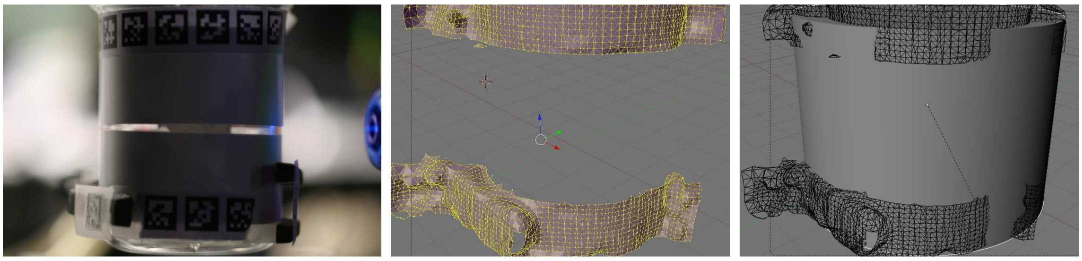

Figure 3.4: The implemented setup consists of the 3D printout, a Schott glass cylinder with screen attached, a trichromatic Laser, the Zaber T-RS60 [149] rotation stage, and a Canon EOS 5D Mark II to capture the screen. The centre of the rotation stage approximately coincides with the main axis of the cylinder (left). After reconstructing the 3D positions of the fiducidal markers (middle, visualized with Blender), the screen is fitted by aligning a parameterized cylinder to the spots (right, visualized with Blender).

$$L_c = L^t_o(\omega^t_o) = L^t_i(\omega^t_i) f_t(\omega^t_i, \omega^t_o) \cos(\theta^t_i) \Delta\omega^t_i, \tag{3.3}$$

and, as in the previous case, $L^t_i(\omega^t_i)$ is assumed to be constant over $\Delta\omega^t_i$. This is only an approximation since the laser spot usually exhibits a Gaussian profile. Note that $\Delta\omega^r_i$ varies with $\cos(\omega_i)$ due to projected area foreshortening. Setting $\Delta\omega^t_i = \cos(\theta^r_o) \cdot c_0$, the cosine multiplied by a diffuse constant c_0 and combining Eqs. 3.2 and 3.3, it can be found that

$$L_c = L^r_i(\omega^r_i) f_t(\omega^t_i, \omega^t_o) f_r(\omega^r_i, \omega^r_o) \cos(\theta^t_i) \cos(\theta^t_o) \cos(\theta^r_i) c_0. \tag{3.4}$$

This equation describes the recorded radiance due to a sample illuminated by a laser from direction ω^r_i.

Now, the measurement is performed with the *calibration sample*. The reference measurement is obtained

$$L^{Spectralon}_c = L^r_i(\omega^r_i) f_t(\omega^t_i, \omega^t_o) \frac{1}{\rho} \cos(\theta^t_i) \cos(\theta^t_o) \cos(\theta^r_i) c_0, \tag{3.5}$$

where $\frac{1}{\rho} \approx 0.99 \cdot \frac{1}{4\pi}$ is the BRDF of Spectralon [102]. Now, taking an arbitrary BRDF measurement, Eqn. 3.4, and dividing it by the Spectralon reference measurement, Eqn. 3.5, the geometric terms cancel out and one obtains

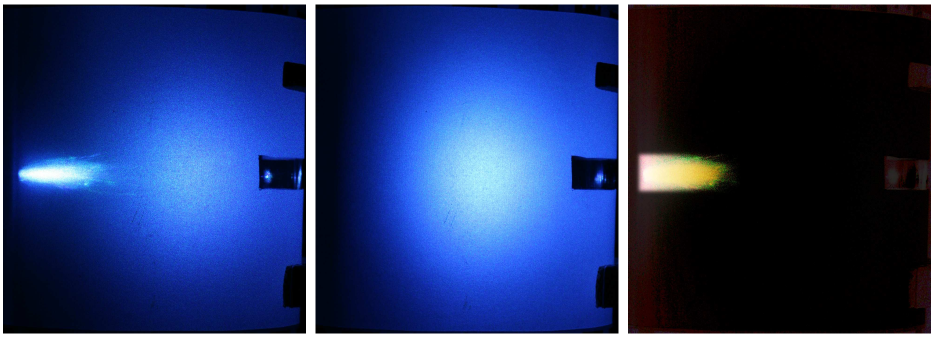

Figure 3.5: An LDR input image of the reflectance of white plastic in air (left) obtains transmittance modulation by the screen. With a spectralon (middle) the screen is diffusely illuminated from within the cylinder. Simple normalisation and subtraction with the Spectralon capturing eliminates the modulation by the screen (right, false-colored image).

$$f_r = \rho \cdot \frac{L_c}{L_c^{Spectralon}}, \tag{3.6}$$

i.e., one can directly measure a value proportional to the BRDF of the sample, Fig. 3.5. Since a full slice of the BRDF is recorded for every incident angle of the laser, one should perform the calibration for every laser angle. This is not strictly necessary since the diffuse BRDF of Spectralon does not vary with the incident angle. Note that the diffuse constant c_0 has to be fitted to the measured data, e.g. with a BRDF model, that differentiates between specularity and diffusity. The speckle noise introduced from the trichromatic laser was noticeable with the bare human eye, but it was smoothed out in the downsampling process of the pipeline, so that no disturbance was introduced on the model.

3.5 Materials

A total amount of 15 materials have been measured. Since two materials are known for their anisotropic reflectance behaviour, both were measured in horizontal and vertical directions to account for anisotropy. All materials can be sorted into one of the following subclasses: single layer materials (plastic, stone), multiple layered materials (cloth, ceramics, vine glass), particle-based (acrylic paint, oil paint), metallic surfaces (aluminium) and porous materials (bamboo, sandpaper, wood). In Fig. 3.6, a collection of the materials is shown which provides a considerably wide variation for analysis.

Figure 3.6: For the measurements, a broad set of multiple layered, particle-based, metallic and porous materials was used (see captions).

3.6 Refractive media

As refractive medium, different salt solutions ranging from $n_i = 1.33$ to $n_i = 1.45$ were used: destilled water ($n_i = 1.33$) and salt solutions exhibiting $n_i = 1.35$, $n_i = 1.37$, $n_i = 1.39$, $n_i = 1.42$ and $n_i = 1.44$, respectively. Additionally, dry measurements were performed, i.e., with the refractive index of air $n_i \approx 1.0$. Compounded fluids with a refractive index greater than $n_i = 1.44$ would be possible, e.g. by solving sucrose in water, but the fluid would be metastable and could sulphur at any instant. Similar surrounding media could be provided by other resolvents, e.g. 2-Propanol ($n_i = 1,37$), 2-Butanol ($n_i = 1,39$) or 1-Hexanol ($n_i = 1,415$), but they are harmful to the human

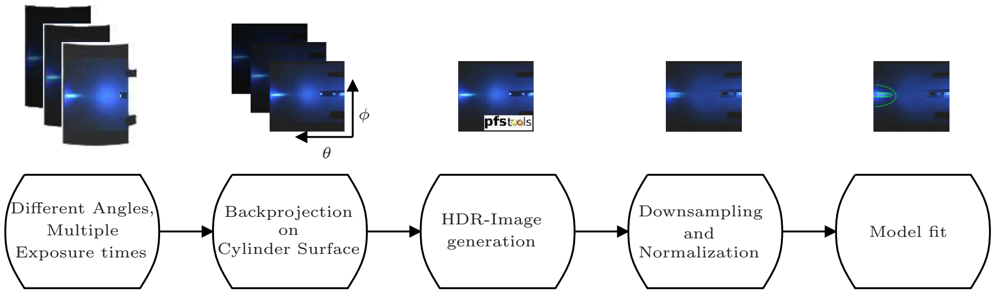

Figure 3.7: The processing pipeline for the imaged reflectances: After capturing, the images are backprojected to the cylinder surface, transformed to HDR [89], and downsampled. Finally, the model is fitted to the data.

respiratory system and thus hamper the experimental setup.

3.7 Processing pipeline

The images are captured for varying incident angles and varying exposure values. The images are then backprojected to the cylinder surface, transformed to HDR [89] and downsampled. Finally, the model is fitted to the data.

3.7.1 Angular sampling

To provide a dense sampling over the hemisphere, all material reflectances have been captured for different incident angles between 5° and 85°, elevation in 5° steps w.r.t. the surface normal.

3.7.2 Reprojection and normalisation

The following pipeline is performed for each material and each refractive medium: for each incident angle, the screen is imaged with a Canon EOS 5d Mark II at different Exposure Value (EV) (20 EV; 18 EV; 16 EV; 14 EV; 13 EV; 10 EV; 8EV) to account for the dynamic range of the reflected laser light. The resulting images of size 2496×1800px for each incident angle are backprojected [45] onto the surface of a cylinder, which is fitted once at the beginning with Random Sample Consensus (RANSAC) [47] to the reconstructed geometry of the setup, in this case 3D positions of fiducidal markers [125]. Sparse bundle adjustment was employed as reconstruction procedure [2]. The surface texture is used for further processing. At this point in the pipeline, the coordinate axes of an image are proportionally related to inclination angle θ and azimuth angle ϕ of the reflected light cone, which is necessary for accurate fitting. Then, the backprojected images are combined to one HDR image [89] which is then normalized to account for the screen transmission properties and downsampled to size 249 × 180 px; a pixel approximately corresponds to 0.2° × 0.2°. The resulting image is stored according to the corresponding incident angle, Fig. 3.7.

3.8 Proposed model

To account for the refractive index in bidirectional scattering distribution function the Torrance-Sparrow BRDF model for microfacet distributions is generalised. The refractive index of the surrounding medium n_i contributes to the Fresnel term for non-diffuse surface appearances. Thus, the proposed model reads

$$f_r(\omega_i, \omega_o, n_i, n_t) = \rho_d + \rho_s \frac{F_r(n_i, n_t) \cdot D(\omega_i, \omega_o) \cdot G(\omega_i, \omega_o)}{(4 \cdot \omega_i \cdot \omega_o)} \tag{3.7}$$

where D is the microfacet distribution, e.g. a Blinn distribution [15], and G is the geometric attenuation term. The refractive index of the surrounding medium n_i and the index of the test material n_t enter the Fresnel term $Fr(n_i, n_t)$ and modulate the appearance of the lobe. This refractive index-dependent bidirectional scattering distribution model is a general way to represent materials with a given material index n_t that change the reflective and transmissive behaviour according to the Fresnel equation. The parameter ρ_d accounts for the diffusely scattered light, while ρ_s modulates the specular term. In the microfacet distribution D, the paramater e accounts for surface roughness. The parameter n_t models the refractive index of the substrate, i.e., the immersed material. Even if it appears counterintuitive at first sight, each material can be assigned a refractive index. The refractive index n_i of the surrounding medium is treated as an input variable.

3.9 Fitting procedure

The proposed BRDF model is evaluated with the captured data for each acquired material. The fitting is based on Levenberg-Marquard optimization [90] and optimizes the parameters ρ_d,ρ_s,n_t and the exponent of the microfacet distribution, Eqn. 3.7. The Blinn microfacet distribution was chosen for exemplary fit.

Then the mean intensity of the diffusely scattered light is calculated for each measured refractive index and assigned to ρ_d. The parameter ρ_s is initially assigned the mean intensity value of the reflected light, i.e., $\omega_o = \omega_i$, for each measured refractive index. The index of the material is assigned to n_t. For the initial damping parameter $\tau = 0.1$ and for the convergence criterion $\epsilon_1 = \epsilon_2 = 10^{-6}$, as proposed by Madsen *et al.* [87]. The fitting typically converges after about 20 iterations.

3.10 Results

With the capturing of immersed materials, different results could be obtained. A subclass of materials showed the assumed reflectance behaviour. The visual results are shown for two materials, plastic and cloth. Other materials showed no measurable difference in the reflectance behaviour for varying refractive index of the surrounding medium.

3.10.1 Red plastic

The most prominent visual result could be achieved for the plastic sample, Fig. 3.8. A difference in extent and intensity between the sample immersed in air and the same sample immersed in a salt solution with $n_i = 1.44$ can be observed from the reprojected images without further processing. It is obvious that the highest decrease in extent is noticeable between the patch immersed in air ($n_i = 1.0$) and the salt solution ($n_i = 1.44$). The dominant transmittance of the screen exhibits a red tinge and reveals the colour of the plastic sample. It can also be noticed that in air, the lower intense areas of the reflected lobe show an asymmetric non-convex shape. This is assumed to be caused by the dominant influence of surface roughness on the reflected light in comparison to the influence of the Fresnel term for a surrounding medium of air. For near-grazing angles, the off-specular areas near the mirroring position obtain a blue tinge, which is reasoned by the dominance of the reflectance over colour for low elevation angles, cf. copper coins near grazing angles [83].

3.10.2 Cloth

Less obvious results are retrieved for cloth. The diffusely reflected light dominates the measurement, Fig. 3.9, but its intensity decreases gradually with increasing n_i. For near-grazing angles, the decrease in the extent is clearly visible, e.g. at 5° elevation for surrounding medium air and distilled water. This is assumed to be explained by dominant self-shadowing effects near grazing angles [34]. The structure of the fabric introduces small intensity variations in the measurement, e.g. at 25° elevation at $n_i = 1.42$ and $n_i = 1.44$.

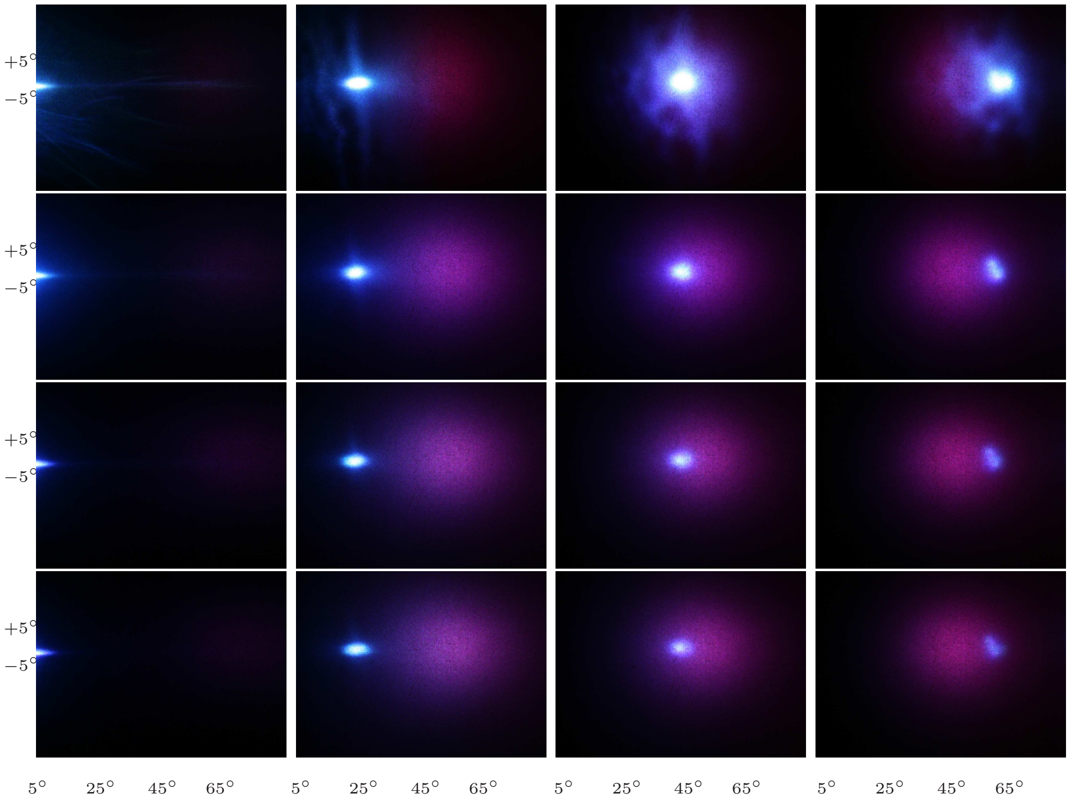

Figure 3.8: The incident angles 5°, 25°, 45° and 65° elevation w.r.t. the surface normal, are captured and reprojected for the red plastic material in air (top row) and immersed in water (second row), a salt solution with $n_i = 1.42$ and a salt solution with $n_i = 1.44$. The intensity and extent of the reflected lobe decrease with increasing n_i (c.f. top and second row). The images are depicted before normalisation.

3.10.3 Alignment

Small deviations from the ideal meridian, i.e., the great circle on the plane of incidence spanned by the surface normal and the incident vector with the lowest elevation, may occur due to damped vibrations of the laser holder introduced by the rotation stage after an angular motion, Fig. 3.10. They are recognised by finding the geometric mean of the pixel that obtain 95% or more of the maximum intensity and shifting the image circularly so that the y-value of the mean coincides with the y-value of the meridian line.

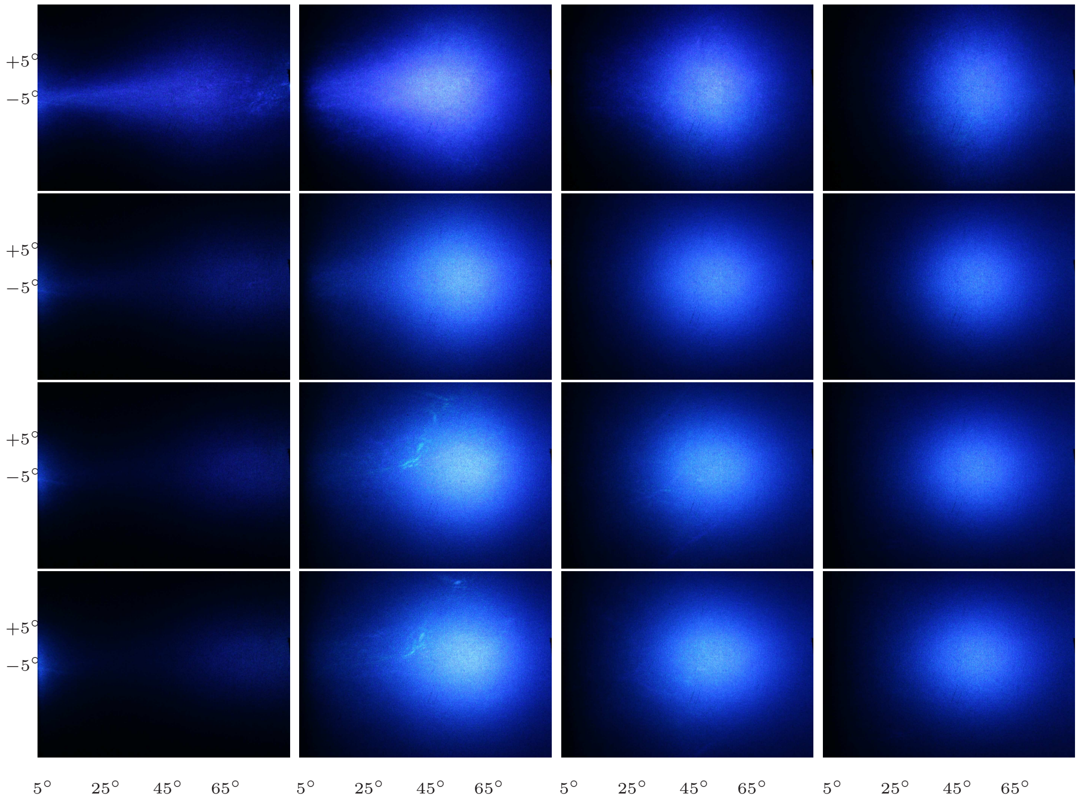

Figure 3.9: The incident angles 5°, 25°, 45° and 65° elevation w.r.t. the surface normal, are captured and reprojected for the cloth material in air (top row) and immersed in water (second row), a salt solution with $n_i = 1.42$ and a salt solution with $n_i = 1.44$. While a decrease in intensity and extent of the reflected lobe with increasing n_i is still noticeable (c.f. top and second row), the overall perceived difference remains small. The fibre structure introduces small intensity variations (c.f. 25°, third and fourth row). The images are prior before normalisation.

3.10.4 Fitting

In the first step, the proposed BRDF model is fitted to the captured BRDF data using the Levenberg-Marquardt algorithm [90]. The following classes of materials are captured: acrylic paint, aluminium, bamboo, ceramics, cloth, oil paint, plastic, sandpaper, stone, Teflon and wood. It turns out that only bamboo, cloth, ceramics, plastic and sandpaper show significantly different reflectance behaviour when immersed in different media, Fig. 3.6. The other materials did not show significantly different reflectance behaviour for different refractive indices; e.g. aluminium is one of the materials that does not show significantly different reflectance behaviour. Its reflectances for surrounding

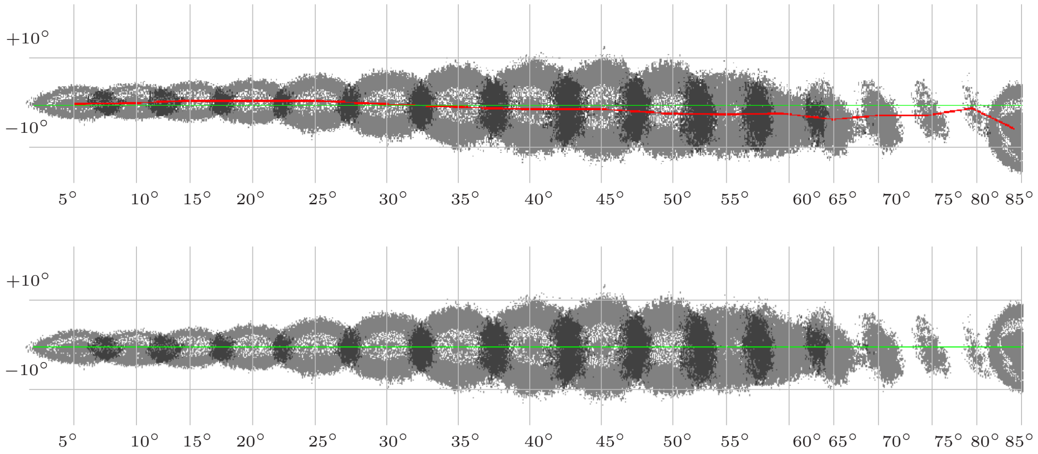

Figure 3.10: The geometric mean of the 95%-percentile for the red plastic measurements varies slightly (upper collage, red line) in position because of small vibrations of the laser holder introduced by the rotation stage (local) after angular motion or small surface normal deviations (global). The effects have to be accounted for by circularly shifting the texture map of the cylinder to have the mean coincide with the (green) meridian line (lower collage).

refractive indices $n_i = 1.0$ and $n_i = 1.44$ vary only in a small numeric range. An exemplary fit for plastic is shown in Fig. 3.11. The decreasing intensity and lobe width for increasing refractive index of the surrounding medium is accurately approximated by the proposed model. For incident angles of high elevation w.r.t. the surface normal, the model tends to overestimate the reflectance values. The other materials did not show different reflectance behaviour for different refractive indices. Table 3.2 shows the results for the fitting of the proposed model to the captured BRDF data of material that show a reflectance behaviour which is governed by the Fresnel term. It lists the model parameters for diffusivity ρ_d, and specularity ρ_s, the estimated refractive index of the material n_t, the surface roughness/exponent of the distribution exp, and the number of iterations k needed for convergence. Note that n_i remains an input variable to the BRDF model.

3.10.5 Renderings

For each material and each surrounding medium the captured reflectance values were saved in MERL-file format [97] after preprocessing using the provided interface. The proposed BRDF model has been implemented in PBRT [112] to enable rendering of immersed materials using artificial refractive indices different from the refractive indices

Material	Subclass	ρ_d	ρ_s	n_t	exp	k
Bamboo	Porous	0.164	0.399	1.292	20.061	48
Cloth	Multiple Layer	0.871	2.782	1.356	9.849	9
Plastic	Single layer	1.5853	0.407	1.323	29.536	8
Sandpaper	Porous	0.200	6.851	0.596	4.732	19
Ceramics	Multiple Layer	0.558	4.269	1.300	20.276	49

Table 3.2: The fitting results for the proposed model with different materials that show the reflectance behaviour governed by the Fresnel term. The table lists the model parameters ρ_d, ρ_s, the estimated refractive index of the material n_t, the exponent for the microfacet distribution, and the number of iterations k needed for the fitting process to converge. Note that the refractive index of the surrounding medium n_i remains variable.

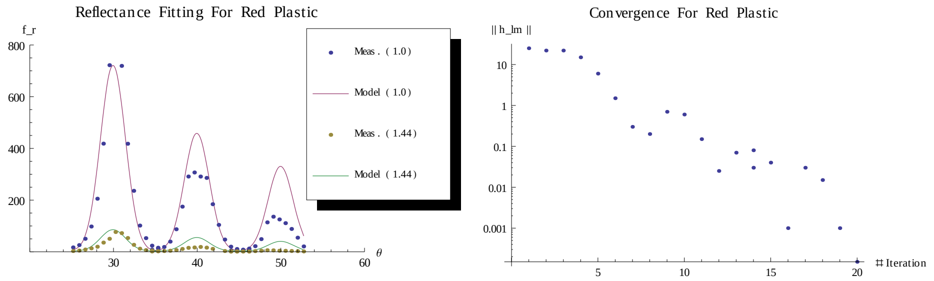

Figure 3.11: The fitting results (left) for the proposed model with red plastic are plotted for three different incident angles (30°, 40°, 50° elevation w.r.t. the surface normal) and two different sourrounding media ($n_i = 1.0$, $n_i = 1.44$). Dots indicate the measured reflectance values, continuous lines indicate the modeled reflectance. The fitting usually converges after 20 iterations (right, convergence criterion c.f. [87]). For incident angles of high elevation w.r.t. the surface normal, the model overestimates the reflectance of the material.

in the set of captured surrounding media. The reflectance function, e.g. of a synthetic plastic material, would then read as

```
BSDF *PlasticMaterial::GetBSDF(...) const {   ...
   float ind = index->Evaluate(dgs);
   float nmat = nMat->Evaluate(dgs);...
   Fresnel *fresnel = BSDF_ALLOC(...)(ind,
nmat); //Assign refractive index parameters for Fresnel behaviour
   if(ind > 1.0){
    BxDF *spec = BSDF_ALLOC(arena, Microfacet)
                  (ks, fresnel, BSDF_ALLOC(arena,
TSDerivDistribution)( rhod, rhos,  e, ind)); ...}
```

```
   else{...}
   return bsdf;
}
```

The constructor would be called with

```
PlasticMaterial *CreatePlasticMaterial(...) {...
   Reference<Texture<float> > index = mp.GetFloatTexture("index", 1.f);
   Reference<Texture<float> > nMat = mp.GetFloatTexture("nMat", 1.f);
   return new PlasticMaterial(...,index,nMat);
}
```

where `index` and `nMat` are passed as parameters from the `.pbrt`-file. To render the results either the measured BRDF data is loaded in the MERL-file format [97] or a material behaviour is synthesised from the fitted parameters. The scenes are assembled using Real Flow fluid simulation [119]. The parts of the object that have fluid spilled on them are assigned the BRDF of the material with a salt solution as surrounding medium ($n_i = 1.44$), while the remaining parts are assigned the BRDF of the material with surrounding medium of air. A glass material assignment to the fluid surface ($n_i = 1.44$, specular reflectance 10%, transmittance 100%) ensured visibility of the fluid-covered surface parts. The light-water interaction was computed using a photon-mapping integrator. The rendering time took approximately ten minutes per frame on a Intel®Core™2 Quad CPU at 2.66GHz; the image resolution was 683×512 pixel. In a second step the BRDFs of air and salt solutions were synthesised with the proposed BRDF model; the parameters were determined by fitting the model to the measured BRDF data, Fig. 3.12.

3.10.6 Limitations

Due to the constraints of the manufactured setup, only the inclination/elevation angle can be sampled for incident light directions. A spatially-varying BRDF measurement in the setup would be reduced to one dimension, the cylinder's main axis, which is intersecting the patch. The measurement of surrounding media with $n_i > 1.7$ poses difficulties, e.g. in terms of the viscosity or stability of the surrounding medium. The quality of the measurements itself is limited by the amount of speckles and the sensor noise of the CCD-chip.

The system of equations in the fitting procedure is overdetermined and numerical inaccuracies in the order of 10^{-16} may alter the fitting results.

Figure 3.12: The captured reflectances for different refractive indices can be used in rendering immersion scenes. Here, the object has a fluid spilled on it (left, top view generated with [119]). The object is split into two separately textured meshes. The part of the object that interacts with water is assigned the material BRDF for red plastic in a salt solution with refractive index $n_i = 1.44$. The other region is assigned the material BRDF for red plastic in air ($n_i = 1.0$). Subtle differences are visible in the reflectance behaviour for the immersed part of the mesh (middle). A rendering without fluid mesh reveals the differences in reflectance behaviour (right).

3.11 Discussion

A new measurement device was presented to measure the reflectance behaviour of different materials which are immersed into transparent media of varying refractive index by placing it at the centre of a cylinder and imaging the reflected laser light with a screen attached to the cylinder. The design choice to sample only the elevation angle was due to the fact that the patch has to be placed within a flawless, completely filled glass half-dome. Visually, plastic showed the most prominent behaviour with a continuous decrease in extent and intensity of the reflected light lobe for an increasing refractive index of the surrounding medium. This measured behaviour supported the conjection that the Fresnel term does govern the reflectance behaviour. Some materials, e.g. cloth, showed a less obvious but measurable behaviour.

3.11.1 Integration into the predictive rendering pipeline

Underwater-BRDFs model the reflectance behaviours of immersed surface patches and are thus integrated as a modeling tool in the predictive rendering pipeline. The above-mentioned procedure provides a tool to retreive reflectance data for immersed materials, if only for varying elevation angles. An existing physically-plausible model from the predictive rendering pipeline is adjusted to account for observed variations in the reflectance behaviour with varying refractive index of the surrounding medium.

4

Light-volume interaction: Measuring the boundaries of two-phase gas flows

4.1 Introduction

Classically, fluid flows have been measured using flow meters, piston meters, venture or dall meters. If the heat conduction properties of the fluid are known to be constant over time, then thermal mass flow meters can be used for measurement as well. At the cutting edge today, two main research fields can be spotted: the detail-driven turbulence analysis conducted in fluid mechanics is one. In the turbulence analysis field, large experimental setups are designed that feature the insertion of small, potentially colored [54, 133] seeding particles of neutral buoyancy [54, 79, 100, 123, 133] whose motion is measured with CCD-cameras. Another measurement method is sensitive Laser-Doppler Anemometry (LDA) based on the fluid's scattering properties and the well-known Doppler shift based on the patent by Edward Roy Pike in 1975 [114]. A good overview about different particle imaging velocimetry setups can be found in the monograph by Adrian and Westerweel [1]. The liability associated with this field is that the observer has to interfere with the flow by inserting particles and introducing disturbances, e.g. small turbulences, in the flow. Note that Laser-Doppler Velocimetry relies on assumptions about the scattering properties of the fluid as well. That means that transparent flows usually have to be seeded with particles [68, 137]. Typical materials are polystyrene, aluminium flakes, hollow glass spheres, oils or oxygen bubbles. On the other hand, there exists the simplicity-driven tomographic reconstruction conducted in computer graphics. The focus lies on capturing simple flows that can also be easily acquired with Laser-Doppler or Particle imaging velocimetry (PIV)/Particle tracking velocimetry (PTV), but only with the use of consumer-grade hardware, and providing the possibility to create digital content modeling gas flows ”at home,” or, at least, in affordable working environments. This field has its roots in Schlieren [98] and interferometric imaging [88]. The background oriented Schlieren imaging technique was registered for a patent in 1999 by G.A. Meier [99]. The limitation of this technique is that constraints have to be imposed on the flow: it should not be obstructed by obstacles. The detection of objects within gas flows in front of background patterns can become a difficult task. A background subtraction approach is not feasible due to small pixel displacements that are introduced by the gas flow [4]. In the following, the interface between two phase gas flows is to be measured in a non-invasive setup comprising consumer grade RGB-D sensors, in this case the Microsoft Kinect. Note that this measurement does not include the spatially resolved velocimetric measurement of the gas flow. Part of this chapter has been published at the *16th International Workshop on Vision, Modeling, Visualization 2011* [15] and the workshop *CDC4CV* in conjunction with *ICCV 2011* [14].

4.2 Related work

Capturing turbulent flows or flows in general is the subject of longstanding research. Kasai *et al.* [77] image the blood flow in organs by employing cross correlation techniques to laser doppler echoes at different time instants. Another approach by Prasad and Sreenivasan [116] produces scalar fields of turbulent flows exiting a jet nozzle by employing energy minimization to the pixel intensity of captured fluorescent fluid in water. The fluorescence is induced by a laser. A rather new approach on the basis of Magnetic Resonance Imaging (MRI) to capture wakes and turbulences was introduced by Newling *et al.* [104]. All methods can either be categorised as invasive, using seeding particles, or non-invasive, relying on laser-Doppler-effects or elaborated pattern analysis.

4.2.1 Invasive techniques

A prominent invasive approach is PIV: it relies on seeding particles into the flow under examination. The extension to tracing flowing particles in consecutive images is called PTV. A method to apply PTV to a turbulent flow in 3D has been presented by Doh *et al.* [40]. Still, given only the images of two adjacent time frames, estimating the

	Elaborated setup	Commodity hardware	Occluders	Unconstrained illumination	Subpixel accurate
Evaluated setup	-	✓	✓	✓	✓
Atcheson *et al.* [6]	✓	✓	-	-	✓
Gregson *et al.* [55]	✓	✓	-	-	✓
Bendicks *et al.* [10]	✓	✓	✓	-	-
Czarske *et al.* [29]	✓	-	-	-	-
Wetzstein *et al.* [145]	✓	-	-	✓	-

Table 4.1: Comparison of related work: while PIV and LDA require elaborated setups, that may feature occluders, the setup proposed by Atcheson *et al.* [6] consists of consumer-grade camcorders and exploits the non-invasive background-oriented Schlieren technique. Note that several parts of the pipeline have to be altered for incorporating occluders [4]. An interesting approach by Wetzstein *et al.* [145] uses light fields that encodes incident angles by colour. Gregson *et al.* [55] measure bouyancy-driven two-phase fluid interactions. They use consumer-grade cameras, but they have to rely on fluorescence effects in one of the two fluids for their image formation model. Both approaches do not evaluate refractive media under the presence of occluders. The evaluated approach incorporates occluders and reconstructs the flow interface at subpixel accuracy relying on Schlieren effects introduced on the actively emitted light pattern.

correlation of a multitude of particle points is an ill-posed problem. Bordas *et al.* [17] proposed to use differently colored particles to ease the matching.

4.2.2 Non-invasive techniques

Voigt *et al.* [135] present a technique to use the laser-doppler effect for imaging the velocity components of a flow on the basis of 2D images. Another approach is based on the flow-based light path alteration of elaborated background patterns that result in different projection images. Atcheson *et al.* [6] proposed a method to capture the time-resolved motion of turbulent gas flows exploiting the Background oriented Schlieren (BOS)-technique. It has to be noted, that they had to carefully engineer a robust background pattern and used a widely-spaced setup where the capturing quality depended on the amount of indirect illumination.

4.2.3 Consumer-grade structured light consoles

During recent years, the use of structured light devices like the Microsoft Kinect, which is used in the evaluated setup, in the consumer sector has experienced a steep increase.

Several popular devices have been employed in the living room environment, for example the Nintendo Wii Remote [75], the input device of the Nintendo Wii gaming console. Besides its own accelerometer, it is equipped with an IR-camera for detecting IR-light sources. The video IR-stream is employed to triangulate the position of the Wii Remote in relation to the TV screen. For this mode a row of infrared Light emitting diode (LED)s is placed atop or under the television. The light sources are detected by the Wii remote and the position is triangulated. The add-on Wii MotionPlus improves the accuracy of the tracking and positioning.

The PlayStation Eye [25] is the camera device of Sony's Play Station 3. It is used for augmented reality applications. This system is a passive light sensor, but it is accompanied by the Sony PlayStation Move, which is a controller with a glowing orb at the top. The glowing orb is tracked by the camera in all three spatial dimensions via its position in the camera image and its size. The orb contains an RGB-LED for illumination. The system is capable of tracking multiple motions by assigning different colors to each controller. The choice of a colour is determined by the maximal distance to each currently assigned colour in the scene.

The equivalent to the Kinect is the Xtion PRO (and the Xtion PRO LIVE) [5]. Both the Xtion PRO and the Xtion PRO LIVE are capable of streaming Video Graphics Array (VGA) depth images at 30fps and Quarter VGA (QVGA) quality at 60fps.

4.2.4 Multiple Kinect setups

As the Kinect is a combined passive RGB and an active structured IR-light sensor, simultaneous calibration presents the same challenges as previous fusion approaches, as described e.g. by Gudmundsson *et al.* [57] or Huhle *et al.* [69]. They both used a fixed rig while the proposed setup employs a static but otherwise freely configurable setup. On the internet, several interesting approaches have been proposed to put the Kinect into a multi-camera setup, ranging from finding texture differences in the IR image with an occluded emitter [44] to treating the checkerboard printout as a planar surface [18]. Another approach involves 3D-structured objects, where their relief encodes a pattern to provide varying depth values in the depth stream [50]. It has to be noted that these approaches have not been proven in setups with multiple Kinects.

Recently, Wetzstein *et al.* [145] showed in their work that it is possible to get dSLR-captured Schlieren images without the need for an image processing pipeline. Their approach encodes angular directions and positions as a colour gamut printout, printed at a resolution of 1200 dpi, in a lenslet array, e.g. *MicroLens Animation10* [101] or *FresnelTech Hexagonal 300* [49], which is placed behind the refractive volume of interest. Fiducidal markers help to align the image plane to the lenslet array. A photo taken with a dSLR, assumed to be a pinhole camera (i.e., the camera has to have a small aperture) then reveals the light path deviations as colour gradients in the projected areas of the volume. Its advantage is that the lenslet array can be placed closely behind the refractive volume and does not necessarily need to be well-lit. The resulting image is comparable to a rainbow Schlieren image [67]. The authors also explore different colour filters in the coded light field, such that an intensity gradient simulates a knife-edge setup at the expense of half the intensity resolution (middle gray would encode zero deflection), or the annular bright or dark fields are sought to simulate effects known to microscopy.

It must be stated that the lenslet array, which covers a comparatively small resolution (bound by the size of the lenses), has to be manufactured and does not qualify as consumer-grade. Both, the profile of the printer colour gamut and the camera colour gamut have to be known beforehand. Their technique itself, while qualitatively visualizing deflections, i.e., the gradient of the underlying refractive volume, does not reconstruct the volume itself. A Poisson integration would have to be computed to get the 3D index field. Furthermore, the technique has to assume a pinhole camera model or incorporate a knife-edge to overcome pixel mapping ambiguities. The lenslet array has to be colour-calibrated after image plane alignment to map colour values to angular directions. The colour-calibration assumes that no refractive volume is placed between the camera and the lenslet array, thus both the lenslet array and the camera have to remain still for at least a small period of time. Nonetheless, the small resolution can be overcome by employing holograms as encoders for position and direction instead of lenslet arrays. Furthermore, the refractive volumes have to be enclosed by the viewing frustum of the camera. Although it has not been stated explicitly that the approach would be capable of discriminating the refractive volume from an occluding object, the resolution at the boundary area would be comparatively low.

Another approach, recently published by Gregson *et al.* [55], introduces the concept of stochastic tomography to reconstruct the buoyancy-driven two-phase mixing process of fluids. They use a consumer-grade camera setup and pour flourescin-sodium dye into water. Their main focus is on the reconstruction, as the raw image stream already reveals the projected extent of each medium. The stochastic tomography approach does not immediately discretize the integral of attenuations/emissions, but computes an observational error compared to an arbitrary starting volume, ideally the volume reconstructed in the last step. The error values are subjected to a convex function with an input set of discrete samples whose density estimation is optimized. A mutation

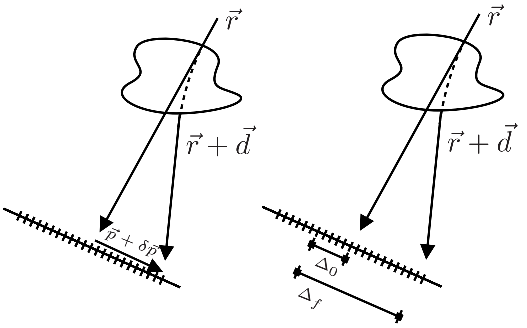

Figure 4.1: A scene that contains a two-phase gas flow introduces measurable light path deviations $\vec{r}+\vec{d}$ on the main axis of the projected cone. This results in a pixel displacement $\vec{p} \pm \delta\vec{p}$ in the IR stream of the structured light sensor (left). In the precomputed depth-image, the same light path deviation would result in a disparity $\Delta_f > \Delta_0$ (right). The first result is measurable with an optical flow approach, the second result is measurable with a difference image approach.

strategy ensures that the position of the samples are determined probabilistically. The offset to the last sample position is gained by adding a Gaussian-distributed random value. Their approach also evaluates the visual hull, but it is used as a boundary for the mutation strategy. Each estimated position outside the visual hull is rejected and recalculated. For the regularisation step, a volume-based and an image-based approach are evaluated.

The drawback of this approach is that it needs dedicated illumination, a LED-strobe ensures a well-lit scene and acts as a synchroniser for the uncalibrated video footage. The reradiation properties of the dye have to be known beforehand to get a good model for the integral of attenuation/emission. Also, the images have to be radiometrically calibrated to the head light source. Their approach has been tested to work with a minimum of five consumer-grade cameras.

4.3 Image formation

Atcheson *et al.* [6] reasoned that a gas flow with a significantly different refractive index than the surrounding air introduces small deviations to a traversing ray $\vec{r}$ that does not enter or leave the interface orthogonally. This also holds for inhomogenuous flows, where the isosurfaces of the refractive index fields denote the interface. The light path deviation can be physically expressed by the Eikonal equation as shown in Sect. 1.2.2. This fact is used in Schlieren imaging by providing a well-illuminated, high-frequency background pattern, which when imaged reveals small ray path alterations.

In the evaluated setup, the Kinects emit an IR-pattern that traverses the interface at least once. The resulting image reveals the introduced light path deviations as follows: consider a projected bright spot of the pre-defined IR-pattern, whose projected pixel position in the IR-sensor would be $\vec{p} + \delta\vec{p}$ when reflected from an object surface at distance d. Now the spot corresponds to a cone with main axis $\vec{r}$ that is emitted from the IR-laser, reradiated from the diffuse surface, and that traverses the gas-flow interface, so that a light path deviation $\delta\vec{r}$ is introduced. Two cases can occur:

1. The main axis path is not altered when traversing the interface. This is true for a negligible index gradient between the two gases or for small cones that travel orthogonally through the interface.
2. The main axis of the cone is bent by $\vec{d}$.

In case 1, the projected pixel movement $\delta\vec{p}$ in the IR-image would be zero. In case 2, the projected pixel movement $\delta\vec{p}$ would be non-negative, possibly smaller than the size of a pixel, Fig. 4.1. This results in a shift of the intensity distribution slightly to the left or right. It is sought to detect the case 2 and robustly discriminate it from random sensor noise resulting in negligible spot movements in the image. This case then determines the projected area of the gas in the sensor images.

In the depth image stream the two cases have the following effects.

For case one, the captured IR-spot would not be shifted closer to or further away from a neighbouring spot, thus the comparison to the reference pattern yields a disparity Δ_0 that equals the disparity Δ in a scene without gas flow. Case two is dependent on the incident angle of the light rays at the boundary layer between the gas and the air. The spot would be shifted closer to or farther away from a neighbouring spot. If it is shifted closer to a neighbouring spot, the comparison to the reference pattern would yield a disparity $\Delta_c < \Delta$, equaling a virtual plane at a closer distance. If it is shifted farther away from the neighbouring spot, the comparison to the reference pattern yields a disparity $\Delta_f > \Delta$, equaling a virtual plane at a farther distance. This fact can be exploited both in the IR-image and the depth image stream for gas flow capturing: either by searching for exactly the depth image deviations Δ_c and Δ_f in a depth image captured from a still scene with the gas flow being the only dynamic scene element, or by evaluating the subpixel spot deviations δp in the IR-image stream. Note that Δ_c and Δ_f are not necessarily distinguishable for evaluating the projected area of the gas flow, since both situations indicate the presence of a light path alteration at the corresponding pixel. The deviations are evaluated above the projected gas nozzle, not at the shadow it casts, which is also present in the depth and IR-image stream.

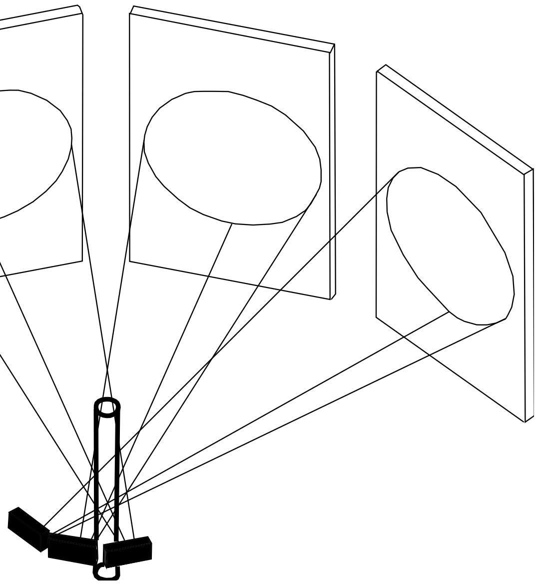

Figure 4.2: In this setup, the volumetric extent of a two-phase gas flow is reconstructed (i.e.,, the volume comprised by the gas (thick cylinder) within a cube filled with air) by capturing it from three discrete viewpoints spaced 30° apart with RGB-D sensors (black boxes). The gas induces light path deviations to the emitted light patterns (cones), that are used to localise the projected position of the gas in the sensor images and to backproject them onto a voxel grid. Occluders may also be introduced to disturb the gas flow. Its implementation includes the use of projection walls,the gas flow is controlled by a valve.

4.4 Setup

The data capture was done outdoors in the shade, in an area measuring 3.5m × 3.5m. The source of the gas flow, a high pressure propane gas nozzle (pressure $\approx$ 400kPa, refractive index $n_i = 1.3407$), was placed below the intersection of the Kinects' viewing axes, which were placed in a small quarter-arc around it, Fig. 4.2. The coded light pattern, which is reflected from the opposite walls, gets distorted by the gas before being imaged by the IR-camera of the Kinect. This is due to the refractive index gradient at the interface of the two-phase gas flow. To minimize pattern distortion due to scene geometry, the three projection walls are orthogonally aligned opposite each Kinect.

The alignment is performed by evaluating the depth image-stream of the Kinect in real-time at the image centre and the four corners of a surrounding rectangle that is likely to comprise the projected area of a captured wall. From all five values, the largest difference is evaluated and a direction to correct the difference is estimated.

Figure 4.3: A checkerboard is usually a printout of a pattern, scaled to suitable size. The pattern is either b/w (left) or colour-coded (M-array, middle) [126, 151]. In the evaluated setup a checkerboard consisting of two materials was employed: mirroring foil and paper sheets (right).

4.4.1 Calibration

In this scenario, several active-light sensors combined with standard RGB-cameras are employed for capturing. As the captured data is to be used for reconstruction, the extrinsic parameters of the sensor have to be calibrated to a common world-space. Ideally, the calibration pattern should be recorded only at one time instant to ensure that the pattern did not move in between two captured calibration images. While this constraint can be accounted for easily in a homogeneous RGB-sensor setup, e.g. with a checkerboard printout attached to a solid planar surface, Fig. 4.3, it becomes more difficult in heterogeneous setups consisting of structured light sensors. The problem is that the printed pattern is not visible in depth- or IR-images, as it is modulated with the structured light pattern. The depth image of a checkerboard printout attached to a solid planar surface would simply show an intensity gradient; the information about the corner locations on the printout is lost. In the non-academic literature, several approaches have been proposed since the release of the Microsoft Kinect [48]. While one approach proposes to use 3D-cuboids (i.e., depth value modulation through non-planar surfaces), another approach proposes to use a printout on a transparent sheet. The unprinted regions on the sheet would not block the light and would thus provide significantly different depth values compared to the printed regions. Both approaches generate problems. The first approach assumes that the infrared light is not blocked by the sheet, which is strongly dependent on the material. The second approach trades pattern visibility in the RGB-sensor for increased contrast in the depth sensor. Thus, a more suitable approach has to be engineered.

It has been stated in chapter 1.2.1 that surface reflectance can be characterized as a probability distribution function with variance values between those of diffuse and

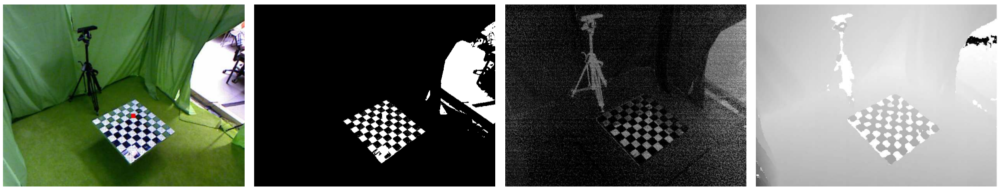

Figure 4.4: In order to calibrate both active and passive sensors at a time, the mirror-diffuse checkerboard can be employed. Consider the RGB-sensor image (far left). After thresholding (left), it can be used for corner detection and consequently for calibration tasks. The same holds for the infrared (right) and depth image (far right) of the structured light sensor after thresholding.

mirroring materials. Following that statement, the diffuse and the mirroring BRDF can be characterized as opposite ends of the scale in terms of reflectance. If a textured surface was to be designed consisting of two materials with maximum difference in reflectance, it would consequently consist of diffuse and mirror patches.

Logically, such a textured surface would provide best contrast in the depth sensor. The advantage is that the same holds for the IR-sensor: each diffuse sheet will provide a single radiance value L_d within a tolerance range accounting for shade and strong illumination. The mirroring sheets map the environment and thus on average provide radiance values $L_{m_{w \in \Omega}} \neq L_d$. For example, bright white paper would be discriminated from a reflected medium green background, e.g. from a green-screen studio, even after a conversion to gray level image. A simple threshold against L_d yields the desired contrast and provides the corners necessary for finding the extrinsic parameters, Fig. 4.4.

4.5 Measurement

4.5.1 Occluders

The gas flow around objects with distinct aerodynamic properties was measured. A bridge (with a drag coefficient $c_d > 1.0$, approximates the turbulence introduced by a skier or a ski jumper), cylinder, box (both $c_d = 0.82$, approximates the turbulence introduced by a coffee filter), cube ($c_d = 0.80$, approximates the turbulence introduced by a model rocket), prism ($c_d = 0.50$, approximates the turbulence introduced by a bicycle), half sphere ($c_d = 0.42$, approximates the turbulence introduced by a rough ball), golf ball ($c_d = 0.3$, approximates the turbulence introduced by a bullet) and droplet ($c_d = 0.04$, approximates the turbulence introduced by the pac-car [152]), were placed in the gas stream, Fig. 4.5.

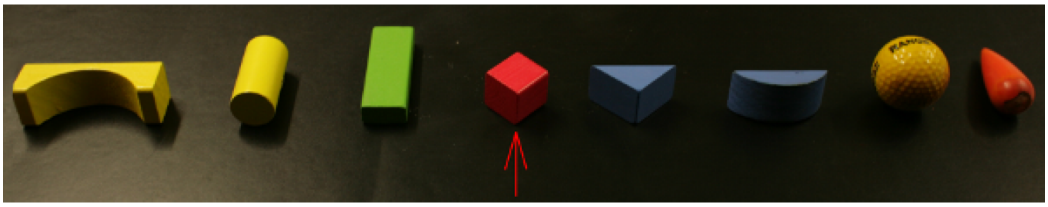

Figure 4.5: Several geometric objects with different aerodynamic properties were examined: a bridge ($c_d > 1.0$), a cylinder ($c_d = 0.82$), a box ($c_d = 0.82$), a cube ($c_d = 0.80$), a prism ($c_d = 0.50$), a half sphere ($c_d = 0.42$), a golf ball ($c_d = 0.3$) and a droplet ($c_d = 0.04$). The objects are shown in the same way as they were placed into the gas flow (indicated by red arrow in the middle).

4.5.2 Evaluation approaches

The Kinect depth sensor can be read out by using the *libfreenect* API, which allows to query the RGB and depth image,or the IR and depth image or the high resolution IR-image (1280×1024) at the same time instant. This enables two different evaluation methods. The first method evaluates the depth images for depth value differences over time. A reasonably different refractive index of the flowing gas would cause alterations to the disparity between two neighbouring IR-spots of the projected pattern and thus lead to minor changes in the depth value at projected areas of the gas volume. The second method evaluates the IR-image itself and searches for any noticeable optical flow in the IR-pattern. It has to be stated that this approach is different to state-of-the-art optical flow methods because it is a sparse method and assumes prior knowledge about image content, i.e., the underlying intensity distribution of an average spot in the projected IR-pattern, Fig. 4.6.

4.6 Depth-based evaluation: polynomial mask fitting

For each Kinect k_i qualitative difference images are obtained by performing a background subtraction of the depth image, i.e., the scene is captured once with no gas flow to get an average image $D_i(0)$. This image is then subtracted for each frame t from a captured image $D_t(t)$ to get the signed difference image $D_{\text{diff},i}(t)$, which may be thresholded to eliminate sensor noise.

$$D_{\text{diff},i}(t) = D_t(t) - D_i(0), i \in 1, 2, 3$$

Then conservative masks are created for the projected areas that are covered by the gas flow by searching for the large connected components $D_{\text{diff},i}(t)$. The projected area

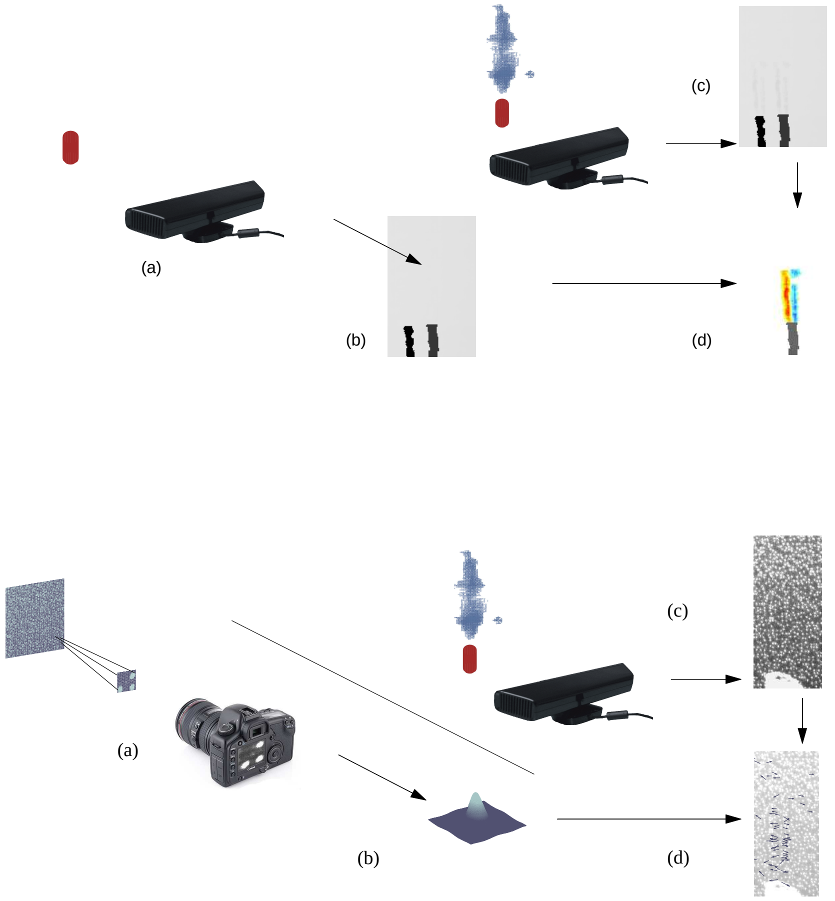

Figure 4.6: In this chapter, two approaches for capturing the gas flow with a commodity RGB-D-sensor are examined. The first approach (upper collage) evaluates depth value alterations from the depth stream. First, the otherwise static scene is captured without flowing gas (a) and a mean depth image is computed as the characteristic scene representation (b). Every subsequent frame in the depth stream with flowing gas (c) is then compared to the mean depth image to get signed difference pixels (d) revealing the projected areas of the gas.
In the second approach (lower collage) the IR-stream is employed instead. The pattern is imaged in high resolution with a dSLR with infrared-blocker removed (a) and a characteristic spot intensity distribution function is computed from the image (b). The pixel movements in every frame of the IR-stream that are introduced by the gas stream (c) can be detected with a sparse spot-based optical flow computation that assumes subpixel shifts to the intensity distribution (d). A threshold of the magnitude then reveals the projected areas of the gas.

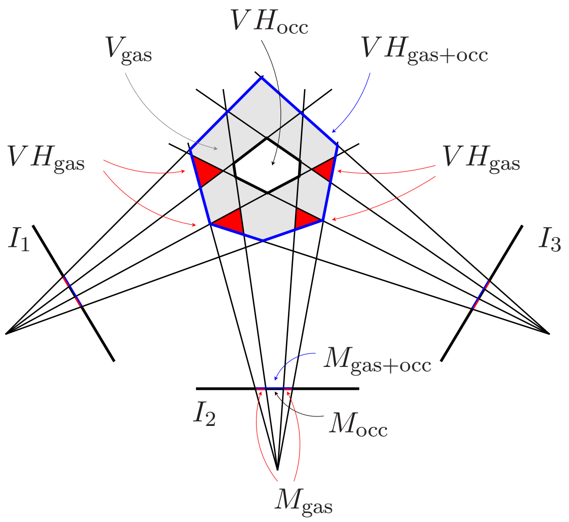

Figure 4.7: The volume of the gas V_{gas} (red and gray regions in horizontal slice) is approximated best by computing VH_{occ} (black boundary, from M_{occ} in each image plane I_1, I_1, I_3) and $VH_{\text{gas+occ}}$ (blue boundary, from $M_{\text{gas+occ}}$ in each image plane) separately and subtracting VH_{occ} from $VH_{\text{gas+occ}}$. If, instead, the masks were subtracted in each image plane a visual hull generation afterwards would result in an incomplete visual of VH_{gas} (from M_{gas} in each image plane) hull (red regions).

corresponding to the occluding object is set to be outside the mask. The object is found by searching for pixels with very small or invalid depth values in $D_t(t)$, and they are marked in $D_{\text{diff},i}(t)$ accordingly.

The hull reconstruction is performed as follows: at first the visual hull $VH_{\text{gas+occ}}$ is reconstructed to represent those voxels that include both the object and the gas followed by the visual hull of only the object VH_{occ}. As in constructive solid geometry [120], VH_{occ} is subtracted from $VH_{\text{gas+occ}}$ to tightly approximate V_{gas}. This way, it is ensured that the reconstructed gas hull fits tightly around the object, Fig. 4.7.

4.7 IR-based evaluation: subpixel-accurate deviation detection

To achieve subpixel-accuracy, a mean intensity distribution kernel is fitted to each laser spot in the IR image. Note that the intensity profile of the laser spot deviates from a standard Gaussian distribution, Fig. 4.8. Usually, an imaged spot spans 3 × 3px in the high resolution image. Subpixel deviations introduced by the gas result in intensity variations that can be accounted for by a slightly shifted distribution. The direction

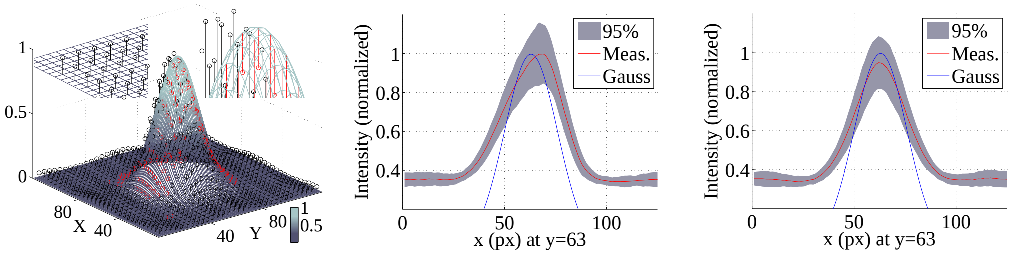

Figure 4.8: The geometry of a measured spot in the projected IR-pattern differs considerably from the profile of a standard Gaussian laser beam (left, black and red error bars and slices, middle and right). In this case a 50mW laser spot is assumed, that is shone onto a planar surface from 3m distance and sampled with a 125 × 125px grid.

and shift then denote the deviation introduced by the gas. A local optimum is found by applying a gradient descent approach

$$x_{n+1} = x_n - \gamma_n \boldsymbol{\nabla} F(x_n), n \geq 0,$$

where x_n spans the domain, in this case the position on the image plane, and F is a multivariate function with defined and differentiable neighborhood. The gray level image is denoted F, and the gradient can be provided e.g. by Matlab's `gradient` function, as a 2D vector. To account for the low sampling rate, the region of interest, usually a 5 × 5px region, is upsampled to a 125 × 125px array. The stepsize γ is set to a small value, usually .5px, but the implementation depends on the IR-stream of the Kinect, which by design has a sparse distribution of spots per image. Thus, the deviation *sampling* is sparse as well.

4.8 Results

The measurement setup has been tested for calibration accuracy, possible interference effects introduced by the use of multiple structured light sensors and for the software evaluation approaches of the image streams.

Finally, some prominent results for gas flowing around occluders are examined.

4.8.1 Accuracy of the calibration pattern

The chessboard calibration method yields an average reprojection error $\mu_{IR_x} = 0.5672$px ($\sigma_{IR_x} = 0.2407$) and $\mu_{IR_y} = 0.3787$px ($\sigma_{IR_x} = 0.0421$) in the IR and an average reprojection error $\mu_{RGB_x} = 0.4870$px ($\sigma_{RGB_x} = 0.3306$) and $\mu_{RGB_y} = 0.3995$px ($\sigma_{RGB_y} = 0.2047$) in the RGB images, with a slight advantage for the RGB camera.

4.8.2 Interference effects

In contrast to motion or opaque scene content capturing setups, the multiple Kinects do not project onto the same surface areas except for the surface of occluder, which is simply masked out. Each Kinect is assigned its own projection wall to project onto and capture from. The gas volume through which all Kinects project does not cause disturbing interference effects or diminish the quality of the depth image or the quality of the captured IR-pattern. It can be shown that the amount of depth pixel errors increases with the amount of specularity of the occluder's surface material, i.e., 10% pixel errors for mirroring foil vs. 2% pixel errors for diffuse carpet with concurrently projecting Kinects. Thus, the occluding objects were chosen to consist of painted wood material, or repainted with a diffuse marker.

4.8.3 Depth-based evaluation

The projection planes could be calibrated so that the distance to its Kinect sensor would result in the same depth. Movable walls were used and fixed to a depth value of 999, which corresponds to 3.04m. The projection planes could be optimized in rotation so that the maximal difference δ_{cc} was ± 1 depth units for a projected area of 200×250 pixels. The circular gas nozzle was placed $\approx$ 2cm below the occluding object, releasing the gas at 400kPa. Throughout the measurement, the depth value changes introduced by the gas flow were in the range $[-2, 2]$. Thus, the evaluation method is rather prone to errors introduced by noise.

4.8.4 IR-based evaluation

The subpixel-accurate, sparse, pattern-based distortion detection against HornSchunck [66], Lucas Kanade [85] and Drulea-Nedevschi [42] with a synthetic spot image and the same image modulated by the *groove2*-flowmap from the Middlebury database [7], Fig. 4.9, have been altered with varying noise and an increasing amount of blurriness. The Average Angular Error (AAE) [8] was compared to the ground truth. The proposed method shows a lower or comparable AAE with increasing image degradation compared to the other flow algorithms, Fig. 4.10. Thus, the proposed algorithm is more robust against the noise introduced by the capturing setup. The occluders have been segmented out by removing the overexposed region in the input image. The projected area of the gas flow could be determined to subpixel accuracy in the input images. A refinement of the visual hulls can be performed in a secondary step.

4.8.5 Obstructed gas flows

In the following subsection, the capture and reconstruction of particular gas flows are evaluated for some prominent occluding objects. The occluders were chosen in order to visualize three different effects introduced to the gas flow: smooth flow, diverged flow, blocking and flow direction reversion.

4.8.5.1 Droplet

As the object with lowest drag coefficient, the droplet occluder introduces almost no turbulences to the flow, Fig. 4.5. The gas stream, obtaining a comparable width as the object, flows smoothly around it, Fig. 4.11. The *quiver* plot, i.e., plot that displays velocity vectors as arrows with components at the corresponding points [93], shows a distinct area, distorted by the exhausting gas. Near the border of the droplet, stronger distortions are recognisable. In the left parts of the *quiver* plots, around the object's shadow, the direction of the distortion vectors is inverted.

4.8.5.2 Golfball

Although the golfball occluder has a low drag coefficient, it is wider than the width of the gas stream. It forces the propane gas to diverge and flow around the object, Fig. 4.12. This is noticeable in the reconstructed 3D hulls as well. The golfball object obstructs the flow, and an alternative flow path to the right is established. Again, strong distortions near the valve are recognisable in the *quiver* plot, and the alternate flow path to the right is detectable in the upper right part of the plot. The inverted distortion vectors are detectable above the shadowgraph of the object. Minor noise in the flow field is detectable approximately at the height of the valve, in neighbouring regions to the left and to the right.

4.8.5.3 Bridge

Being a concave object, the bridge occluder obstructs the flow of the propane almost completely, Fig. 4.13. The flow of the propane gas is not only blocked, its direction is reverted as well. Both the difference and the depth images show distorted regions expanding downwards to the bottom of the image: a red contour line in the difference image plot for the depth image approach indicates the inversion of the gas flow. In the *quiver* plot, the inverted vectors near the projected area of the bridge indicate the existence of gas flow directed downwards. It is notable that minor distortions are visible *above* the bridge occluder which can be explained by small propane volumina passing

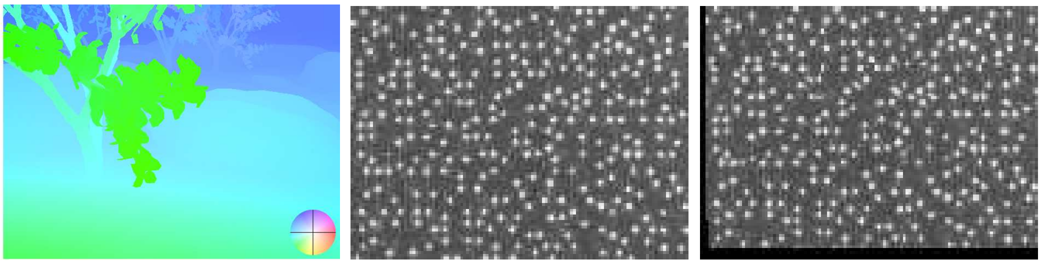

Figure 4.9: The *groove2*-flowmap [7] (left) is applied to a synthetic spot pattern (middle, cropped) resembling the spot pattern of the Kinect to get a reverse-warped image (right, generated with Matlab and cropped) as ground truth data for the optical flow comparison, Fig. 4.10.

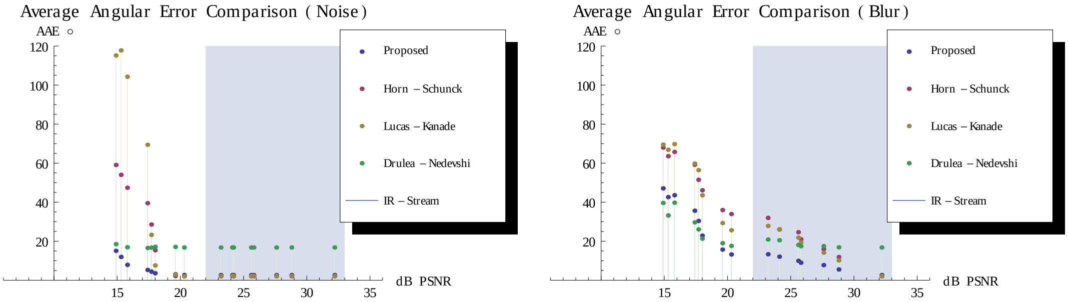

Figure 4.10: The quality of the IR-based approach is evaluated by comparing it to state-of-the-art optical flow methods. As test dataset, the modulated spot pattern is used, Fig. 4.9. An increasing level of noise (left plot, PSNR computed) and of out-of-focus blur (right plot, PSNR computed) is applied to it. The computated optical flow is compared to the ground truth (*groove2*-flowmap), and the average angular error is evaluated. It can be seen that the average angular error for the proposed distortion detection (blue points) is significantly lower than for the Horn- Schunck [66] method (magenta points) and Lucas-Kanade [85] method (yellow points) compared to the recently published Drulea-Nedevschi [42] method (green points) in the relevant range. The range was chosen because the PSNR of an average IR-image from the Kinect sensor ranges from 22dB to 33dB (light blue area).

by the bridge at the front or at the rear. In the reconstructed 3D hulls the obstruction of the flow and the divergence towards the bottom is visible. The distortions above the bridge were deliberately thresholded out for the 3D reconstruction.

4.8.6 Limitations

The setup constrains the measurement devices to span only a half-arc and interference effects may occur, if the object under investigation is comparatively large in size. The

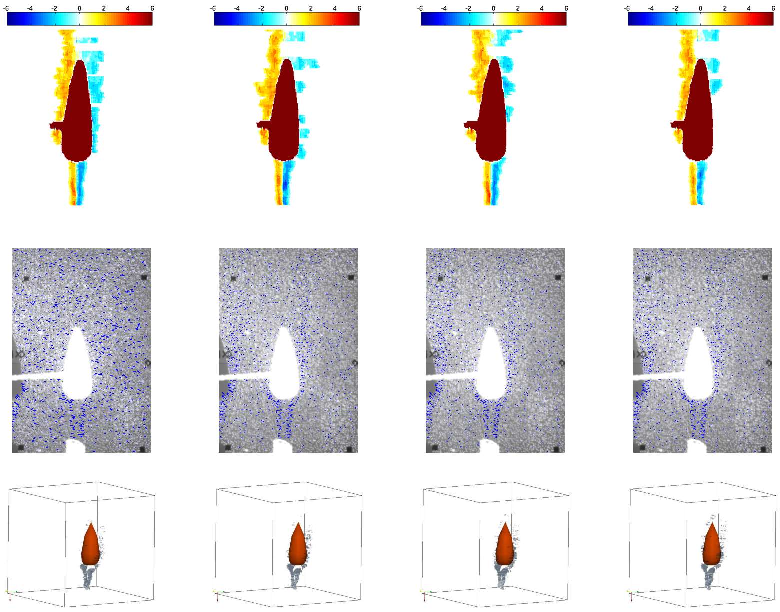

Figure 4.11: Four consecutive frames for the gas flow around the droplet evaluated with the depth-based (top row) and IR-based (second row) method and the reconstructed boundary of the two phases (third row). The colors in the difference plot (first row) indicate the amplitude of depth differences introduced by the gas. For visualisation purposes the *quiver*-plot (second row) is enhanced in length by a factor 2 and thresholded for horizontal vector length $> .2$ to show the subpixel movement introduced by the gas. It can be seen, that the droplet intrudes smoothly in the gas flow without causing major turbulences. The direction of the distortion vectors is inverted around the object's shadow.

image resolution of the depth image, the number of spots in the IR-image and the index gradient introduced by the particular gas limit the quality of the deviation computation. Small air pressure differences are thus hardly recognisable, e.g. a sound wave detection with that setup is not feasible. It is not possible to genlock the Microsoft Kinect, thus the recorded depth- or IR-streams have to be temporally aligned, e.g. by searching for a distinct motion path introduced by the user beforehand in all streams. The amount of data per recording (e.g. in the depth-based approach $640 \times 480 \times 30$fps $\times$ 2 bytes of depth) limited the recording time to a minute, the recordings were streamed to RAM-disk, as the hard drive's access time would introduce unnecessary frame drops. The field of view of the Microsoft Kinect is rather limited (57.8°) compared to state-of-the-art structured light sensors like the Hokuyo laser ($240° - 270°$) [81]. The laser unit of the Microsoft Kinect cannot be deliberately switched on and off in a clock rate by USB commands, and the emitted light is too intense to block it with conventional

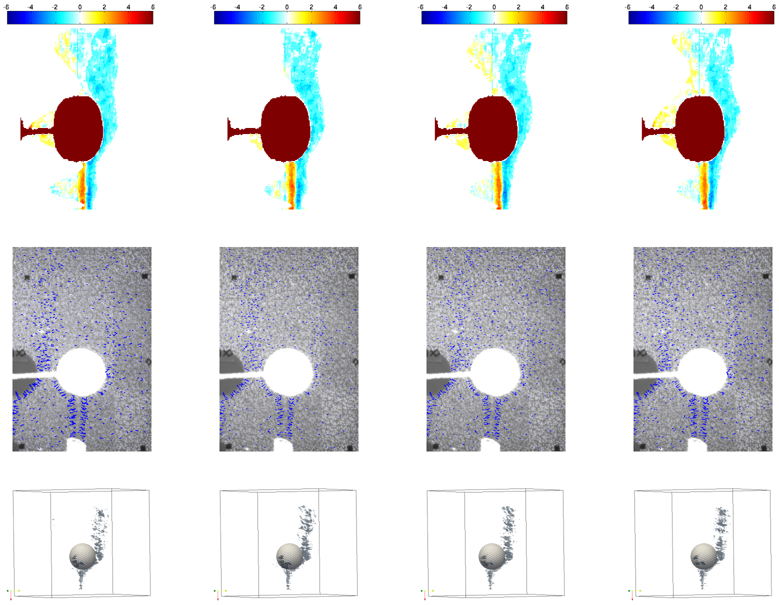

Figure 4.12: Four consecutive frames for the gas flow around the golfball evaluated with the depth-based (top row) and ir-based (second row) method and the reconstructed boundary of the two phases (third row). The colors in the difference plot (first row) indicate the amplitude of depth diffences introduced by the gas. For visualisation purposes the *quiver*-plot (second row) is enhanced in length by a factor 2 and thresholded for horizontal vector length $> .2$ to show the subpixel movement introduced by the gas. It can be seen, that the golfball blocks the gas flow partially and forces it to flow at an alternate path to the right of the object. Minor noise in the flow field is detectable approximately at the height of the valve, in neighbouring regions to the left and to the right.

LED-based devices. Thus, an artificial frame rate posed on a Kinect would have to be realised by blocking the light with additional hardware, e.g. a rotational shutter device.

Another limitation of the setup is the permitted range of the sensor, i.e., the Microsoft Kinect ranges from 0.6m to 5m. Images from below or beyond that range consist of invalid values or are over- or underexposed. This is mainly due to eye-safety regulations recommended for such a gaming device. Attached zoom devices, like the Nyko Zoom [148], may enhance the view. The measurements have to be taken under good lighting conditions, e.g. in the shade with stable skylight. Rain, snow and severe light changes due to cloud movements may alter the images. Both the RGB- and the IR-sensor have a filter attached to the CCD-chip to introduce a Bayer-pattern, thus the pixel values in the IR-values may not have the same accuracy to the measured intensity

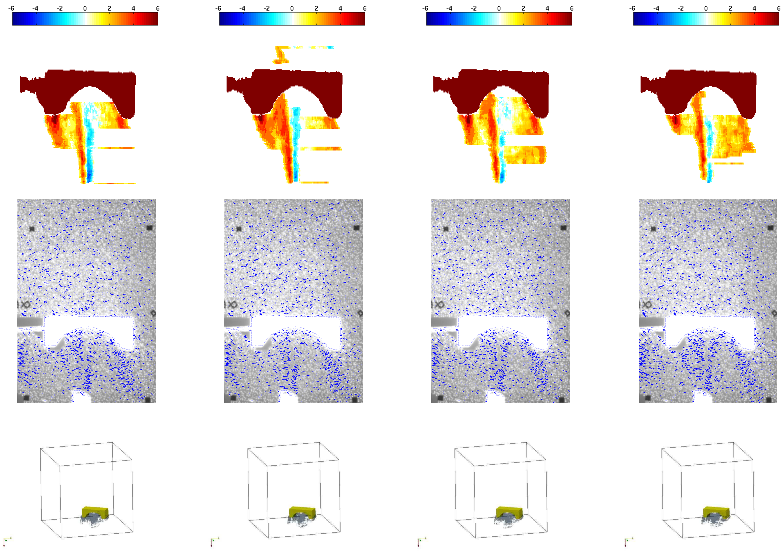

Figure 4.13: Four consecutive frames for the gas flow around the bridge evaluated with the depth-based (top row) and IR-based (second row) method and the reconstructed boundary of the two phases (third row). The colors in the difference plot (first row) indicate the amplitude of depth diffences introduced by the gas. For visualisation purposes the *quiver*-plot (second row) is enhanced in length by a factor 2 and thresholded for horizontal vector length $> .2$ to show the subpixel movement introduced by the gas. It can be seen, that the bridge almost completely blocks the gas flow and forces it to revert the direction. Small volumina parts flow around the bridge to the front or the rear and cause minor deviations. The distortions above the bridge were deliberately thresholded out for the 3D reconstruction.

of a captured IR-spot and would have to be prefiltered for equalization of the subtle intensity differences. A refinement of the visual hull is bounded by the amount of 2D measurements, thus a setup consisting of three Kinects may constrain the visual hull refinement to infer radial symmetry or smoothness of the volume.

The setup itself is limited to capturing boundary surfaces between two phases for a homogenous gas flowing through another homogenous gas. It is assumed in the setup that the propane gas flow remains homogenous after escaping from the nozzle. It is not possible to measure the velocity of the gas flow, i.e., it does not compute spatially resolved vector fields.

4.9 Discussion

The Microsoft Kinect, an active-light based gaming device, was investigated for its capability to capture turbulent gas flows around occluding objects with the purpose of enabling reconstruction of such phenomena with low-cost consumer-grade imaging devices. The investigation is motivated by the fact that in purely passive light image-based approaches to gas capturing, the occluder has to be segmented by image statistics, e.g. histogram comparison or edge detection, while with the structured light sensor Kinect, the occluder can be segmented out by its depth value or its distinct reflection of the IR-image. As the API *libfreenect* allows to retrieve both a densely computed depth map and its underlying high resolution IR-stream of the emitted pattern, it was proposed to evaluate both sensor data, the depth- and IR-images. The notion behind the depth images was that a gas flow with a significantly different refractive index would alter the light path of the diffusely reflected IR-pattern from the scene and thus would lead to desired misinterpretations during disparity estimation, i.e., a virtual plane would be estimated to be closer or farther away than the actually captured plane if an IR-spot were to be shifted towards a neighbouring spot or away from it respectively.

As multiple Kinects were employed around the scene, several questions arose. It was shown that the Kinects do not interfere with each other in a disturbing way, because each sensor was projected onto a different wall. A common projection surface was only the obstructing object. The objects were chosen to have a diffuse surface and were deliberately segmented out, both in the 2D images and the 3D reconstructions. Furthermore, the Kinects could be calibrated simultaneously for the RGB- and IR-camera by introducing a checkerboard consisting of two disjointed BRDFs. This is due to the fact that mirroring materials, placed at right angles (i.e., every angle except nearly orthogonal to the camera's viewing axis), will project the IR-pattern to the surrounding scene. The resulting depth values in the captured images would then either be significantly different from the values of the diffuse surface or be invalid. A segmentation could then be easily performed by thresholding out the diffuse values.

An evaluation of the sensor images showed that the left and right boundary of the projected gas could be identified in each sensor's depth image, but the amplitude of difference values would be comparatively small, and thus it would be more exposed to errors due to sensor or scene noise. Nonetheless, the projection planes could be calibrated to their corresponding Kinect in distance up to the exact depth value. The occluders could be extracted instantly by thresholding for their depth value, usually the smallest depth value in the image.

A similar notion was applied to the IR-image, as the light path deviation would lead to blurry or slightly displaced IR-spots in the captured image. In the IR-approach a sparse, spot-based optical flow algorithm was proposed. The spot was characterized by a kernel, because it differed significantly from a standard Gaussian laser beam profile. The kernel was fitted accurately to a subpixel level by employing a gradient descent approach for the spot positions. As initial value an IR-image captured before the gas flow was used. The occluders were overexposed in the IR-image and thus could be extracted by finding the largest connected component with maximum intensity value in the image. A comparison between both approaches revealed that the IR-image-based method shows a more accurate capturing of the projected gas flow. Both methods and the 3D reconstruction were examined for three occluders that either blocked the gas flow (bridge occluder), caused the flow to diverge (golf ball occluder) or that smoothly intruded in the gas flow (droplet occluder) without causing noticeable turbulences. Some disadvantages of the evaluated setup were detected, e.g. the limited field of view and the restricted capturing range. The USB protocol prohibits a frame rate higher than 30 fps and the use of more than one sensor per bus. A Bayer filter attached to both CCD-chips alters the captured intensities and thus the resulting image would have to be filtered before evaluation. The extent of the captured gas volume was limited.

4.9.1 Integration into the predictive rendering pipeline

The geometric extent of the interface between two-phase flows has been measured and reconstructed on the example of propane flowing in air. In the context of the predictive rendering pipeline, the proposed method can be sorted in as a tool to capture and reconstruct the exact geometry of the scene content, e.g. the participating medium. Although the accuracy of the employed sensor, the Microsoft Kinect is bounded, it is still notable, that the presented setup is the first approach to reconstruct the geometry with sensors in the end consumer segment.

5

Conclusion

This thesis has presented various contributions to the field of light-matter interaction phenomena. At first, a method for capturing the polarisation behaviour of real-world metals is presented. It relies on ellipsometry and fitting the predictive model to the reflectance ratios calculated from the polarisation values. One can obtain new renderings from the measurements that are visually indistinguishable from the predicted reflectances. The measurements showed that anisotropy can be neglected. The outcome of the measurements was dependent on the surface position for coins that have undergone a common mint procedure, the *Polierte Platte*. For anodised aluminium (E6), a validation could not be found. Instead, a layered structure had to be assumed to accurately model reflectance. For aluminium foil, the validation could be performed.

Secondly, a new BRDF has been presented that incorporates the effect that the Fresnel term governs the reflectance behaviour for immersed materials. The refractive index of the surrounding medium is variable and thus adds a dimension to the reflectance function. It has to be stated that the Fresnel effect could only be verified for a subset of materials. Plastic shows the most significant change in reflectance for varying refractive indexes of the surrounding medium. In the example on cloth, minor changes at grazing angles were observed. The processing pipeline involved circular shifts of the reprojected cylinder textures to account for small deviations from the ideal meridian due to slight deviations of the surface normal direction or due to damped oscillations of the rotation stage with attached laser light source during the recording procedure. With the new BRDF, renderings of objects that are partially immersed in transparent surrounding media, e.g. which have had distilled water spilled on them, were generated with a greater degree of photorealism.

Finally, the light-volume interaction in two-phase gas flows was exploited to use consumer-grade RGB-D sensors to capture gas flows around occluding objects. The obstruction of gas flows with objects has been considered an unsolved task to date, because it either required the setup to be more elaborate, e.g. invasive, or it required the image processing algorithms to correctly discriminate between the projected object and the projected area of the gas flow. Applying RGB-D sensors to the problem leads to correct extraction of the occluder. Two evaluation procedures were examined, the evaluation of the depth stream by finding depth value deviations and the evaluation of the IR-stream by searching for optical flow of the IR spots. While both approaches could detect the immanent gas flow, the IR-based approach proved to be more accurate. The method was applied to gas flows around occluders with different aerodynamic properties, and their effect on the gas flow propagation was examined. In the context of a measurement setup consisting of multiple RGB-D-sensors, a calibration method with a checkerboard consisting of two materials was employed. Interference effects were not observed as the RGB-D-sensors would either project onto disjointed surface areas, or the objects obtaining a common surface area would be segmented out beforehand as occluders.

Common to all three contributions in the field of light-matter interaction phenomena was the implementation of an examination setup, the collection of a set of materials with common properties, and the algorithmic evaluation and fitting of models to the recorded data. The resulting evaluation was split into the evaluation of the algorithmic part and the evaluation of the examined effects. All three contributions seek to provide tools for an accurate modeling of the scene in the predictive rendering pipeline, either by verifying physically-plausible BRDF models and by adjusting them for immersion scenarios or by capturing and reconstructing the exact geometry of the interface of a scene content, here the flow of propane gas.

Appendix A

Ordering BRDFs

Throughout the thesis, it was assumed that BRDFs can be ordered, and that in different order schemes the mirror and diffuse BRDF would be sorted to the limit of the particular scale. Several approaches have been proposed in the literature, e.g. the PCA of a measured dataset or the fit of an analytic distribution function, e.g. the von-Mises-Fisher distribution to the arbitrarily defined BRDF. It has to be stated that both approaches remain artificial in terms of the ordering scheme. In the following discussion, it is assumed instead that the statistical representation of the BRDFs is arbitrary, i.e., they can be represented by either a continuous analytical function or a discrete 2D-histogram of integers. Then the ordering itself is to be performed with a statistical measure that applies to both, the discrete and the continuous formulation. The proof shows that the mirror and the diffuse BRDF are sorted to the upper and lower limit of the BRDF order scheme. It has to be noted that for ordering only the prominent lobe is considered, i.e., for an arbitrary incident angle only the range around the maximum reflectance value that has the same monotony is considered. Rough or retroreflective BRDFs are averaged to a mean off-specular value, that is similar to a diffuse term. The FWHM was used to compute an order value for each specular lobe. It is an expression for the width of a distribution function, given by the difference between the two extreme values of the independent variable at which the dependent variable is equal to half of its maximum value. It is used to describe the pulse and the spectral width of sources, e.g. for the resolution of spectrometers. In signal processing, the convention of "width" as "half maximum" is commonly agreed upon. For higher dimensions, the axis projections can be employed for the FWHM separately. The evaluation can now be performed in directional statistics or in linear 2D statistics, Fig. A.1. A directional statistics evaluation appears intuitive, as the probabilities are dependent on angles on a sphere. In that sense the distribution is evaluated over the exitant angle θ of the BRDF. An ideal mirror surface illuminated by an infinitesimal small laser spot at angle θ_i to the surface normal would reflect the light in the mirror direction, and the reflectance would consist of an infinitesimal small spot on the parallel plane. The support in this case would only be at $\theta = \theta_i$, thus the cumulative distribution is

$$\int_{-\pi/2}^{\pi/2} \delta(\theta - \theta_i) \frac{\mathrm{d}\theta}{\pi} = 1. \tag{A.1}$$

In this case, the FWHM evaluates to zero, thus determining the infimum of a BRDF ordering.
A perfect diffuse surface has support over the complete hemisphere, thus every point on the parallel plane has the same non-zero probability of being illuminated.

$$\int_{-\pi/2}^{\pi/2} \frac{\mathrm{d}\theta}{\pi} = 1. \tag{A.2}$$

Note that the FWHM evaluates to 2π, thus determining the supremum of a BRDF ordering. BRDF ordering would have to be constrained to not include values greater than 2π, which is numerically unsatisfying. Besides, a perfect diffuse surface can only be approximated in nature. Ideally, one would like the mirror to evaluate to zero and the perfect diffuse BRDF to evaluate to infinity. Thus, the BRDF evaluation is now performed in linear 2D statistics by assuming an infinite plane parallel to the surface patch at a distance d, Fig. A.2. The evaluation would be performed on the domain spanned by the infinite plane. For simplification the formulae are derived in 1d case, i.e., dependency only on the elevation, but the quantile measurement can be extended to higher dimensions as well [60]. An ordering for BRDFs obtaining one prominent lobe is derived by considering their reflectance as a probability distribution on a second plane parallel to the surface patch at a distance d.
The distribution is evaluated over the exitant angle θ of the BRDF, which can be described as $\theta = tan^{-1}(\frac{y}{d})$ for a point y on the second plane.
Its infinitesimal element $d\theta$ can be derived as

$$\mathrm{d}\theta = \frac{d \cdot \mathrm{d}y}{d^2 + y^2}$$

The cumulative distribution has to evaluate to 1, thus

$$\int_{-\pi/2}^{\pi/2} \frac{\mathrm{d}\theta}{\pi} = 1,$$

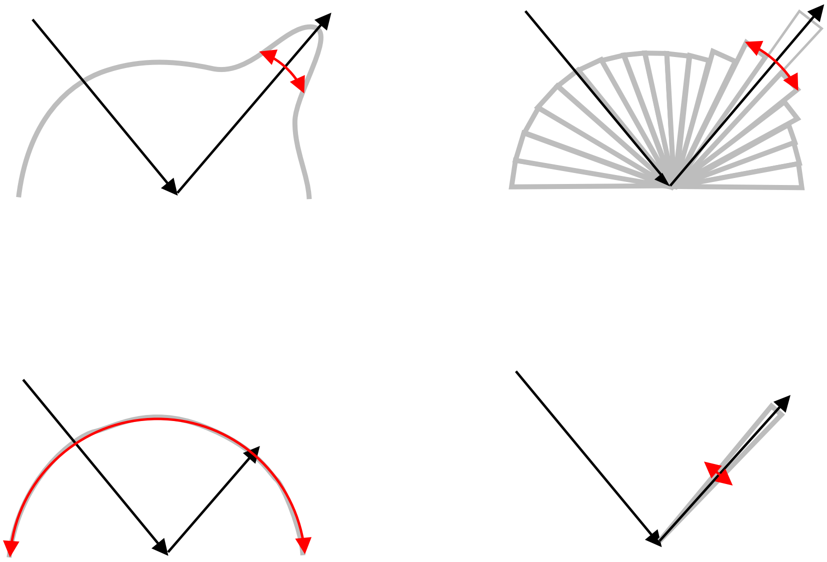

Figure A.1: The FWHM in directional statistics, in evaluating angles on the unit sphere, is shown on the example of a continous Phong BRDF (top left), a discrete reflectance histogram (top right), a continuous, nearly perfect diffuse BRDF (bottom left) and a discrete histogram of a mirror (bottom right). The gray lines or triangles indicate the amount of reflectance for a given angle, while the Length of the red double arrow denotes the value of the FWHM. The evaluation is depicted for the 1d case, for higher dimensions the FWHM would have to be evaluated for each dimension.

with $\frac{1}{\pi}$ as normalizing coefficient.

Finally, the probability for an angular element is given by

$$\frac{\mathrm{d}\theta}{\pi} = \frac{d\ \mathrm{d}y}{\pi d^2 + y^2}.$$

An ideal mirror surface illuminated by an infinitesimal small laser spot at angle θ_i to the surface normal would reflect the light in the mirror direction, and the reflectance would consist of an infinitesimal small spot on the second plane, Fig. A.3.

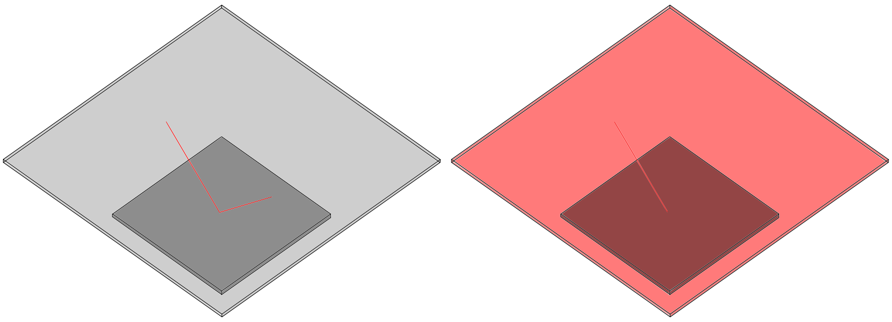

Figure A.2: An arbitrary ordering of BRDFs obtaining one lobe would result in letting the perfect mirror be the infimum, and the ideal diffuse surface be the surpremum. This arbitrary ordering is reasoned by evaluating with the FWHM, a statistic measure applicable to continuous and discrete distributions. While the intuitive measurement in directional statistics would result in an unsatisfying range for the BRDF ordering, the measurement in linear 2D statistics would give the desired result: the BRDFs are sampled over an infinite continuous 2D plane parallel to the surface patch at a distance d. The density function, resembling a skew bivariate Cauchy-distribution, would be evaluated by a FWHM resulting that the FWHM $\rightarrow 0$ for the mirror (indicated by red spot on the plane) and FWHM $\rightarrow \infty$ for the perfect diffuse surface (indicated by red plane), hence proving the ordering.

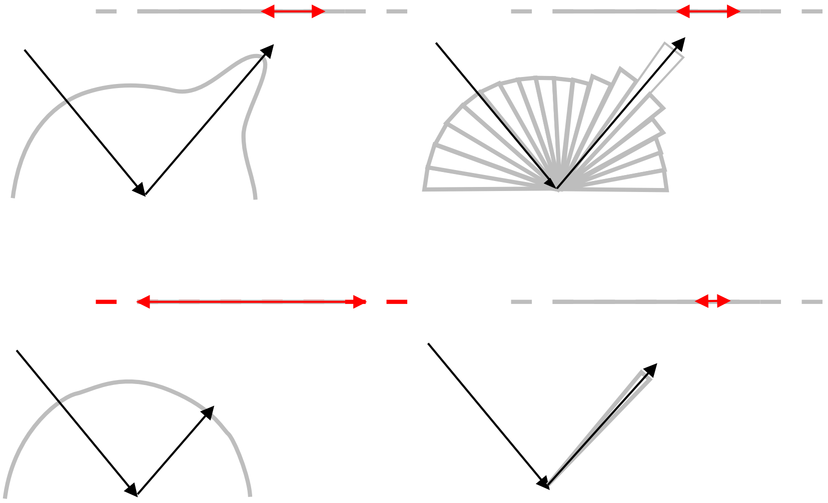

Figure A.3: The FWHM in linear 2D statistics with the help of sampling on a parallel infinite surface (grey line, dashed to indicate infinite extent) is shown on the example of a continuous Phong BRDF (top left), a discrete reflectance histogram (top right), a continuous, nearly perfect diffuse BRDF (bottom left) and a discrete histogram of a mirror (bottom right). The length of the red double arrow denotes the value of the FWHM. The value for the diffuse BRDF expands to infinity (red line, dashed to indicate infinite extent), while the value for the mirror BRDF vanishes (with respect to the sampling width). The evaluation is depicted for the 1d case, for higher dimensions the FWHM would have to be evaluated for each dimension.

The support in this case would only be at $\theta = \theta_i$, thus the cumulative distribution would be

$$\int_{-\pi/2}^{\pi/2} \delta(\theta - \theta_i) \frac{\mathrm{d}\theta}{\pi} = 1.$$

In this case, the FWHM evaluates to zero, thus determining the infimum of a BRDF ordering.
A perfect diffuse surface has support over the complete hemisphere, thus every point on the second plane has probability > 0 of being illuminated.

$$\int_{-\pi/2}^{\pi/2} \frac{\mathrm{d}\theta}{\pi} = 1.$$

Note that the FWHM evaluates to infinity, thus determining the supremum of a BRDF ordering. A generic Phong-type BRDF f_r with a specular term and a diffuse term, that has support over the complete hemisphere would have to be ordered as follows. If the half maximum is smaller than the diffuse term, then FWHM would evaluate to infinity, thus ordering the BRDF to the perfect diffuse BRDF. In order to prevent this, the minimum reflectance value of the BRDF would have to be subtracted from all reflectance values to cancel out the diffuse part. Thus, the glossy lobe would remain and the FWHM would evaluate correctly: We define a BRDF $\hat{f}_r$ as

$$\hat{f}_r = f_r - \min_{\theta_i, \theta_o}(f_r),$$

which would be ordered only by the variance of the area illuminated by the glossy lobe. The same notion applied to the perfect diffuse BRDF would result in shifting the reflectance from a constant value c to zero everywhere, because the minimum and maximum value coincide but the FWHM would evaluate it to infinity. Retroreflective BRDFs or BRDFs that do not show distinctive maximum intensity around the mirroring direction would either have to be averaged to diffusivity or not considered in the BRDF ordering.

Acronyms

AAE	Average Angular Error. 77
BOS	Background oriented Schlieren. 65
BRDF	Bidirectional Reflectance Distribution Function. 10–12, 20–22, 25–27, 29, 32–34, 38, 50–52, 55, 58, 59, 61, 72, 83, 85, 87, 88, 90, 91
BSSRDF	Bidirectional subsurface scattering reflectance distribution function. 20
BTDF	Bi-directional Transmittance Distribution Function. 13, 22
CAD	Computer-aided design. 5
CCD	Charge coupled device. 8, 9, 19, 20, 22, 25, 26, 61, 63, 81, 84
DRC	DARPA robotics challenge. 7
dSLR	digital single-lens reflex camera. 5, 31, 66, 67, 74
EV	Exposure Value. 54
fps	frames per second. 8, 66, 84
FWHM	Full Width at Half Maximum. 12, 87–91
HDR	High Dynamic Range. 42, 54

IR	Infrared range (> 750nm). 35, 36, 66, 69–74, 76, 77, 79–84
ISNP	Institut des NanoSciences de Paris. 29
LDA	Laser-Doppler Anemometry. 63, 65
LED	Light emitting diode. 66, 68
MERL	Mitsubishi Engineering and Research Lab. 25, 61
MRI	Magnetic Resonance Imaging. 64
PBRT	Physically based Rendering Toolkit. 42, 43, 59
PCA	Principal Component Analysis. 21, 87
PIV	Particle imaging velocimetry. 64, 65
PSNR	Peak Signal to Noise Ratio. 79
PTV	Particle tracking velocimetry. 64
QVGA	Quarter VGA. 66
RANSAC	Random Sample Consensus. 54
RGB	Red-green-blue colorspace. 26, 66, 71, 81, 83
RGB-D	RGB and depth map. 22–24, 64, 70, 74, 86
RMS	Root Mean Square. 33
svBRDF	spatially-varying BRDF. 22, 46
tvBRDF	time-varying BRDF. 46
UV	Ultraviolet range (< 390nm). 36, 38
VGA	Video Graphics Array. 66
VIS	Visible range (390 – 750nm). 31, 35–40
XE	Xenon. 31, 35, 36

List of symbols

$D_i(0)$	Average depth image at frame 0. 73
$D_t(t)$	Depth image at frame t. 73, 75
$D_{\text{diff},i}(t)$	Difference image at frame t. 73, 75
D	Microfacet distribution. 32, 33, 42, 50, 55
F_r	Fresnel reflectance. 16, 50
F_t	Fresnel transmission. 16
G	geometric term. 32, 42, 55
I_1	First Kinect sensor's image plane. 75
I_2	Second Kinect sensor's image plane. 75
I_3	Third Kinect sensor's image plane. 75
L_d	Diffusely reflected radiance value. 72
$L_{m_{w\in\Omega}}$	Reflected radiance value, mirrored from environment radiance. 72
L	Radiance, emitted, incident, excitant. 12, 50, 51
$M_{\text{gas+occ}}$	Image mask comprised by the projections of both an occluder and the gas flow. 75
M_{gas}	Image mask comprised by the projections of the gas flow. 75
M_{occ}	Image mask comprised by the projections of an occluder. 75
S	Shadowing term. 50
$VH_{\text{gas+occ}}$	Visual Hull comprised by both an occluder and the gas flow. 75
VH_{gas}	Visual Hull comprised by the gas flow. 75
VH_{occ}	Visual Hull comprised by an occluder. 75
V_{gas}	Volume comprised by the gas flow. 75

Ω	Hemispherical Domain. 11–13
$\boldsymbol{\rho}$	Relative change in field behavior, parallel, perpendicular component. 15, 16, 32, 34
λ	Wavelength. 11, 16, 32, 39–41
$\mathbf{C}$	Babinet-Soleil Compensator in Drude's Ellipsometer. 28
$\mathbf{E}$	Electromagnetic field of incident light wave, parallel, perpendicular component. 14, 15, 17, 26
$\mathbf{F}$	Telescope in Drude's Ellipsometer. 28
$\mathbf{K}$	Telescope in Drude's Ellipsometer. 28
$\mathbf{M}$	Mueller Matrix of optical element, e.g. linear polarizer or retarder. 18
$\mathbf{R}$	Electromagnetic field of reflected light wave, parallel, perpendicular component. 11, 15, 26
$\mathbf{S}$	Stokes Vector. 17
$\mathbf{S}$	Sample in Drude's Ellipsometer. 28
$\boldsymbol{\Delta}$	Relative change in phase. 15, 16, 28, 32, 35–40
$\boldsymbol{\Psi}$	Relative change in amplitude. 15, 16, 18, 28, 32, 35–40
$\mathbf{p}$	Polarizer in Drude's Ellipsometer. 28
E	Error Functional of Levenberg-Marquardt Fitting. 33, 34
J	Gradient of function in Levenberg-Marquardt Fitting. 34
$\mathrm{d}s$	Infinitesimals, arc element, cartesian elements. 13, 14
ϕ	Azimuth angle, incident, excitant. 11–13, 54
ρ_d	diffuse part of refractive index dependent BRDF. 55, 60
ρ_s	specular part of refractive index dependent BRDF. 55, 60
θ	Elevation/Inclination angle, incident, excitant. 11–13, 26, 37, 39, 40, 54, 88, 89, 91
$\vec{I}_{rgb}$	RGB value of incident light ray. 26

$\vec{I}$	Incident light ray. 11
$\vec{N}$	Surface normal. 11
$\vec{R}_{rgb}$	RGB value of reflected light ray. 26
$\vec{R}$	Reflected light ray. 11
$\vec{d}$	Change in direction of wave propagation. 68, 69
$\vec{p}$	Pixel position on image sensor. 68, 69
$\vec{r}$	Direction of wave propagation. 14, 68
$\vec{x}$	Position of light wave in 3d. 12, 14
c_d	Drag coefficient. 72, 73
f_r	Bidirectional reflectance distribution function. 11, 12, 50, 91
f_t	Bidirectional transmittance distribution function. 13
k_i	ith Kinect sensor in setup. 73
n_i	Refactive index of the surrounding medium or thin film layer. 16, 48, 49, 53, 55–62, 70
n_t	Refactive index of the transmitting medium or substrate. 16, 38, 55, 59, 60
n	Refactive index field. 13
r	Complex refractive index. 31, 32, 39
s	Path length. 13, 14
t	Time instant or frame, usually the time period that a CCD-chip is exposed to incident light. 73
Δ_0	Unaltered disparity value computed by Kinect (no difference measurable). 68, 69
Δ_c	Altered disparity value computed by Kinect (closer distance estimated). 69
Δ_f	Altered disparity value computed by Kinect (closer distance estimated). 68, 69
Δ	Disparity value computed by Kinect. 69

Bibliography

[1] Adrian, R., and Westerweel, J. *Particle image velocimetry*, vol. 30. Cambridge University Press, 2010.

[2] Agarwal, S., Snavely, N., Simon, I., Seitz, S., and Szeliski, R. Building rome in a day. In *Computer Vision, 2009 IEEE 12th International Conference on* (2009), Ieee, pp. 72–79.

[3] Apfel, J. H. Phase retardance of periodic multilayer mirrors. *Appl. Opt. 21*, 4 (Feb 1982), 733–738.

[4] Ashikmin, M., Premože, S., and Shirley, P. A microfacet-based brdf generator. In *Proceedings of the 27th annual conference on Computer graphics and interactive techniques* (2000), ACM Press/Addison-Wesley Publishing Co., pp. 65–74.

[5] Asus. Xtion pro live, May 2012.

[6] Atcheson, B., Ihrke, I., Heidrich, W., Tevs, A., Bradley, D., Magnor, M., and Seidel, H.-P. Time-resolved 3d capture of non-stationary gas flows. *ACM Transactions on Graphics (Proc. SIGGRAPH Asia) 27*, 5 (2008), 132–141.

[7] Baker, S., Scharstein, D., Lewis, J., Roth, S., Black, M., and Szeliski, R. A database and evaluation methodology for optical flow. *International Journal of Computer Vision 92*, 1 (2011), 1–31.

[8] Barron, J., Fleet, D., and Beauchemin, S. Performance of optical flow techniques. *International Journal of Computer Vision 12*, 1 (1994), 43–77.

[9] Beckmann, P., and Spizzichino, A. *The Scattering of Electromagnetic Waves from Rough Surfaces.* Pergamon Press.

[10] Bendicks, C., Tarlet, D., Roloff, C., Bordás, R., Wunderlich, B., Michaelis, B., and Thévenin, D. Improved 3-d particle tracking velocimetry with colored particles. *Journal of Signal and Information Processing 2*, 2 (2011), 59–71.

[13] Berger, K., Reshetouski, I., Magnor, M., and Ihrke, I. Measuring brdfs of immersed materials. In *Proc. Vision, Modeling and Visualization (VMV) 2011* (Oct. 2011), pp. 325–330.

[14] Berger, K., Ruhl, K., Albers, M., Schröder, Y., Scholz, A., Guthe, S., and Magnor, M. The capturing of turbulent gas flows using multiple kinects. In *Proc. CDC4CV 2011* (Nov. 2011), IEEE, pp. 1108–1113. ISBN: 978-1-4673-0061-2.

[15] Berger, K., Ruhl, K., Schroeder, Y., Brümmer, C., Scholz, A., and Magnor, M. Markerless motion capture using multiple color-depth sensors. In *Proc. Vision, Modeling and Visualization (VMV) 2011* (2011), pp. 317–324.

[16] Berger, K., Wilkie, A., Weidlich, A., and Magnor, M. Modeling and verifying the polarizing reflectance of real-world metallic surfaces. *Computer Graphics and Applications 32*, 2 (Mar. 2012), 24–33.

[15] Blinn, J. Models of light reflection for computer synthesized pictures. In *ACM SIGGRAPH Computer Graphics* (1977), vol. 11, ACM, pp. 192–198.

[16] Blinn, J. F. Models of Light Reflection for Computer Synthesized Pictures. In *Proc. of SIGGRAPH* (1977), pp. 192–198.

[17] Bordás, R., Bendicks, C., Kuhn, R., Wunderlich, B., Thévenin, D., and Michaelis, B. Coloured tracer particles employed for 3-d ptv in gas flows. In *ISFV13-13th International Symposium on Flow Visualization, and FLUVISU12-12th French Congress on Visualization in Fluid Mechanics, Paper*, vol. 93, pp. 1–4.

[18] Burrus, N. `http://nicolas.burrus.name/index.php/Research/KinectCalibration`, November 2010.

[19] Callet, P. L'apparence visuelle des bronzes – restauration virtuelle d'une statuette chinoise. In *CNRS-GDR 2602 couleur et matériaux à effets visuels, 2006, éditions BELIN* (2006).

[20] Callet, P. Metals, alloys and lighting: optical properties and spectral simulation in computer graphics. In *CIE expert symposium, 19-20* (2006).

[21] Callet, P. Couleur et apparence visuelle ii : L'aspect métallique. In *CIE expert symposium, 19-20* (2007).

[22] Callet, P., De Contencin, F., Zymla, A., Denizet, P., Hilpert, T., Miyazawa, K., and Robin, B. An emblematic bronze from cyprus the idalion project. *Digital Heritage* (2010), 206–224.

[23] Callet, P., et al. Virtual restoration of bronze-3d capture and optical simulation in parallel spectral ray-tracing. In *International Cultural Heritage Informatics Meeting ICHIM* (2005), Citeseer.

[24] Callet, P., and Zymla, A. Rendering of binary alloys – example and validation with bronze. In *ICCVG'04* (2005).

[25] Challinor, R., Matheson, D., Crooker, K., Flury, M., Boch, M., Egozy, E., Tate, D., and Goldstein, S. Gesture-based user interface, Oct. 27 2010. US Patent App. 12/913,493.

[26] Charbonnier, C., Schmid, J., Kolo-Christophe, F., Magnenat-Thalmann, N., Becker, C., and Hoffmeyer, P. Virtual hip joint: from computer graphics to computer-assisted diagnosis. In *Eurographics 2009 - First Medical Prize* (April 2009), Eurographics Association, Munich, Germany, pp. 1–4.

[27] Chen, S., Li, J., Torrance, K., and Pattanaik, S. Preliminary calibration of the photometrics pxl1300l ccd camera. Tech. rep., Technical Report PCG-96-1, Cornell University Program of Computer Graphics, 1996.

[28] Cook, R. L., and Torrance, K. E. A Reflectance Model for Computer Graphics. In *Proc. of SIGGRAPH* (1981), pp. 307–316.

[29] Czarske, J. Laser doppler velocimetry using powerful solid-state light sources. *Measurement Science and Technology 17* (2006), 71.

[30] Dai, Q., Wang, J., Liu, Y., Snyder, J., Wu, E., and Guo, B. The Dual-microfacet Model for Capturing Thin Transparent Slabs. *CGF 28*, 7 (2009), 1917–1925.

[31] Dana, K., Livescu, G., and Makonahalli, R. Transparent watermarking using bidirectional imaging. In *Computer Vision and Pattern Recognition Workshops, 2009. CVPR Workshops 2009. IEEE Computer Society Conference on* (2009), IEEE, pp. 31–38.

[32] Dana, K., Livescu, G., and Makonahalli, R. Transparent watermarking using bidirectional imaging. In *Computer Vision and Pattern Recognition Workshops, 2009. CVPR Workshops 2009. IEEE Computer Society Conference on* (june 2009), pp. 31 –38.

[33] DARPA. Darpa robotics challenge (drc). `http://www.darpa.mil/Our_Work/TTO/Programs/DARPA_Robotics_Challenge.aspx`, 2010.

[34] Daubert, K., Lensch, H., Heidrich, W., and Seidel, H. Efficient cloth modeling and rendering. In *12th Eurographics Workshop on Rendering* (2001), pp. 63–70.

[35] Davidson, M. Fundamentals of xenon arc lamps. `http://zeiss-campus.magnet.fsu.edu/articles/lightsources/xenonarc.html`, 2011.

[36] Debevec, P. The uffizi gallery, florence. light probe image gallery. `http://www.pauldebevec.com/Probes/uffizi_probe.hdr`, 1998.

[37] Debevec, P. Rendering synthetic objects into real scenes: Bridging traditional and image-based graphics with global illumination and high dynamic range photography. In *ACM SIGGRAPH 2008 classes* (2008), ACM, pp. 32:01–32:10.

[38] Deen, N., Willems, P., van Sint Annaland, M., Kuipers, J., Lammertink, R., Kemperman, A., Wessling, M., and van der Meer, W. On image pre-processing for piv of single-and two-phase flows over reflecting objects. *Experiments in fluids 49*, 2 (2010), 525–530.

[39] deutsche Muenze, M. Polierte Platte. `http://www.mdm.de/catalogsearch/result/?q=polierte+platte`.

[40] Doh, D., Hwang, T., and Saga, T. 3d-ptv measurements of the wake of a sphere. *Measurement Science and Technology 15* (2004), 1059.

[41] Drude, P. *Lehrbuch der Optik*. S. Hirzel, 1901.

[42] Drulea, M., and Nedevschi, S. Total variation regularization of local-global optical flow. In *Intelligent Transportation Systems (ITSC), 2011 14th International IEEE Conference on* (2011), IEEE, pp. 318–323.

[43] Durand, F., and Dorsey, J. Fast bilateral filtering for the display of high-dynamic-range images. In *ACM Transactions on Graphics (TOG)* (2002), vol. 21, ACM, pp. 257–266.

[44] Engelhard, N. `http://www.informatik.uni-freiburg.de/~engelhar/calibration.html`, mai 2011.

[45] Everitt, C. Projective texture mapping. *White paper, NVidia Corporation* (2001).

[46] Feng, P. Blue angels + high speed pass = schlieren! `http://www.flickr.com/photos/paulcamerastination/5085687122/in/set-72157622352905416` All rights reserved. Used with permission., 2007.

[47] Fischler, M., and Bolles, R. Random sample consensus: a paradigm for model fitting with applications to image analysis and automated cartography. *Communications of the ACM 24*, 6 (1981), 381–395.

[48] FREEDMAN, B., SHPUNT, A., MACHLINE, M., and ARIELI, Y. Depth mapping using projected patterns, Oct. 9 2008. WO Patent WO/2008/120,217.

[49] FresnelTech. `http://www.fresneltech.com/`, 2012.

[50] Gaffney, M. `http://www.thingiverse.com/thing:7793`, 2011.

[51] Ghosh, A., Chen, T., Peers, P., Wilson, C., and Debevec, P. Circularly polarized spherical illumination reflectometry. In *ACM Transactions on Graphics (TOG)* (2010), vol. 29, ACM, pp. 162–173.

[52] Ghosh, A., Heidrich, W., Achutha, S., and O'Toole, M. A Basis Illumination Approach to BRDF Measurement. *International Journal of Computer Vision 90*, 2 (November 2010), 183–197.

[53] Goldstein, D., and Collett, E. *Polarized light*, vol. 83. CRC, 2003.

[54] Goss, L., Post, M., Sarka, B., and Trump, D. Two-color particle velocimetry. In *Proceedings of SPIE* (1990), vol. 1404, pp. 99–288.

[55] Gregson, J., Krimerman, M., Hullin, M. B., and Heidrich, W. Stochastic tomography and its applications in 3d imaging of mixing fluids. *ACM Trans. Graph. (Proc. SIGGRAPH 2012) 31*, 4 (2012), 52:1–52:10.

[56] Gu, J., Ramamoorthi, R., Belhumeur, P., and Nayar, S. K. Dirty Glass: Rendering Contamination on Transparent Surfaces. In *Proc. of EGSR* (2007), pp. 159–170.

[57] Gudmundsson, S., Larsen, R., Aanaes, H., Pardas, M., and Casas, J. Tof imaging in smart room environments towards improved people tracking. In *Computer Vision and Pattern Recognition Workshops, 2008. CVPRW'08. IEEE Computer Society Conference on* (2008), IEEE, pp. 1–6.

[58] Gupta, R., and Magnenat-Thalmann, N. Interactive rendering of optical effects in wet hair. In *Proceedings of the 2007 ACM symposium on Virtual reality software and technology* (2007), ACM, pp. 133–140.

[59] Haidinger, W. Ueber das directe erkennen des polarisirten lichts und der lage der polarisationsebene. *Annalen der Physik 139*, 9 (1844), 29–39.

[60] Hallin, M., Paindaveine, D., and Šiman, M. Multivariate quantiles and multiple-output regression quantiles: From l1 optimization to halfspace depth. *The Annals of Statistics 38*, 2 (2010), 635–669.

[61] Hanrahan, P., and Krueger, W. Reflection from Layered Surfaces due to Subsurface Scattering. In *Proc. of SIGGRAPH* (1993), pp. 164–174.

[62] Hasler, N., Thormählen, T., Rosenhahn, B., and Seidel, H. Learning skeletons for shape and pose. In *Proceedings of the 2010 ACM SIGGRAPH symposium on Interactive 3D Graphics and Games* (2010), ACM, pp. 23–30.

[63] He, X., Torrance, K., Sillion, F., and Greenberg, D. A comprehensive physical model for light reflection. In *ACM SIGGRAPH Computer Graphics* (1991), vol. 25, ACM, pp. 175–186.

[64] He, X. D., Torrance, K. E., Sillion, F. X., and Greenberg, D. P. A Comprehensive Physical Model for Light Reflection. In *Proc. of SIGGRAPH* (1991), pp. 175–186.

[65] Hegedüs, R., Szél, G., and Horváth, G. Imaging polarimetry of the circularly polarizing cuticle of scarab beetles (coleoptera: Rutelidae, cetoniidae). *Vision research 46*, 17 (2006), 2786–2797.

[66] Horn, B., and Schunck, B. Determining optical flow. *Artificial intelligence 17*, 1-3 (1981), 185–203.

[67] Howes, W. Rainbow schlieren and its applications. *Applied optics 23*, 14 (1984), 2449–2460.

[68] Huffaker, R. M. Laser doppler detection systems for gas velocity measurement. *Appl. Opt. 9*, 5 (May 1970), 1026–1039.

[69] Huhle, B., Jenke, P., and Strasser, W. On-the-fly scene acquisition with a handy multi-sensor system. *International Journal of Intelligent Systems Technologies and Applications 5*, 3 (2008), 255–263.

[70] Hullin, M. B., Hanika, J., Ajdin, B., Kautz, J., Seidel, H.-P., and Lensch, H. P. A. Acquisition and Analysis of Bispectral BRDFs. *Transactions on Graphics 29*, 3 (2010).

[71] Hyde, M. W., Schmidt, J. D., and Havrilla, M. J. A geometrical optics polarimetric bidirectional reflectance distribution function for dielectric and metallic surfaces. *Opt. Express 17*, 24 (Nov 2009), 22138–22153.

[72] Ihrke, I., Ziegler, G., Tevs, A., Theobalt, C., Magnor, M., and Seidel, H.-P. Eikonal rendering: Efficient light transport in refractive objects. *SIGGRAPH '07: ACM SIGGRAPH 2007 papers* (2007), 59.

[73] Jensen, H., and Buhler, J. A rapid hierarchical rendering technique for translucent materials. In *ACM Transactions on Graphics (TOG)* (2002), vol. 21, ACM, pp. 576–581.

[74] Jensen, H., Legakis, J., Dorsey, J., Justin, J., and Dorsey, L. Rendering of wet materials. 273–282.

[75] Jones, C., Jenkins, O., and Loper, M. System and method for cooperative remote vehicle behavior, Apr. 11 2008. US Patent App. 12/101,949.

[76] Kajiya, J. T. Anisotropic Reflection Models. In *Proc. of SIGGRAPH* (1985), pp. 15–21.

[77] Kasai, C., Namekawa, K., Koyano, A., and Omoto, R. Real-time two-dimensional blood flow imaging using an autocorrelation technique. *IEEE Trans. Sonics Ultrason 32*, 3 (1985), 458–464.

[78] Kautz, J., and McCool, M. Interactive rendering with arbitrary BRDFs using separable approximations. In *Eurographics Rendering Workshop 1999* (1999), vol. 18, Citeseer.

[79] Keane, R., Adrian, R., and Zhang, Y. Super-resolution particle imaging velocimetry. *Measurement Science and Technology 6* (1995), 754.

[80] Kelemen, C., and Szirmay-Kalos, L. A microfacet based coupled specular-matte brdf model with importance sampling. In *Eurographics Short Presentations* (2001), vol. 25, p. 34.

[81] Kneip, L., Tâche, F., Caprari, G., and Siegwart, R. Characterization of the compact hokuyo urg-04lx 2d laser range scanner. In *Robotics and Automation, 2009. ICRA'09. IEEE International Conference on* (2009), IEEE, pp. 1447–1454.

[82] Lafortune, E. P. F., Foo, S.-C., Torrance, K. E., and Greenberg, D. P. Non-linear Approximation of Reflectance Functions. In *Proc. of SIGGRAPH* (1997), pp. 117–126.

[83] Levoy, M. Lecture an light and shadow. `http://www-graphics.stanford.edu/courses/cs99d-01/light2.htm`, 2011.

[84] Lu, J., Georghiades, A. S., Rushmeier, H., Dorsey, J., and Xu, C. Synthesis of Material Drying History: Phenomenon Modeling, Transferring and Rendering . In *Proc. of Workshop on Natural Phenomena* (2005), pp. 175–184.

[85] Lucas, B., and Kanade, T. An iterative image registration technique with an application to stereo vision. In *Proceedings of the 7th international joint conference on Artificial intelligence* (1981).

[86] Lynch, D., Hunter, W., and Palik, E. Handbook of optical constants of solids. *Academic, Orlando* (1985), 353.

[87] Madsen, K., Bruun, H., and Tingleff, O. *Methods for non-linear least squares problems.* TU Denmark, 1999.

[88] Maeda, M., Kawaguchi, T., and Hishida, K. Novel interferometric measurement of size and velocity distributions of spherical particles in fluid flows. *Measurement Science and Technology 11*, 12 (2000), L13.

[89] Mantiuk, R., Krawczyk, G., Mantiuk, R., and Seidel, H. High dynamic range imaging pipeline: Perception-motivated representation of visual content. *Human Vision and Electronic Imaging XII, Proceedings of the SPIE 6492* (2007).

[90] Marquardt, D. An algorithm for least-squares estimation of nonlinear parameters. *Journal of the society for Industrial and Applied Mathematics 11*, 2 (1963), 431–441.

[91] Marschner, S. R., Westin, S. H., Lafortune, E. P. F., and Torrance, K. E. Image-based Bidirectional Reflectance Distribution Function Measurement. *Applied Optics 39*, 16 (2000), 460–466.

[92] Mäthger, L., Shashar, N., and Hanlon, R. Do cephalopods communicate using polarized light reflections from their skin? *The Journal of Experimental Biology 212*, 2133–2140.

[93] Matlab. Technical documentation: Quiver or velocity plot `http://www.mathworks.de/help/techdoc/ref/quiver.html`, 2012.

[94] Matusik, W., Pfister, H., Brand, M., and McMillan, L. A Data-Driven Reflectance Model. *Transactions on Graphics 22*, 3 (2003), 759–769.

[95] Matusik, W., Pfister, H., Brand, M., and McMillan, L. A data-driven reflectance model. In *Proceedings International Conference on Computer Graphics and Interactive Techniques, ACM SIGGRAPH* (2003), pp. 27–31.

[96] Matusik, W., Pfister, H., Brand, M., and McMillan, L. Efficient isotropic BRDF measurement. In *Proceedings of the 14th Eurographics workshop on Rendering* (2003), Eurographics Association, pp. 241–247.

[97] Matusik, W., Pfister, H., McMillan, L., and Brand, M. MIT/Merl BRDF Database (2003) http://graphics. csail. mit. edu/˜ wojciech.

[98] Meier. Computerized background-oriented schlieren. *Experiments in Fluids 33* (2002), 181–187. 10.1007/s00348-002-0450-7.

[99] Meier, G., 1999. German Patent DE 199 42 856 A1.

[100] Meinhart, C., Wereley, S., and Gray, M. Volume illumination for two-dimensional particle image velocimetry. *Measurement Science and Technology 11* (2000), 809–817.

[101] MicroLens. `http://www.microlens.com/pages/choosing_right_lens.htm`, 2012.

[102] Möller, W., Nikolaus, K., and Höpe, A. Degradation of the diffuse reflectance of spectralon under low-level irradiation. *Metrologia 40* (2003), S212.

[103] Neumann, D., Lugauer, F., Bauer, S., Wasza, J., and Hornegger, J. Real-time rgb-d mapping and 3-d modeling on the gpu using the random ball cover

data structure. In *Computer Vision Workshops (ICCV Workshops), 2011 IEEE International Conference on* (2011), IEEE, pp. 1161–1167.

[104] Newling, B., Poirier, C., Zhi, Y., Rioux, J., Coristine, A., Roach, D., and Balcom, B. Velocity imaging of highly turbulent gas flow. *Physical review letters 93*, 15 (2004), 154503–154511.

[105] Ngan, A., Durand, F., and Matusik, W. Experimental Analysis of BRDF Models. In *Proc. of EGSR* (2005), pp. 117–126.

[106] Nicodemus, F., Richmond, J., Hsia, J., Ginsberg, I., and Limperis, T. *Geometrical considerations and nomenclature for reflectance.* National Bureau of Standards (US), 1977.

[107] Nishino, K. Directional statistics brdf model. In *Computer Vision, 2009 IEEE 12th International Conference on* (29 2009-oct. 2 2009), pp. 476 –483.

[108] Oren, M., and Nayar, S. K. Generalization of Lambert's Reflectance Model. In *Proc. of SIGGRAPH* (1994), pp. 239–246.

[109] Otas, K., Pakenas, V., Vaskys, A., and Vaskys, P. Investigation of led light attenuation in fog. *Electronics and Electrical Engineering 121*, 5 (2012), 47–52.

[110] Palik, E. D. *Handbook of Optical Constants of Solids.* Academic Press, 1985.

[111] Patrick Callet, Anna Zymla, A. M. Virtual metallurgy and archaeology. In *ICCVG* (2002), pp. 1–8.

[112] Pharr, M., and Humphreys, G. *Physically based rendering: From theory to implementation.* Morgan Kaufmann, 2004.

[113] Phong, B. T. Illumination for Computer Generated Pictures. *Comm. ACM 18*, 6 (1975), 311–317.

[114] Pike, E. Laser doppler velocimetry, Feb. 1 1975. US Patent 3,866,055.

[115] Poulin, P., and Fournier, A. A Model for Anisotropic Reflection. In *Proc. of SIGGRAPH* (1990), pp. 273–282.

[116] Prasad, R., and Sreenivasan, K. Quantitative three-dimensional imaging and the structure of passive scalar fields in fully turbulent flows. *Journal of Fluid Mechanics 216*, -1 (1990), 1–34.

[117] Priest, R., and Gerner, T. Polarimetric brdf in the microfacet model: theory and measurements. Tech. rep., DTIC Document, 2000.

[118] Print3d. `http://printin3d.com/`, mai 2012.

[119] Realflow. Realflow 2010. `http://www.realflow.com/rf_product.php`, 2010.

[120] Requicha, A., Voelcker, H., and Rochester Univ., N. Y. P. A. P. Constructive solid geometry. Tech. rep., Rochester Univ., N. Y. Production Automation Project, 1977.

[121] Rother, A. Ellipsometer. *Review on Scientific Instrument 16* (1945).

[122] Rother, A. Optimizing precision of rotating-analyzer ellipsometers. *Optical Society of America 6* (1974), 639–646.

[123] Santiago, J., Wereley, S., Meinhart, C., Beebe, D., and Adrian, R. A particle image velocimetry system for microfluidics. *Experiments in Fluids 25*, 4 (1998), 316–319.

[124] Schlick, C. An Inexpensive BRDF Model for Physically-Based Rendering. *Computer Graphics Forum 13*, 3 (1994), 233–246.

[125] Schmalstieg, D. `http://studierstube.icg.tugraz.at/handheld_ar/images/artoolkitplus_BCH_thin_board.png`, June 2012.

[126] Scholz, V., Stich, T., Keckeisen, M., Wacker, M., and Magnor, M. Garment motion capture using color-coded patterns. In *Computer Graphics Forum* (2005), vol. 24, Wiley Online Library, pp. 439–447.

[127] SENTECH. Short manual of the sentech se800 ellipsometer, May 2000.

[128] Sillion, F., Puech, C., et al. *Radiosity and global illumination.* Springer, 1994.

[129] Small, C., Steckler, M., Seeber, L., Akhter, S., Goodbred Jr, S., Mia, B., and Imam, B. Spectroscopy of sediments in the ganges-brahmaputra delta: Spectral effects of moisture, grain size and lithology. *Remote Sensing of Environment 113*, 2 (2009), 342–361.

[130] Sun, B., Sunkavalli, K., Ramamoorthi, R., Belhumeur, P. N., and Nayar, S. K. Time-Varying BRDFs. *TVCG 13*, 3 (2007), 595–609.

[131] Torrance, K., and Sparrow, E. Theory for off-specular reflection from roughened surfaces. *J. Optical Soc. America 57* (1967), 1105–1114.

[132] Torrance, K. E., and Sparrow, E. M. Theory for Off-Specular Reflection from Roughened Surfaces. *JOSA 57*, 9 (1967), 1105–1114.

[133] Towers, D., Towers, C., Buckberry, C., and Reeves, M. A colour piv system employing fluorescent particles for two-phase flow measurements. *Measurement Science and Technology 10* (1999), 824–832.

[134] Trowbridge, T., and Reitz, K. Average irregularity representation of a rough surface for ray reflection. *JOSA 65*, 5 (1975), 531–536.

[135] Voigt, A., Skupsch, C., Koenig, J., Shirai, K., Buettner, L., and Czarske, J. Laser doppler field sensor for two dimensional flow measurements in three velocity components. *Imaging Measurement Methods for Flow Analysis* (2009), 21–30.

[136] Voss, K. J., and Zhang, H. Bidirectional reflectance of dry and submerged labsphere spectralon plaque. *Appl. Opt. 45*, 30 (Oct 2006), 7924–7927.

[137] W. T. Mayo, J., and Allen, J. B. New doppler holographic technique for fluid velocity visualization and measurement. *Appl. Opt. 10*, 9 (Sep 1971), 2119–2126.

[138] Walter, B., Marschner, S., Li, H., and Torrance, K. Microfacet Models for Refraction through Rough Surfaces. *Eurographics Symposium on Rendering (2007)* (2008).

[139] Ward, G. J. Measuring and Modeling Anisotropic Reflection. In *Proc. of SIGGRAPH* (1992), pp. 265–272.

[140] Ward, K., and Lin, M. Modeling hair influenced by water and styling products. In *In International Conference on Computer Animation and Social Agents (CASA* (2004), Citeseer.

[141] Weaver, J., Krafka, C., Lynch, D., and Koch, E. Optical properties of metals. i.–the transition metals. *Phys. Data, 18*, 1 (1981), 302.

[142] Weidlich, A., and Wilkie, A. Arbitrarily Layered Micro-Facet Surfaces. In *Proc. of Pacific Graphics* (2007), pp. 171–178.

[143] Weidlich, A., and Wilkie, A. Arbitrarily layered micro-facet surfaces. In *Proceedings of the 5th international conference on Computer graphics and interactive techniques in Australia and Southeast Asia* (2007), ACM, pp. 171–178.

[144] Weinberg, F. *Optics of Flames: Including methods for the study of refractive index fields in combustion and aerodynamics.* Butterworths, 1963.

[145] Wetzstein, G., Raskar, R., and Heidrich, W. Hand-held schlieren photography with light field probes. In *Computational Photography (ICCP), 2011 IEEE International Conference on* (2011), IEEE, pp. 1–8.

[146] Wheeless, C. Wheeless' textbook of orthopaedics. *Fractures of the Femoral Neck* (1996).

[147] Wilkie, A., Weidlich, A., Magnor, M., and Chalmers, A. Predictive rendering. In *ACM SIGGRAPH ASIA 2009 Courses* (2009), ACM, p. 12.

[148] Young, A., and Naghi, H. Lens accessory for video game sensor device, Feb. 28 2012. US Patent 8,123,622.

[149] Zaber, I. `http://www.zaber.com/wiki/Manuals/T-RS`, Juni 2012.

[150] Zhang, H., and Voss, K. Bidirectional reflectance study on dry, wet, and submerged particulate layers: effects of pore liquid refractive index and translucent particle concentrations. *Applied optics 45*, 34 (2006), 8753–8763.

[151] Zhang, L., Curless, B., and Seitz, S. Rapid shape acquisition using color structured light and multi-pass dynamic programming. In *3D Data Processing Visualization and Transmission, 2002. Proceedings. First International Symposium on* (2002), IEEE, pp. 24–36.

[152] Zurich, E. `http://www.paccar.ethz.ch/`, mai 2012.

Author's publications

Kai Berger, Christian Linz, Christian Lipski, Timo Stich, and Marcus Magnor. Echtzeiterkennung von befahrbaren bereichen in urbanen szenarien. In *Proc. GI-Fachausschuss*.

Kai Berger, Christian Lipski, Christian Linz, Timo Stich, and Marcus Magnor. The area processing unit of caroline - finding the way through darpa's urban challenge. In *Proc. 2nd Workshop Robot Vision (RobVis 2008) 2008*, February 2008.

Christian Lipski, Björn Scholz, Kai Berger, Christian Linz, Timo Stich, and Marcus Magnor. A fast and robust approach to lane marking detection and lane tracking. In *Proc. IEEE Southwest Symposium on Image Analysis and Interpretation 2008*, volume 2008, pages 57–60, Washington, DC, USA, July 2008. IEEE Computer Society, IEEE Computer Society.

Kai Berger, Bradly Atcheson, Ivo Ihrke, Wolfgang Heidrich, and Marcus Magnor. Tomographic 4D reconstruction of gas flows in the presence of occluders. In *Proc. Vision, Modeling and Visualization (VMV) 2009*, November 2009.

Kai Berger, Christian Lipski, Christian Linz, Anita Sellent, and Marcus Magnor. A ghosting artifact detector for interpolated image quality assessment. In *Proc. ACM Applied Perception in Computer Graphics and Visualization (APGV) 2009*, September 2009.

Ivo Ihrke, Kai Berger, Bradly Atcheson, Marcus Magnor, and Wolfgang Heidrich. Tomographic reconstruction and efficient rendering of refractive gas flows. In Wolfgang Nitsche and Christoph Dobriloff, editors, *Notes on Numerical Fluid Mechanics and Multidisciplinary Design*, volume 106, pages 145–154. Springer Berlin / Heidelberg, February 2009.

Christian Lipski, Kai Berger, and Marcus Magnor. visage - A visualization and debugging framework for distributed system applications. In Vaclav Skala, editor, *Proc.*

WSCG 2009, volume 2009, pages 1–7, Plzen, Czech Republic, February 2009. UNION Agency – Science Press.

Kai Berger, Christian Linz, Christian Lipski, Tobi Vaudrey, Reinhard Klette, and Marcus Magnor. Target space interactivity - the end of 3D widgets. In *WSCG Communication Papers Proceedings 2010*, February 2010.

Kai Berger, Christian Lipski, Christian Linz, Anita Sellent, and Marcus Magnor. A ghosting artifact detector for interpolated image quality assessment. In *Proc. IEEE International Symposium on Consumer Electronics (ISCE) 2010*, June 2010.

Andrea Keil, Georgia Albuquerque, Kai Berger, and Marcus Magnor. Real-time gaze tracking with a consumer-grade video camera. In Vaclav Skala, editor, *Proc. WSCG 2010*, Plzen, Czech Republic, February 2010. UNION Agency – Science Press.

Christian Lipski, Denis Bose, Martin Eisemann, Kai Berger, and Marcus Magnor. Sparse bundle adjustment speedup strategies. In *WSCG Communication Papers Proceedings 2010*, pages 85–88, February 2010.

Christian Lipski, Christian Linz, Kai Berger, Anita Sellent, and Marcus Magnor. Virtual video camera: Image-based viewpoint navigation through space and time. *Computer Graphics Forum*, 29(8):2555–2568, 2010.

Kai Berger, Ilya Reshetouski, Marcus Magnor, and Ivo Ihrke. Measuring brdfs of immersed materials. In *Proc. Vision, Modeling and Visualization (VMV) 2011*, pages 325–330, October 2011.

Kai Berger, Kai Ruhl, Mark Albers, Yannic Schröder, Alexander Scholz, Stefan Guthe, and Marcus Magnor. The capturing of turbulent gas flows using multiple kinects. In *Proc. CDC4CV 2011*, pages 1108–1113. IEEE, November 2011. ISBN: 978-1-4673-0061-2.

Kai Berger, Kai Ruhl, Yannic Schroeder, Christian Brümmer, Alexander Scholz, and Marcus Magnor. Markerless motion capture using multiple color-depth sensors. In *Proc. Vision, Modeling and Visualization (VMV) 2011*, pages 317–324, 2011.

Kai Berger, Alexander Wilkie, Andrea Weidlich, and Marcus Magnor. Modeling and verifying the polarizing reflectance of real-world metallic surfaces. *Computer Graphics and Applications*, 32(2):24–33, March 2012.

Curriculum Vitæ - Lebenslauf

Curriculum Vitæ

1985	born in Braunschweig, Germany
2004	High school degree, main subjects politics and mathematics
	Wilhelm-Gymnasium Braunschweig, Germany
2004-2008	Diploma in Computer Science
	TU Braunschweig, Germany
2008-2012	Ph.D. Student, Instut für Computergraphik
	TU Braunschweig, Germany

Lebenslauf

1985	geboren in Braunschweig
2004	Allgemeine Hochschulreife
	Wilhelm-Gymnasium Braunschweig
2004-2008	Diplomstudium in Informatik
	TU Braunschweig
2008-2012	Wissenschaftlicher Mitarbeiter, Institut für Computergraphik
	TU Braunschweig